

**An Adaptive Discrete Newton Method
for a Regularization-Free Bingham
Model**

Dissertation
zur Erlangung des akademischen Grades eines
Doktors der Naturwissenschaften
(Dr. rer. nat.)

Der Fakultät für Mathematik der
Technischen Universität Dortmund
vorgelegt von

Arooj Fatima

im März 2023

Dissertation

An Adaptive Discrete Newton Method for a Regularization-Free Bingham Model

Fakultät für Mathematik
Technische Universität Dortmund

Erstgutachter: Prof. Dr. Stefan Turek
Zweitgutachter: Prof. Dr. Heribert Blum

Tag der mündlichen Prüfung: 11.07.2023

Abstract

Developing a numerical and algorithmic tool which correctly identifies unyielded regions in the yield stress fluid flow is a challenging task. Two approaches are commonly used to handle the singular behaviour at the yield surface, i.e. the Augmented Lagrangian approach and the regularization approach, respectively. Generally in the regularization approach for the resulting nonlinear and linear problems, solvers do not perform efficiently when the regularization parameter gets very small. In this work, we use a formulation introducing a new auxiliary stress [1]. The three field formulation of yield stress fluids corresponds to a regularization-free Bingham formulation. The resulting set of equations arising from the three field formulation is treated efficiently and accurately by a monolithic finite element method. The velocity and pressure are discretized by the higher order stable FEM pair Q_2/P_1^{disc} and the auxiliary stress is discretized by the Q_2 element.

Furthermore, this problem is highly nonlinear and presents a big challenge to any nonlinear solver. We developed a new adaptive discrete Newton's method, which evaluates the Jacobian with the directional divided difference approach [2]. The step size in this process is an important key: We relate this size to the rate of the actual nonlinear reduction for achieving a robust adaptive Newton's method. The resulting linear subproblems are solved using a geometrical multigrid solver. We analyse the solvability of the problem along with the adaptive Newton method for Bingham fluids by doing numerical studies for different prototypical configurations, i.e. "Viscoplastic fluid flow in a channel"[2], "Lid Driven Cavity", "Flow around cylinder", and "Bingham flow in a square reservoir", respectively.

Key words— Viscoplastic Fluids, Bingham Fluid, Divided Difference, FEM, Adaptive Newton Method, Regularization-Free, Edge-oriented FEM stabilization.

*To my parents,
husband and siblings*

Acknowledgments

First and foremost, I would like to express my heartiest gratitude to my supervisor, Prof. Dr. Stefan Turek for providing me an opportunity to work under his invaluable expertise in his excellent research group. His insightful feedback pushed me to sharpen my thinking and brought my work to a higher level. Thank you for your guidance, confidence, optimism, advice and ideas throughout these years.

I am also thankful to Dr. Abderrahim Ouazzi for very helpful discussions and guidance on my research topic, which helped me to improve my understandings. I would also like to thank Dr. Hogenrich Damanik for providing his *FeatFlow* software version, great help and guidance to understand the code. He provided the tools to choose the right direction for my dissertation. Additionally, all my LSIII colleagues and secretaries for their wonderful collaboration in these years. I am thankful to Tatiana Theis, Rida Ahmad, Omid Ahmadi, Dr. Liudmila Rivkind, Lydia Wambach, Dr. Hennes Hajduk and Xenia Kerkhoff for providing very friendly atmosphere. I am very grateful to Dr. Timm Treskatis for his valuable guidance and discussions which helped me in the numerical computations.

I also want to thank my family for their prayers, love and encouragement. Finally, I am extremely grateful to Muhammad Aaqib Afaq (my lovely husband) for his immense love, patience and support to make my career a priority in our life. Fortunately, being also a part of LSIII, we always have very delightful discussions with each others related to our research work. This endeavor would not have been possible without his constant encouragement during the challenges in these years.

I would also like to thank the Deutsche Forschungsgemeinschaft (DFG) for their financial support under the DFG Priority Program SPP 1962 and AiF/IGF-Projekt 20845 N "Simulation: Vorhersage und Optimierung des Strangschmelzens in der Fused Filament Fabrication". I would also like to acknowledge the support by LiDO3 team at ITMC, TU Dortmund University.

Contents

1	Motivation	1
1.1	Motivation	1
1.2	Introduction	2
1.3	Contribution of the Thesis	3
1.4	Organization	4
1.5	Already Published Contributions	5
2	Mathematical Modelling for Bingham Viscoplastic Fluids	7
2.1	Classification of the Fluids	7
2.2	Bingham Viscoplastic Fluid	9
2.2.1	Regularization Techniques and Three-Field Formulation	9
2.3	Variational Formulation	11
2.3.1	The Weak Form of Navier-Stokes Equations	11
2.3.2	The Weak Form of Bingham Three-Field Formulation	12
2.3.3	Existence and Uniqueness of Solution	14
2.4	Analytical Solution for Bingham flow in a Channel	14
2.4.1	Newtonian Zone	15
2.4.2	Rigid Zone	16
3	Finite Element Method	19
3.1	Introduction	19
3.2	FEM for Poisson's Equation	19
	Choice of the interpolation function	22
3.3	Finite Element Approximations	27

CONTENTS

3.3.1	The Navier-Stokes Equations	27
3.3.2	The Bingham Three-Field Formulation	28
3.4	Stability of the Finite Elements	29
3.5	Edge Oriented FEM Stabilization	31
3.6	Artificial Diffusion Stabilization	31
4	Nonlinear and Linear Solvers	33
4.1	Nonlinear Solver	33
4.1.1	Newton Method	33
4.2	Linear Solver	35
4.2.1	Multigrid Method	36
4.3	Flow Around Cylinder Benchmark	37
4.4	Lid Driven Cavity Benchmark	42
5	Numerical Study of Bingham	45
5.1	Bingham Fluid Flow in a Channel	45
5.1.1	Boundary Conditions: Case 1	46
5.1.2	Boundary Conditions: Case 2	54
5.2	Multigrid Parameters Study	57
5.3	Bingham Flow in a Channel with EOFEM Stabilization	61
5.4	Bingham Flow in a Channel with Artificial Diffusion Stabilization	67
6	Adaptive Discrete Newton	73
6.1	Adaptive Discrete Newton	73
6.2	Numerical Results	75
6.2.1	Bingham Fluid Flow in a Channel	75
6.2.2	Lid Driven Cavity	83
6.2.3	Flow Around Cylinder	91
6.2.4	Rotational Bingham Flow in a Square Reservoir	94
7	Conclusions	97

Chapter 1

Motivation

1.1 Motivation

Viscoplastic fluids have been the topic of interest since more than 100 years. These fluids are the prominent part of our daily life. Toothpaste is a well known example, where it remains in its solid form until the applied stress (friction with the teeth) is high enough to deform the toothpaste [3]. Similarly, mayonnaise can be spread over a bread piece and remains at rest afterwards. This transition from solid state to liquid is reversible if the chemical reactions do not take place. Apart from the daily life applications, viscoplastic fluids have high significance in industrial processes too. It involves in so many areas e.g. food industry (chocolate making, jam), cosmetic industry (creams), cement industry (concrete flow in constructions) and the paper making industry (suspension of pulp). Nevertheless, the existence of the solid regime in viscoplastic fluids is a controversial debate. On one hand, it is often considered as highly viscous fluid regime [4] instead of true solid. On the other hand, the clear transition of the rheology from solid to liquid is justified in [5].

The solid and liquid regimes cannot be predicted beforehand. It is a very difficult task because of the undergoing rheological transition. Specially, when the fluids are dependent on their flow history, e.g. yield stress fluids. These kind of fluids are in the focus of the present work because of their advantageous use as the lubrication in the multilayer flow applications. One of the interesting applications is viscoplastic lubrication (hydraulic fracturing) and macro encapsulation [6]: Heavy crude oil transportation along pipelines, coal-water slurry transportation and co-extrusion operations. In these processes, the stabilization of the interfaces and to suppress the interfacial instabilities in multi-layer shear flows [7] is the main interest by means of viscoplastic fluids.



Figure 1.1: Examples of viscoplastic material. The image is reprinted from [8]

1.2 Introduction

We have slightly discussed the nature of the viscoplastic fluids, which behaves as solid before a critical yield stress value and as a viscous fluid afterwards. This threshold value concept is reviewed by Barnes et al. [4]. Accurately knowing or predicting this yield stress value for different materials having different properties is really a challenging task. The difficulty arises because of the different regions i.e. rigid zone (fluid moving with uniform velocity) and dead/plug zone (zero velocity region). These regions depend on the yield stress value and are required to be known beforehand. For acquiring this pre-control of viscoplastic fluids in real life situations, several constitutive models have been proposed. Bingham [9] constitutive model is the most widely used model, which includes a discontinuity in the viscosity function, because the fluid does not begin to flow before meeting the threshold value of the yield stress. Consequently, the shear rate is zero. This discontinuity raises complexities in solving the Bingham model not only analytically but also in the numerical approximations. Therefore, solving yield stress/viscoplastic fluid models numerically is still a difficult task.

In order to circumvent this problem, there are some proposed methods in literature for solving viscoplastic fluids e.g. the augmented Lagrangian method was introduced by Hestenes [10] in 1969. This method has been widely used by many scientists in their studies [11, 12, 13, 14]. Afterwards, Glowinski [15] and Fortin et al. [16] used this method to apply on linear Stokes problem and nonlinear problems e.g. Bingham fluid flow (this model describes the nature of the viscoplastic fluids, which is not easy to model numerically). The accurate solution of the Bingham fluid is determined by the determination of the yield

1.3. CONTRIBUTION OF THE THESIS

surfaces, which needs highly refined meshes and are computationally very expensive. One possible solution/remedy was to include a continuous function by Glowinski et al. [15, 16], which leads to the idea of the regularization technique [17].

From 1980's, some regularization models were proposed by regularizing the viscosity term in the Bingham constitutive law. Bercovier and Engelman [18] proposed a function in 1980. Later in 1987, Papanastasiou [19] also introduced a function. The main advantage of such techniques was "easy numerical implementation". Therefore, a trend of the regularization technique was adopted during 1980's and 1990's. However, in 2001 Samarito et al. [20] again worked on the augmented Lagrangian method to show its accuracy in the prediction of yielded zones. In consequence, a competition has been developed between regularization and augmented Lagrangian approach. The disadvantage of the latter approach is the requirement of the large computation time for complex problems, whereas the former one is faster for non-linear complex problems. In 2005, Frigaard et al. [21] has done a detailed review study about the positive and the negative aspects of the regularization techniques.

1.3 Contribution of the Thesis

The contribution of the work presented in this thesis is to develop a numerical and algorithmic tool, which is capable of correctly identifying the unyielded regions in yield stress fluid flow. Two approaches are commonly used to handle the singular behaviour at the yield surface, i.e. the augmented Lagrangian approach and the regularization approach, respectively. Generally in the regularization approach, the numerical solvers do not perform efficiently for instance, when the regularization parameter gets very small.

In this work, we use a formulation by introducing a new auxiliary stress tensor [1]. The three-field formulation of the yield stress fluids corresponds to a regularization-free Bingham model [22]. This method is free from the two apparent deficiencies that effect the shape of the yield surfaces, which are defined for the exact Bingham fluid, namely the regularizations and the inefficient algorithms. Furthermore, this problem is highly nonlinear and presents a big challenge to any nonlinear solver. Therefore, we developed a new adaptive discrete Newton method, which evaluates the Jacobian with the divided difference approach. We relate the step size to the rate of the actual nonlinear reduction for achieving a robust adaptive Newton method. The resulting saddle-point problem is solved efficiently and accurately by a monolithic finite element method. The velocity and pressure are discretized by the higher order stable FEM pair Q_2/P_1^{disc} and the auxiliary stress is discretized by the Q_2 element. We analyse the solvability of the problem along with the adaptive Newton method for Bingham fluids by doing numerical studies for the prototypical configurations.

1.4 Organization

The organization of this research work, excluding the current motivational chapter, is described as follows:

Chapter 2 initially describes the classification of the fluids, and is devoted to the detailed introduction of the Bingham viscoplastic fluid along its mathematical equations. The associated constitutive law exhibits the fluid properties in the form of shear and rigid zones. The main motivation of using the three-field formulation for Bingham fluids by pointing out the limitations of the standard two-field formulation is described. The corresponding strong as well as weak formulations are also presented in this chapter.

Chapter 3 includes the detailed understanding of finite element methods for simple Poisson's equation. Moreover, the space discretization of the Bingham three-field formulation problem has been discussed. Afterwards, the choice of the finite elements for three-field Stokes problem and some stabilization techniques (e.g. edge oriented and artificial diffusion stabilization) are presented at the end of the chapter.

Chapter 4 provides an introduction of the monolithic (non-linear and linear) solvers. The non-linearity is treated with the discrete Newton with divided difference evaluation of the Jacobian. The resulting linear subproblem is handled by a linear solver, which can be direct or iterative i.e. UMFPACK or geometric multigrid, respectively. A detailed numerical study is also presented in this chapter regarding the inf-sup stability conditions of three-field Stokes problem for the "flow around cylinder configuration".

Chapter 5 presents the numerical results of Bingham fluid flow in a channel for direct and iterative solver. Moreover, to analyse the behaviour of the solver, a detailed parametric optimization study for the multigrid solver is performed. The effects of adding the stabilization (edge-oriented and artificial diffusion) on the solver is also investigated for the same flow configuration.

Chapter 6 is devoted to the insights of our newly developed adaptive discrete Newton approach for any nonlinear problem. A comprehensive description of the efficiency and the robustness of this method is explained with the help of graphical representation of the solver's behaviour. Several comparison studies for different benchmark configurations are carried out between classical and the new adaptive discrete Newton.

Chapter 7 summarizes the conclusions and provides the references at the end.

1.5 Already Published Contributions

- [22] A. Fatima, S. Turek, A. Ouazzi, M. A. Afaq, An adaptive discrete Newton method for regularization-free Bingham model, in: Book of Extended Abstracts of the 6th ECCOMAS Young Investigators Conference 7th-9th July 2021, Valencia, Spain, Editorial Universitat Politècnica de Valencia, 2021, pp. 180–189.
- [23] M. A. Afaq, S. Turek, A. Ouazzi, A. Fatima, Monolithic Newton-multigrid solver for multiphase flow problems with surface tension, in: Book of Extended Abstracts of the 6th ECCOMAS Young Investigators Conference 7th-9th July 2021, Valencia, Spain, Editorial Universitat Politècnica de Valencia, 2021, pp. 190–199.
- [24] A. Fatima, H. Damanik, S. Turek, R. Wolff, J. Rudloff, M. Lang, T. Hochrein, and M. Bastian. Mit Simulation zu neuen Materialien. Kunststoffe, 09/2021, 2021.

CHAPTER 1. MOTIVATION

Chapter 2

Mathematical Modelling for Bingham Viscoplastic Fluids

2.1 Classification of the Fluids

Fluids are found everywhere as an essential part of our daily life and almost everything consists of fluid. The fluids are classified in two major categories i.e. Newtonian and non-Newtonian. This classification depends on the relation between shear rate ($\frac{du}{dy}$ or $\dot{\gamma}$) and the shear stress ($\boldsymbol{\tau}$). Which describes, how the fluid behaves in response to the applied stress. A compact depiction of the classification of the fluids is shown in Fig. 2.1. One can see, that the Newtonian fluids follow a linear relation between shear stress and the deformation rate. In the Newtonian fluids, the stress tensor $\boldsymbol{\tau}$ is expressed by

$$\boldsymbol{\tau} = -p\mathbf{I} + 2\eta\mathbf{D}, \quad (2.1)$$

here, p is the pressure field, η is the viscosity and \mathbf{D} is the deformation tensor. The flow characteristic can be explained with the help of Navier-Stokes equations, which consist of mass balance and force balance laws. The Navier-Stokes (NS) equations for a viscous incompressible homogeneous flow in its strong form reads:

$$\begin{cases} \frac{\partial \mathbf{u}}{\partial t} + \mathbf{u} \cdot \nabla \mathbf{u} - \nabla \cdot \boldsymbol{\tau} + \nabla p = 0 & \text{in } \Omega \\ \nabla \cdot \mathbf{u} = 0 & \text{in } \Omega \\ \mathbf{u} = \mathbf{g}_D & \text{on } \Gamma_D \end{cases} \quad (2.2)$$

CHAPTER 2. MATHEMATICAL MODELLING FOR BINGHAM VISCOPLASTIC FLUIDS

Here, \mathbf{u} is the velocity field, $\boldsymbol{\tau}$ is the total stress tensor and Γ is boundary of a domain (depends on the geometry). The deformation tensor form of the NS equations can be equivalently written as:

$$\left\{ \begin{array}{ll} \frac{\partial \mathbf{u}}{\partial t} + \mathbf{u} \cdot \nabla \mathbf{u} - \nabla \cdot 2\mu \mathbf{D}(\mathbf{u}) + \nabla p = 0 & \text{in } \Omega \\ \nabla \cdot \mathbf{u} = 0 & \text{in } \Omega \\ \mathbf{u} = \mathbf{g}_D & \text{on } \Gamma_D \end{array} \right. \quad (2.3)$$

The fluids, which do not follow the linear relation are categorized as non-Newtonian fluids, also called as generalized non-Newtonian fluids, involving at least a non-linear viscosity term inside the constitutive equation as follows:

$$\boldsymbol{\tau} = -pI + 2\eta(\|\mathbf{D}\|)\mathbf{D}.$$

These types of non-linear viscosities appear in the equations of the fluids like Power law model, Carreau model [25, 26, 27]. One kind of such fluid is shear thickening, which increases its resistance and shows friction with increasing the applied stress. Mathematically described with the Power law model, containing the power index n greater than 1 as follows:

$$\eta = -2\mu \|\mathbf{D}\|^{n-1} \quad n > 1.$$

On the contrary, shear thinning fluids decreases its resistance, when the applied stress is increased e.g. pseudoplastic fluids. Bingham plastic is the limited case of such fluids, which requires a finite value of the applied stress τ_s before it begins to flow.

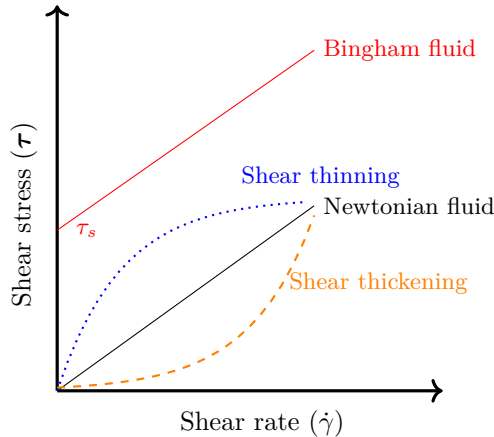


Figure 2.1: Classifications of the fluids w.r.t. shear stress and shear rate

2.2 Bingham Viscoplastic Fluid

This section describes the characteristics of the Bingham fluids in details. A Bingham viscoplastic fluid is defined as: A fluid that requires the applied stress above a certain non-zero limit of the yield stress to deform and to start flowing like a fluid. Below this non-zero limit of the yield stress, the fluid behaves like a solid. The difference of such behaviour can be observed from the constitutive law of Bingham fluids (dependent on the yield stress properties) defined as:

$$\boldsymbol{\tau} = \begin{cases} 2\eta\mathbf{D}(\mathbf{u}) + \tau_s \frac{\mathbf{D}(\mathbf{u})}{\|\mathbf{D}(\mathbf{u})\|} & \text{if } \|\mathbf{D}(\mathbf{u})\| \neq 0 \\ \|\boldsymbol{\tau}\| \leq \tau_s & \text{if } \|\mathbf{D}(\mathbf{u})\| = 0 \end{cases} \quad (2.4)$$

where $\mathbf{D}(\mathbf{u}) = \frac{1}{2}(\nabla\mathbf{u} + (\nabla\mathbf{u})^T)$ denotes the strain rate tensor, and τ_s denotes the yield stress. It is the simplest model, that describes the nature of the viscoplastic fluids. The equation (2.4) basically represents the straight line behaviour which has τ_s as y-intercept and exhibits a linear relation afterwards, presented in Fig. 2.1. The first part of this constitutive law describes the shear region, where fluid behaves as a liquid. Whereas, the second part describes the rigid or plug zone, where the fluid behaves as solid or moves with constant velocity. This law can be equivalently written as:

$$\mathbf{D} = \begin{cases} \frac{1}{2\eta} \left(1 - \frac{\tau_s}{\|\boldsymbol{\tau}\|}\right) \boldsymbol{\tau} & \text{if } \|\boldsymbol{\tau}\| > \tau_s \\ 0 & \text{if } \|\boldsymbol{\tau}\| \leq \tau_s \end{cases} \quad (2.5)$$

In recent years, the attention has been increased significantly for solving the Bingham fluids numerically because of its presence in the industry as well as in many phenomena of nature [28, 29]. There are categorically two methods, that has been proposed to solve Bingham fluids: Direct regularization techniques [30, 21, 31] and Lagrange multiplier approach (Uzawa method [17], augmented Lagrangian method [32, 20] and penalty-Newton-Uzawa-CG method [33]). In this work, the regularization technique is used for solving the Bingham fluid flow, discussed in the next section.

2.2.1 Regularization Techniques and Three-Field Formulation

It is well-known from the literature that due to the plug region it is very difficult to model the Bingham constitutive law for viscoplastic fluids mathematically. The main problem arises due to the non-differentiability of the viscosity in the constitutive law and needs to be treated in a special way. The constitutive law in eq. (2.4) consists of the non-linear viscosity:

$$\eta(\|\mathbf{D}(\mathbf{u})\|) = 2\eta + \frac{\tau_s}{\|\mathbf{D}(\mathbf{u})\|} \quad (2.6)$$

CHAPTER 2. MATHEMATICAL MODELLING FOR BINGHAM VISCOPLASTIC FLUIDS

The problem of differentiability arises when the viscosity becomes infinite in the rigid zone, i.e. $\|\mathbf{D}(\mathbf{u})\| = 0$. Therefore, one approach is to use regularization to overcome this problem. The purpose is to make the viscosity smooth and differentiable over the whole domain. There are various regularization models in the literature e.g. Allouche et al. [34] introduced a regularization parameter simply added in the denominator as

$$\eta_\epsilon(\|\mathbf{D}(\mathbf{u})\|)_\epsilon = 2\eta + \frac{\tau_s}{\epsilon + \|\mathbf{D}(\mathbf{u})\|}. \quad (2.7)$$

Bercovier and Engelman [18] proposed a different regularization function as

$$\eta_\epsilon(\|\mathbf{D}(\mathbf{u})\|) = 2\eta + \frac{\tau_s}{\sqrt{\epsilon^2 + \|\mathbf{D}(\mathbf{u})\|^2}}. \quad (2.8)$$

Papanastasiou [19] proposed an exponential expression in the regularization model which is valid for any shear rate

$$\eta_\epsilon(\|\mathbf{D}(\mathbf{u})\|) = 2\eta + \frac{\tau_s(1 - e^{-\frac{\|\mathbf{D}(\mathbf{u})\|}{\epsilon}})}{\|\mathbf{D}(\mathbf{u})\|}. \quad (2.9)$$

Tanner et al. [35] proposed a different model called bi-viscous model formed by:

$$\eta_\epsilon(\|\mathbf{D}(\mathbf{u})\|) = \begin{cases} (2\eta + \frac{\tau_s}{\|\mathbf{D}(\mathbf{u})\|}) & \text{if } \|\mathbf{D}(\mathbf{u})\| \geq \epsilon\tau_s \\ \frac{2\eta}{\epsilon} & \text{if } \|\mathbf{D}(\mathbf{u})\| \leq \epsilon\tau_s \end{cases} \quad (2.10)$$

After adding one of the above mentioned regularization techniques, the corresponding Navier-Stokes equations for the steady incompressible Bingham flow reads:

$$\begin{cases} -\nabla \cdot \boldsymbol{\tau} + \nabla p = 0 & \text{in } \Omega \\ \nabla \cdot \mathbf{u} = 0 & \text{in } \Omega \\ \mathbf{u} = \mathbf{g}_D & \text{on } \Gamma_D \end{cases} \quad (2.11)$$

where $\boldsymbol{\tau}$ is stress tensor from eq. (2.4) with regularized viscosity. It is already discussed above, that the rigid zone inside the flow regimes produces a singularity. In the present work, we use the Bercovier and Engelman (eq. 2.8) regularization function to overcome this problem.

A wide range of computational iterative schemes is available and can be used for numerical approximations of regularized system of equations. Generally in the regularization approach, solvers do not perform efficiently, when the regularization parameter ϵ gets very small but the real viscoplastic solution can only be achieved when $\epsilon \rightarrow 0$, which is a very difficult situation for the numerical solver. For the remedy of such problem, we use a formulation introducing a new auxiliary stress tensor ($\boldsymbol{\sigma}$) [1]. The corresponding three-field formulation

2.3. VARIATIONAL FORMULATION

of yield stress fluids leads to a regularization-free Bingham model. Hence, we proceed within the framework of a three-field Stokes problem defined as follows:

$$\boldsymbol{\sigma} = \frac{\mathbf{D}(\mathbf{u})}{\|\mathbf{D}(\mathbf{u})\|_\epsilon} \quad (2.12)$$

Then, the three-field $(\mathbf{u}, \boldsymbol{\sigma}, p)$ system of stationary Bingham fluid flow equations is given as follows:

$$\begin{cases} \|\mathbf{D}(\mathbf{u})\|_\epsilon \boldsymbol{\sigma} - \mathbf{D}(\mathbf{u}) = 0 & \text{in } \Omega \\ -\nabla \cdot (2\eta \mathbf{D}(\mathbf{u}) + \tau_s \boldsymbol{\sigma}) + \nabla p = 0 & \text{in } \Omega \\ \nabla \cdot \mathbf{u} = 0 & \text{in } \Omega \\ \mathbf{u} = \mathbf{g}_D & \text{on } \Gamma_D \end{cases} \quad (2.13)$$

System (2.13) represents the mixed formulation, which solves the regularized as well as the regularization-free Bingham problem, i.e. $\epsilon = 0$. This formulation over comes not only the problem for the numerical solver but also helps to achieve accurate solution. The numerical studies shown in the next sections describe the advantages of this three-field formulation, particularly that we can achieve a true viscoplastic solution by solving a regularization-free Bingham model. The resulting saddle-point problem is solved efficiently and accurately by a monolithic finite element method.

2.3 Variational Formulation

In the present work, the finite element method is chosen for the discretization in space. For this purpose, the strong form of the corresponding system of equations is converted into the weak formulation by multiplying the test functions [36] and integrated over the whole domain.

2.3.1 The Weak Form of Navier-Stokes Equations

We consider the two test functions \mathbf{v}, q for the stationary incompressible Newtonian flow and multiply with the system of equations (2.3). Then, the resulting weak forms read:

$$\begin{aligned} \int_{\Omega} \left(\mathbf{u} \cdot \nabla \mathbf{u} - \nabla \cdot 2\eta \mathbf{D}(\mathbf{u}) + \nabla p \right) \mathbf{v} \, dx &= 0 \quad \text{in } \Omega \\ \int_{\Omega} \nabla \cdot \mathbf{u} \, q \, dx &= 0 \quad \text{in } \Omega \end{aligned} \quad (2.14)$$

Let $\mathbb{V} = \mathbf{H}_0^1(\Omega) := (H_0^1(\Omega))^2$ and $\mathbb{Q} = L_0^2(\Omega)$ be the spaces for the velocity and pressure, respectively, and let \mathbb{V}', \mathbb{Q}' , be their corresponding dual spaces. We

CHAPTER 2. MATHEMATICAL MODELLING FOR BINGHAM VISCOPLASTIC FLUIDS

introduce the following linear forms: \mathcal{A}_u , \mathcal{N}_u and \mathcal{L}_u defined on $\mathbb{V} \rightarrow \mathbb{V}'$ as follows

$$\begin{aligned} \langle \mathcal{N}_u \mathbf{u}, \mathbf{v} \rangle &= \int_{\Omega} (\mathbf{u} \cdot \nabla \mathbf{u}) \mathbf{v} \, dx, & \forall \mathbf{u}, \mathbf{v} \in \mathbb{V} \\ \langle \mathcal{L}_u \mathbf{u}, \mathbf{v} \rangle &= \int_{\Omega} 2\eta \mathbf{D}(\mathbf{u}) : \mathbf{D}(\mathbf{v}) \, dx, & \forall \mathbf{u}, \mathbf{v} \in \mathbb{V} \end{aligned} \quad (2.15)$$

and we set

$$\mathcal{A}_u := \mathcal{N}_u + \mathcal{L}_u, \quad (2.16)$$

the following linear forms: \mathcal{B} defined on $\mathbb{V} \rightarrow \mathbb{Q}'$ as follows

$$\langle \mathcal{B} \mathbf{u}, q \rangle = - \int_{\Omega} \nabla \cdot \mathbf{u} \, q \, dx, \quad \forall \mathbf{u} \in \mathbb{V}, q \in \mathbb{Q} \quad (2.17)$$

We define the bilinear forms $a(\cdot, \cdot)$ defined on $\mathbb{V} \times \mathbb{V} \rightarrow \mathbb{R}$ and $b(\cdot, \cdot)$ defined on $\mathbb{V} \times \mathbb{Q} \rightarrow \mathbb{R}$ reads; for $\mathcal{U} = (\mathbf{u})$ and $\mathcal{V} = (\mathbf{v})$

$$\begin{aligned} a(\mathcal{U}, \mathcal{V}) &= \langle \mathcal{A}_u \mathbf{u}, \mathbf{v} \rangle, \\ b(\mathcal{U}, q) &= b(\mathbf{u}, q). \end{aligned} \quad (2.18)$$

The weak formulation for the classical Navier-Stokes system (2.3) reads:
Find $(\mathcal{U}, p) \in \mathbb{V} \times \mathbb{Q}$ *s.t.*

$$\begin{cases} a(\mathcal{U}, \mathcal{V}) + b(\mathcal{V}, p) = 0 & \forall \mathcal{V} \in \mathbb{V}, \\ b(\mathcal{U}, q) = 0 & \forall q \in \mathbb{Q}. \end{cases} \quad (2.19)$$

2.3.2 The Weak Form of Bingham Three-Field Formulation

We consider the three test functions \mathbf{v} , q and $\boldsymbol{\tau}$ for velocity, pressure and stress, respectively, and multiply with the system of equations (2.13). Then, the resulting weak forms read:

$$\begin{aligned} \int_{\Omega} \left(\|\mathbf{D}(\mathbf{u})\|_{\epsilon} \boldsymbol{\sigma} - \mathbf{D}(\mathbf{u}) \right) \boldsymbol{\tau} \, dx &= 0 \quad \text{in } \Omega \\ \int_{\Omega} \left(-\nabla \cdot \left(2\eta \mathbf{D}(\mathbf{u}) + \tau_s \boldsymbol{\sigma} \right) + \nabla p \right) \mathbf{v} \, dx &= 0 \quad \text{in } \Omega \\ \int_{\Omega} \nabla \cdot \mathbf{u} \, q \, dx &= 0 \quad \text{in } \Omega \end{aligned} \quad (2.20)$$

For simplicity, we consider $u = 0$ at Γ_D and after taking the integration by parts for the second order derivative and pressure term, the simplified weak

2.3. VARIATIONAL FORMULATION

formulation reads:

$$\begin{aligned}
\int_{\Omega} \left(\|\mathbf{D}(\mathbf{u})\|_{\epsilon} \boldsymbol{\sigma} : \boldsymbol{\tau} \right) dx - \int_{\Omega} \left(\mathbf{D}(\mathbf{u}) : \boldsymbol{\tau} \right) dx &= 0 \quad \text{in } \Omega \\
\int_{\Omega} \left(2\eta \mathbf{D}(\mathbf{u}) : \mathbf{D}(\mathbf{v}) \right) dx + \int_{\Omega} \left(\tau_s \mathbf{D}(\mathbf{v}) : \boldsymbol{\sigma} \right) dx - \int_{\Omega} p \nabla \cdot \mathbf{v} dx &= 0 \quad \text{in } \Omega \\
\int_{\Omega} q \nabla \cdot \mathbf{u} dx &= 0 \quad \text{in } \Omega
\end{aligned} \tag{2.21}$$

Let $\mathbb{V} = \mathbf{H}_0^1(\Omega) := (H_0^1(\Omega))^2$, $\mathbb{Q} = L_0^2(\Omega)$, and $\mathbb{M} = (L^2(\Omega))_{\text{sym}}^{2 \times 2}$ be the spaces for the velocity, pressure and stress, respectively associated with $\|\cdot\|_{1,\Omega}$ and $\|\cdot\|_{0,\Omega}$. Let \mathbb{V}' , \mathbb{Q}' , and \mathbb{M}' be their corresponding dual spaces. Furthermore, we set $\mathbb{X} := \mathbb{V} \times \mathbb{M}$ and $\mathbb{X}' := \mathbb{V}' \times \mathbb{M}'$. We introduce the following linear forms:

\mathcal{A}_1 defined on $\mathbb{V} \rightarrow \mathbb{V}'$

$$\langle \mathcal{A}_1 \mathbf{u}, \mathbf{v} \rangle := \int_{\Omega} 2\eta \mathbf{D}(\mathbf{u}) : \mathbf{D}(\mathbf{v}) dx \tag{2.22}$$

\mathcal{A}_2 defined on $\mathbb{X} \rightarrow \mathbb{X}'$

$$\langle \mathcal{A}_2 \boldsymbol{\sigma}, \boldsymbol{\tau} \rangle = \int_{\Omega} \tau_s \|\mathbf{D}(\mathbf{u})\|_{\epsilon} \boldsymbol{\sigma} : \boldsymbol{\tau} dx \tag{2.23}$$

The associated bilinear forms $a_1(\cdot, \cdot)$ and $a_2(\cdot, \cdot)$ defined on $\mathbb{V} \rightarrow \mathbb{V}'$ and $\mathbb{M} \rightarrow \mathbb{M}'$

$$a_1(\mathbf{u}, \mathbf{v}) = \langle \mathcal{A}_1 \mathbf{u}, \mathbf{v} \rangle, \quad a_2(\boldsymbol{\sigma}, \boldsymbol{\tau}) = \langle \mathcal{A}_2 \boldsymbol{\sigma}, \boldsymbol{\tau} \rangle$$

Let B_1 and B_2 defined on $\mathbb{V} \rightarrow \mathbb{Q}'$ and $\mathbb{V} \rightarrow \mathbb{M}'$

$$\langle \mathcal{B}_1 \mathbf{v}, q \rangle := - \int_{\Omega} \nabla \cdot \mathbf{v} q dx \quad , \quad \langle \mathcal{B}_2 \mathbf{v}, \boldsymbol{\sigma} \rangle := - \int_{\Omega} \tau_s \mathbf{D}(\mathbf{v}) : \boldsymbol{\sigma} dx \tag{2.24}$$

$$\langle \mathcal{A}(\mathbf{u}, \boldsymbol{\sigma}), (\mathbf{v}, \boldsymbol{\tau}) \rangle = \langle \mathcal{A}_1 \mathbf{u}, \mathbf{v} \rangle + \langle \mathcal{A}_2 \boldsymbol{\sigma}, \boldsymbol{\tau} \rangle + \langle \mathcal{B}_2^T \mathbf{v}, \boldsymbol{\sigma} \rangle + \langle \mathcal{B}_2 \mathbf{u}, \boldsymbol{\tau} \rangle$$

The corresponding operator form reads:

$$\begin{bmatrix} \mathcal{A}_1 & \mathcal{B}_2^T & \mathcal{B}_1^T \\ \mathcal{B}_2 & -\mathcal{A}_2 & \mathbf{0} \\ \mathcal{B}_1 & \mathbf{0} & \mathbf{0} \end{bmatrix} \begin{bmatrix} \mathbf{u} \\ \boldsymbol{\sigma} \\ p \end{bmatrix} = \begin{bmatrix} rhs_{\mathbf{u}} \\ rhs_{\boldsymbol{\sigma}} \\ rhs_p \end{bmatrix}$$

The associated bilinear form for $\mathcal{U} = (\mathbf{u}, \boldsymbol{\sigma})$ and $\mathcal{V} = (\mathbf{v}, \boldsymbol{\tau})$ are

$$a(\mathcal{U}, \mathcal{V}) = a_1(\mathbf{u}, \mathbf{v}) + a_2(\boldsymbol{\sigma}, \boldsymbol{\tau}) + b_2(\mathbf{v}, \boldsymbol{\sigma}) + b_2(\mathbf{u}, \boldsymbol{\tau})$$

Find $(\mathcal{U}, p) \in \mathbb{X} \times \mathbb{Q}$ such that:

$$\begin{cases} a(\mathcal{U}, \mathcal{V}) + b(\mathcal{V}, p) = \langle \mathbf{f}, \mathcal{V} \rangle & \forall \mathcal{V} \in \mathbb{X} \\ b(\mathcal{U}, q) = \langle \mathbf{g}, q \rangle & \forall q \in \mathbb{Q} \end{cases} \tag{2.25}$$

CHAPTER 2. MATHEMATICAL MODELLING FOR BINGHAM VISCOPLASTIC FLUIDS

2.3.3 Existence and Uniqueness of Solution

In the work of Aposporidis et al. [1], it is shown that the weak formulation of the three-field Bingham (2.25) is equivalent to the weak formulation of the two-field Bingham with the regularized viscosity approach i.e. eq. (2.8) and (2.4) in the reference article. The following theorem states the well-posedness for the weak form of eq. (2.13)

Theorem 1 (for proof see [1])

The mixed formulation has a unique solution $\{\mathbf{u}, \boldsymbol{\sigma}, p\}$ from $\mathbf{H}_0^1 \times (L_{\text{sym}}^2)^{2 \times 2} \times L_0^2$ such that

$$\|\mathbf{u}\|_1^2 + \epsilon \tau_s \|\boldsymbol{\sigma}\|^2 \leq \|f\|_{-1}, \quad \|p\|_0 \leq c(\|f\|_{-1} + \tau_s \min\{1, \epsilon^{-1} \|f\|_{-1}\}). \quad (2.26)$$

where ϵ is a regularization parameter and c is a constant. Moreover, $\boldsymbol{\sigma} \in (L_{\text{sym}}^\infty)^{2 \times 2}$ and $\|\boldsymbol{\sigma}\|_{L^\infty} \leq 1$.

There is no extension of this theorem for the well-posedness of regularization-free Bingham case i.e. $\epsilon = 0$. Therefore, It is still an open problem in the theory. In the coming sections, it is shown that the unique numerical solution of $(\mathbf{u}, \boldsymbol{\sigma}, p)$ in the three-field Bingham formulation is obtained in the model problem i.e. "Bingham fluid flow in a channel". The numerical solution satisfies the analytical unique solution not only for the regularized problem but also for the regularization-free Bingham problem.

2.4 Analytical Solution for Bingham flow in a Channel

This two dimensional test case provides the analytical solution of the Bingham fluid flow between infinite parallel plates, the domain is considered unit length apart and long ($h = 1$). The viscosity (η) of the fluid is considered as unity. The flow moves due to the x-component of the velocity (u_1) and the y-component of the velocity (u_2) is zero. Considering the analytical solution for velocity and pressure as:

$$u_1 = \begin{cases} \frac{1}{8} [(1 - 2\tau_s)^2 - (1 - 2\tau_s - 2y)^2] & 0 \leq y < \frac{1}{2} - \tau_s \\ \frac{1}{8} (1 - 2\tau_s)^2 & \frac{1}{2} - \tau_s \leq y \leq \frac{1}{2} + \tau_s \\ \frac{1}{8} [(1 - 2\tau_s)^2 - (2y - 2\tau_s - 1)^2] & \frac{1}{2} + \tau_s < y \leq 1 \end{cases} \quad (2.27)$$

$$p = ax + b \quad (2.28)$$

2.4. ANALYTICAL SOLUTION FOR BINGHAM FLOW IN A CHANNEL

where the slope of the pressure gradient $a = -1$ because of the linear pressure in Poiseuille theory [37]. The analytical expression for the auxiliary stress tensor $\boldsymbol{\sigma}$ is calculated as:

$$\sigma_{12} = \begin{cases} \frac{1}{\sqrt{2}} & 0 \leq y < \frac{1}{2} - \tau_s \\ -\frac{4}{\sqrt{2}}y + \frac{2}{\sqrt{2}} & \frac{1}{2} - \tau_s \leq y \leq \frac{1}{2} + \tau_s \\ -\frac{1}{\sqrt{2}} & \frac{1}{2} + \tau_s < y \leq 1 \end{cases} \quad (2.29)$$

with $\sigma_{11} = 0$, $\sigma_{22} = 0$ and $\sigma_{12} = \sigma_{21}$ due to symmetry. The solution of velocity and auxiliary stress tensor is dependent on the zones inside the channel, therefore, the expression for $\mathbf{D}(\mathbf{u})$ is calculated and the solution corresponding to the respective zone is inserted into the three-field system of equations (2.13). Keeping the definition of deformation tensor in mind i.e. $\mathbf{D}(\mathbf{u}) = \frac{1}{2}(\nabla \mathbf{u} + (\nabla \mathbf{u})^T)$, the expression for $\mathbf{D}(\mathbf{u})$ is derived as follows:

$$D_{12} = \begin{cases} \frac{1}{4} [(1 - 2\tau_s - 2y)] & 0 \leq y < \frac{1}{2} - \tau_s \\ 0 & \frac{1}{2} - \tau_s \leq y \leq \frac{1}{2} + \tau_s \\ -\frac{1}{4} [(2y - 2\tau_s - 1)] & \frac{1}{2} + \tau_s < y \leq 1 \end{cases} \quad (2.30)$$

with $D_{11} = 0$ and $D_{22} = 0$.

$$\|\mathbf{D}(\mathbf{u})\| = \begin{cases} \frac{1}{\sqrt{8}} [(1 - 2\tau_s - 2y)] & 0 \leq y < \frac{1}{2} - \tau_s \\ 0 & \frac{1}{2} - \tau_s \leq y \leq \frac{1}{2} + \tau_s \\ \frac{1}{\sqrt{8}} [(2y - 2\tau_s - 1)] & \frac{1}{2} + \tau_s < y \leq 1 \end{cases} \quad (2.31)$$

The exact solution should satisfy the system of equations (2.13) for all zones, therefore, the Newtonian and rigid zones are presented separately.

2.4.1 Newtonian Zone

$$\text{Constitutive eq} \begin{cases} \|\mathbf{D}(\mathbf{u})\|_\epsilon \sigma_{12} - D_{12} = 0 \\ \frac{1}{\sqrt{8}} [(1 - 2\tau_s - 2y)] \frac{1}{\sqrt{2}} - \frac{1}{4} [(1 - 2\tau_s - 2y)] = 0 \\ 0 = 0 \end{cases}$$

CHAPTER 2. MATHEMATICAL MODELLING FOR BINGHAM
VISCOPLASTIC FLUIDS

$$\text{Momentum eq} \left\{ \begin{array}{l} -2\eta \left(\frac{D_{11}}{\partial x} + \frac{D_{12}}{\partial x} \right) - \sqrt{2}\tau_s \left(\frac{\sigma_{11}}{\partial x} + \frac{\sigma_{12}}{\partial x} \right) + \frac{\partial p}{\partial x} = 0 \\ -2(1) \left(0 - \frac{2}{4} \right) - \sqrt{2}\tau_s (0 + 0) - 1 = 0 \\ 1 + 0 - 1 = 0 \\ 0 = 0 \\ -2\eta \left(\frac{D_{12}}{\partial y} + \frac{D_{22}}{\partial y} \right) - \sqrt{2}\tau_s \left(\frac{\sigma_{12}}{\partial y} + \frac{\sigma_{22}}{\partial y} \right) + \frac{\partial p}{\partial y} = 0 \\ -2(1) (0 + 0) - \tau_s (0 + 0) + 0 = 0 \\ 0 = 0 \end{array} \right.$$

$$\text{Continuity eq} \left\{ \begin{array}{l} \frac{\partial u_1}{\partial x} + \frac{\partial u_2}{\partial y} = 0 \\ 0 + 0 = 0 \end{array} \right.$$

2.4.2 Rigid Zone

$$\text{Constitutive eq} \left\{ \begin{array}{l} \|\mathbf{D}(\mathbf{u})\|_\epsilon \sigma_{12} - D_{12} = 0 \\ 0 \left(\frac{-4}{\sqrt{2}}y + \frac{2}{\sqrt{2}} \right) = 0 \\ 0 = 0 \end{array} \right.$$

$$\text{Momentum eq} \left\{ \begin{array}{l} 2\eta \left(\frac{D_{11}}{\partial x} + \frac{D_{12}}{\partial x} \right) - \sqrt{2}\tau_s \left(\frac{\sigma_{11}}{\partial x} + \frac{\sigma_{12}}{\partial x} \right) + \frac{\partial p}{\partial x} = 0 \\ -2(1) (0 + 0) - \sqrt{2}\tau_s \left(0 - \frac{4}{\sqrt{2}} \right) - 1 = 0 \\ 1 - 1 = 0 \\ 0 = 0 \\ -2\eta \left(\frac{D_{12}}{\partial y} + \frac{D_{22}}{\partial y} \right) - \sqrt{2}\tau_s \left(\frac{\sigma_{12}}{\partial y} + \frac{\sigma_{22}}{\partial y} \right) + \frac{\partial p}{\partial y} = 0 \\ -2(1) (0 + 0) - \tau_s (0 + 0) + 0 = 0 \\ 0 = 0 \end{array} \right.$$

$$\text{Continuity eq} \left\{ \begin{array}{l} \frac{\partial u_1}{\partial x} + \frac{\partial u_2}{\partial y} = 0 \\ 0 + 0 = 0 \end{array} \right.$$

2.4. ANALYTICAL SOLUTION FOR BINGHAM FLOW IN A CHANNEL

Hence, the analytical expression of $\boldsymbol{\sigma}, \mathbf{u}, p$ is satisfying the equations of three-field Bingham formulation. As already mentioned in subsection 2.3.3, the mixed formulation has a unique solution for the regularized problem but there is no possible extension for the well-posedness of the regularization-free problem. In the numerical results for the configuration "Bingham fluid flow in a channel" in chapter 5, we show that our monolithic numerical solver with the three-field Bingham formulation can recover the exact solution not only for the regularized but also for the regularization-free ($\epsilon = 0$) Bingham problem. Hence, one can exactly solve and obtain the unique solution of the regularization-free Bingham fluid flow at least numerically.

**CHAPTER 2. MATHEMATICAL MODELLING FOR BINGHAM
VISCOPLASTIC FLUIDS**

Chapter 3

Finite Element Method

3.1 Introduction

Several methods are available for the space discretization of any given system of equations, for example the finite difference method (FDM) [38, 39, 40], the finite volume method (FVM) [41, 42] and the finite element method (FEM) [43, 44, 45]. FEM is a new method as compared to the other methods, it was mainly used in structural mechanics but in the present era, it is also widely used in other fields (e.g. fluid dynamics, heat conduction, magnetic field and many more). The demand of this method is really high because of its flexibility to solve complex boundary value problems robustly and accurately. FEM finds the solution of a complex problem by generating an alternative weak problem: By multiplying the original differential equations to the test functions and integrating over the whole domain. Afterwards, the solution of the weak problem is approximated instead of finding the exact solution of the differential equations (strong form). Moreover, there can be different ways for the improvement of this approximated solution e.g. by refining the grid/mesh of the geometry or assuming the higher order polynomials for the interpolation. In the next section, an explanation of the fundamentals of finite element method is given, by applying it on the simple Poisson's equation.

3.2 FEM for Poisson's Equation

For understanding the finite element method in a better way, we consider a very simple steady state problem i.e. Poisson's equation, defined as follows:

$$\nabla^2 u = \frac{\partial^2 u}{\partial x^2} + \frac{\partial^2 u}{\partial y^2} = 0 \quad (3.1)$$

CHAPTER 3. FINITE ELEMENT METHOD

where "u" is the distribution of the heat in a rectangular domain $\Omega = [0, a] \times [0, b]$, shown in Fig. 3.1. The value of the temperature at the boundaries is given as

$$\begin{aligned} u(0, y) &= 100, \quad u(a, y) = 250, \\ u(x, 0) &= 50, \quad u(x, b) = 200. \end{aligned}$$

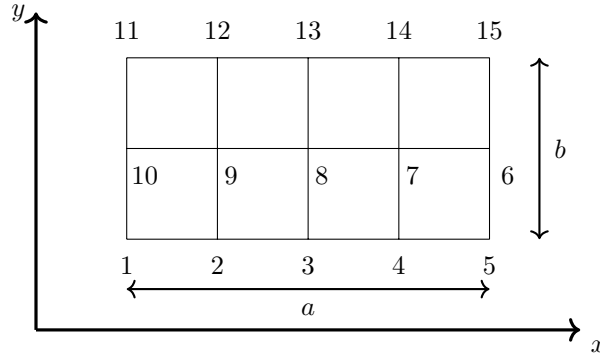


Figure 3.1: The rectangular domain with global node numbers.

The first step of the finite element method, is to multiply the weight (test) function with the equation in order to reduce the strong continuity condition on the variables. Therefore, we multiply the equation (3.1) with a test/weight function i.e. $w(x, y)$, and integrate over a random domain Ω^r , which is basically inside the solution domain Ω ($\Omega^r \in \Omega$). The resulting equation reads as follows:

$$\int_{\Omega^r} w(x, y) \left(\frac{\partial^2 u}{\partial x^2} + \frac{\partial^2 u}{\partial y^2} \right) dx dy = 0 \quad (3.2)$$

$$\int_{\Omega^r} \left(w(x, y) \frac{\partial^2 u}{\partial x^2} + w(x, y) \frac{\partial^2 u}{\partial y^2} \right) dx dy = 0 \quad (3.3)$$

By using the product rule of the following term

$$\nabla(w, \nabla u) = \nabla w \nabla u + w \nabla^2 u,$$

rearrange it as:

$$\nabla(w, \nabla u) - \nabla w \nabla u = w \nabla^2 u, \quad (3.4)$$

using the relation 3.4, we obtain the following form of the equation (3.3):

$$\int_{\Omega^r} \left(\left(\frac{\partial}{\partial x} \left[w \frac{\partial u}{\partial x} \right] - \frac{\partial w}{\partial x} \frac{\partial u}{\partial x} \right) + \left(\frac{\partial}{\partial y} \left[w \frac{\partial u}{\partial y} \right] - \frac{\partial w}{\partial y} \frac{\partial u}{\partial y} \right) \right) dx dy = 0 \quad (3.5)$$

3.2. FEM FOR POISSON'S EQUATION

rearranging the above equation as:

$$\int_{\Omega^r} \left(\left(\frac{\partial}{\partial x} \left[w \frac{\partial u}{\partial x} \right] + \frac{\partial}{\partial y} \left[w \frac{\partial u}{\partial y} \right] \right) - \left(\frac{\partial w}{\partial x} \frac{\partial u}{\partial x} + \frac{\partial w}{\partial y} \frac{\partial u}{\partial y} \right) \right) dx dy = 0 \quad (3.6)$$

To convert the volume integral into the line integral, we apply Gauss divergence theorem [46] on the first term of above equation, such that:

$$\int_{\Omega^r} \left(\frac{\partial}{\partial x} \left[w \frac{\partial u}{\partial x} \right] + \frac{\partial}{\partial y} \left[w \frac{\partial u}{\partial y} \right] \right) dx dy = \int_{\Gamma^r} \left[w \frac{\partial u}{\partial x} \right] \cdot \mathbf{n}_x + \left[w \frac{\partial u}{\partial y} \right] \cdot \mathbf{n}_y ds \quad (3.7)$$

where \mathbf{n} is the normal vectors on the boundary in outward direction. Taking the terms of boundary integral on the right hand side, we define the new term f_n as:

$$f_n = \mathbf{n}_x \frac{\partial u}{\partial x} + \mathbf{n}_y \frac{\partial u}{\partial y}$$

substituting the value in equation (3.6)

$$\int_{\Gamma^r} w f_n ds - \int_{\Omega^r} \left(\frac{\partial w}{\partial x} \frac{\partial u}{\partial x} + \frac{\partial w}{\partial y} \frac{\partial u}{\partial y} \right) dx dy = 0 \quad (3.8)$$

Then, the complete weak formulation of the equation (3.1) can be written as:

$$\int_{\Omega^r} \left(\frac{\partial w}{\partial x} \frac{\partial u}{\partial x} + \frac{\partial w}{\partial y} \frac{\partial u}{\partial y} \right) dx dy = \int_{\Gamma^r} w f_n ds \quad (3.9)$$

The strong continuity requirement is now weakened and equally shared by the weight function, that satisfies the essential boundary conditions of the domain and presents variation of the primary variable \mathbf{u} . In order to do the approximation of the solution of equation 3.9, we divide the rectangular domain Ω into the finite elements (e). The node and the edge of the elements must be common with neighbouring element except on the boundaries. The ansatz for the approximated solution \mathbf{u} of equation (3.9) can be defined as:

$$\mathbf{u}^e(x, y) = \sum_{i=1}^{n_u} \mathbf{u}_i^e \psi_i^e(x, y) \quad (3.10)$$

where \mathbf{u}_i^e is value of the solution at node i of the element e and ψ_i^e is the shape function for the interpolation of \mathbf{u} at node i within the element. The choice of the shape function must satisfy the following properties:

1. The value of the shape function $\psi_i = 1$ at node i and zero at any other nodes in the domain, where δ_{ij} is the Kronecker delta,

$$\psi_i^e(x, y) = \delta_{ij} = \begin{cases} 1 & \text{if } i = j \\ 0 & \text{if } i \neq j. \end{cases}$$

CHAPTER 3. FINITE ELEMENT METHOD

2. The sum of all the basis functions ψ_i on a local element should be equal to 1.

$$\sum_{i=1}^{n_u} \psi_i^e(x, y) = 1 \quad (3.11)$$

3. The sum of the derivatives of the shape function's should vanish at any point in the element, known as the conservation property.

$$\sum_{i=1}^{n_u} \nabla \psi_i^e(x, y) = 0 \quad (3.12)$$

After substituting the assumed solution into the equation (3.9), we get

$$\int_{\Omega^r} \left(\frac{\partial w}{\partial x} \sum_{i=1}^{n_u} \mathbf{u}_i^e \frac{\partial \psi_i^e}{\partial x} + \frac{\partial w}{\partial y} \sum_{i=1}^{n_u} \mathbf{u}_i^e \frac{\partial \psi_i^e}{\partial y} \right) dx dy = \int_{\Gamma^r} w f_n ds \quad (3.13)$$

As already mentioned, the weight function exhibits the variation of the primary variable \mathbf{u} , therefore, we can assume the same kind of shape function for the w i.e. $w_j = \psi_j$ for $j = 1, 2, 3, \dots, n$.

$$\underbrace{\int_{\Omega^r} \left(\sum_{i=1}^{n_u} \sum_{j=1}^{n_u} \mathbf{u}_i^e \frac{\partial \psi_i^e}{\partial x} \frac{\partial \psi_j^e}{\partial x} + \sum_{i=1}^{n_u} \sum_{j=1}^{n_u} \mathbf{u}_i^e \frac{\partial \psi_i^e}{\partial y} \frac{\partial \psi_j^e}{\partial y} \right) dx dy}_{\sum_{i=1}^{n_u} \sum_{j=1}^{n_u} K_{ij}^e \mathbf{u}_i^e} = \underbrace{\int_{\Gamma^r} \sum_{j=1}^{n_u} \psi_j^e f_n ds}_{F_j^e} \quad (3.14)$$

Hence, the matrix form of the equation (3.14) reads:

$$\sum_{i=1}^{n_u} \sum_{j=1}^{n_u} K_{ij}^e \mathbf{u}_i^e = F_j^e \quad (3.15)$$

In case of any external force or source term, it will be added into the right hand side of the equation. In order to construct the shape functions, the choice of the interpolation function is very important.

Choice of the interpolation function

Basis functions on the local elements are constructed from the piecewise polynomials e.g. Lagrangian polynomials [47]. It helps to construct the k^{th} order shape functions systematically, where k is any positive real number

$$L_k(x) = \prod_{i=1, i \neq j}^n \frac{x - x_i}{x_k - x_i} = \psi_k^e(x). \quad (3.16)$$

3.2. FEM FOR POISSON'S EQUATION

Here the Lagrange polynomial L is the Kronecker delta and it also satisfy the properties (3.11, 3.12) of the shape function.

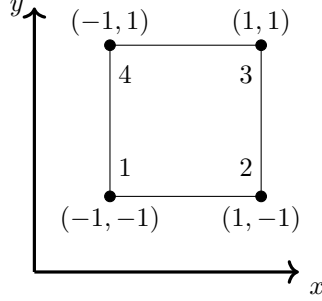


Figure 3.2: A local Q_1 quadrilateral from the rectangular domain.

For a local Q_1 quadrilateral Fig. 3.2, the interpolation functions are calculated with the Lagrange polynomial [47] as follows, where $k \neq i$:

Case 1: $k = 1, j = 1$

$$\begin{aligned}
 L_1(x_1, y_1) &= \frac{x - x_2}{x_1 - x_2} \cdot \frac{y - y_4}{y_1 - y_4} = \psi_1^e(x, y) \\
 \psi_1^e(x_1, y_1) &= \frac{x - (1)}{(-1) - 1} \cdot \frac{y - 1}{(-1) - 1} \\
 \psi_1^e(x_1, y_1) &= \frac{x - 1}{-2} \cdot \frac{y - 1}{-2} \\
 \psi_1^e(x_1, y_1) &= \frac{1 - x}{2} \cdot \frac{1 - y}{2} \\
 \psi_1^e(x_1, y_1) &= \frac{1}{4}(1 - x)(1 - y)
 \end{aligned}$$

Case 2: $k = 2, j = 2$

$$\begin{aligned}
 L_2(x_2, y_2) &= \frac{x - x_1}{x_2 - x_1} \cdot \frac{y - y_3}{y_2 - y_3} = \psi_2^e(x, y) \\
 \psi_2^e(x_2, y_2) &= \frac{x - (-1)}{1 - (-1)} \cdot \frac{y - 1}{(-1) - 1} \\
 \psi_2^e(x_2, y_2) &= \frac{x + 1}{2} \cdot \frac{y - 1}{-2} \\
 \psi_2^e(x_2, y_2) &= \frac{x + 1}{2} \cdot \frac{1 - y}{2} \\
 \psi_2^e(x_2, y_2) &= \frac{1}{4}(1 + x)(1 - y)
 \end{aligned}$$

CHAPTER 3. FINITE ELEMENT METHOD

Case 3: $k = 3, j = 3$

$$\begin{aligned}
 L_3(x_3, y_3) &= \frac{x - x_4}{x_3 - x_4} \cdot \frac{y - y_2}{y_3 - y_2} = \psi_3^e(x, y) \\
 \psi_3^e(x_3, y_3) &= \frac{x - (-1)}{1 - (-1)} \cdot \frac{y - (-1)}{(1) - (-1)} \\
 \psi_3^e(x_3, y_3) &= \frac{x + 1}{2} \cdot \frac{y + 1}{2} \\
 \psi_3^e(x_3, y_3) &= \frac{x + 1}{2} \cdot \frac{1 + y}{2} \\
 \psi_3^e(x_3, y_3) &= \frac{1}{4}(1 + x)(1 + y)
 \end{aligned}$$

Case 4: $k = 4, j = 4$

$$\begin{aligned}
 L_4(x_4, y_4) &= \frac{x - x_3}{x_4 - x_3} \cdot \frac{y - y_1}{y_4 - y_1} = \psi_4^e(x, y) \\
 \psi_4^e(x_4, y_4) &= \frac{x - 1}{-1 - 1} \cdot \frac{y - (-1)}{1 - (-1)} \\
 \psi_4^e(x_4, y_4) &= \frac{x - 1}{-2} \cdot \frac{y + 1}{2} \\
 \psi_4^e(x_4, y_4) &= \frac{1 - x}{2} \cdot \frac{1 + y}{2} \\
 \psi_4^e(x_4, y_4) &= \frac{1}{4}(1 - x)(1 + y)
 \end{aligned}$$

Here, x and y are the local coordinates of an element. Hence, the basis functions for a Q_1 element can be collectively written as:

$$\begin{aligned}
 \psi_1^e(x, y) &= \frac{1}{4}(1 - x)(1 - y) \\
 \psi_2^e(x, y) &= \frac{1}{4}(1 + x)(1 - y) \\
 \psi_3^e(x, y) &= \frac{1}{4}(1 + x)(1 + y) \\
 \psi_4^e(x, y) &= \frac{1}{4}(1 - x)(1 + y)
 \end{aligned} \tag{3.17}$$

The matrix K_{ij} from the equation (3.15) can be calculated with the following definition:

$$\int_{\Omega^r} \left[\frac{\partial \psi_i^e}{\partial x} \frac{\partial \psi_j^e}{\partial x} + \frac{\partial \psi_i^e}{\partial y} \frac{\partial \psi_j^e}{\partial y} \right] dx dy \tag{3.18}$$

This integration can be numerically computed through Gauss-Legendre Quadrature [48]. The integrals from equation (3.18) for the matrix K_{ij} , can be written as: For $i = 1$ and $j = 1, 2, 3, 4$

$$\int_{\Omega^r} \left(\frac{\partial \psi_1^e}{\partial x} \left[\frac{\partial \psi_1^e}{\partial x} + \frac{\partial \psi_2^e}{\partial x} + \frac{\partial \psi_3^e}{\partial x} + \frac{\partial \psi_4^e}{\partial x} \right] + \frac{\partial \psi_1^e}{\partial y} \left[\frac{\partial \psi_1^e}{\partial y} + \frac{\partial \psi_2^e}{\partial y} + \frac{\partial \psi_3^e}{\partial y} + \frac{\partial \psi_4^e}{\partial y} \right] \right) dx dy \tag{3.19}$$

3.2. FEM FOR POISSON'S EQUATION

We denote ψ_{11} as:

$$\psi_{11} = \int_{\Omega^r} \left(\frac{\partial \psi_1^e}{\partial x} \left[\frac{\partial \psi_1^e}{\partial x} \right] + \frac{\partial \psi_1^e}{\partial y} \left[\frac{\partial \psi_1^e}{\partial y} \right] \right) dx dy \quad (3.20)$$

The corresponding matrix for all the shape functions of the local element (Fig. 3.2) can be written as:

$$\begin{bmatrix} \psi_{11} & \psi_{12} & \psi_{13} & \psi_{14} \\ \psi_{21} & \psi_{22} & \psi_{23} & \psi_{24} \\ \psi_{31} & \psi_{32} & \psi_{33} & \psi_{34} \\ \psi_{41} & \psi_{42} & \psi_{43} & \psi_{44} \end{bmatrix} \begin{bmatrix} \mathbf{u}_1 \\ \mathbf{u}_2 \\ \mathbf{u}_3 \\ \mathbf{u}_4 \end{bmatrix}. \quad (3.21)$$

For writing the matrix of the global nodes, the connection details between the local and the global node numbers of an element are required. Thus, the connectivity matrix of all the elements in Fig. 3.1 is given as K_g , where g denotes the global node numbers,

$$[K_g] = \begin{bmatrix} 1 & 2 & 9 & 10 \\ 2 & 3 & 8 & 9 \\ 3 & 4 & 7 & 8 \\ 4 & 5 & 6 & 7 \\ 7 & 6 & 15 & 14 \\ 8 & 7 & 14 & 13 \\ 9 & 8 & 13 & 12 \\ 10 & 9 & 12 & 11 \end{bmatrix}, \quad (3.22)$$

consisting of the total 15 global nodes. The mapping of the first two elements are given below, describing, how the global and the local nodes are connected.

Element 1

$$\begin{bmatrix} (1, 1) & (1, 2) & (1, 3) & (1, 4) \\ (2, 1) & (2, 2) & (2, 3) & (2, 4) \\ (3, 1) & (3, 2) & (3, 3) & (3, 4) \\ (4, 1) & (4, 2) & (3, 4) & (4, 4) \end{bmatrix} \mapsto \begin{bmatrix} (1, 1) & (1, 2) & (1, 9) & (1, 10) \\ (2, 1) & (2, 2) & (2, 9) & (2, 10) \\ (9, 1) & (9, 2) & (9, 9) & (9, 10) \\ (10, 1) & (10, 2) & (10, 4) & (10, 10) \end{bmatrix}$$

Element 2

$$\begin{bmatrix} (1, 1) & (1, 2) & (1, 3) & (1, 4) \\ (2, 1) & (2, 2) & (2, 3) & (2, 4) \\ (3, 1) & (3, 2) & (3, 3) & (3, 4) \\ (4, 1) & (4, 2) & (3, 4) & (4, 4) \end{bmatrix} \mapsto \begin{bmatrix} (2, 2) & (2, 3) & (2, 8) & (2, 9) \\ (3, 2) & (3, 3) & (3, 8) & (3, 9) \\ (8, 2) & (8, 3) & (8, 8) & (8, 9) \\ (9, 2) & (9, 3) & (9, 8) & (9, 9) \end{bmatrix}$$

3.3. FINITE ELEMENT APPROXIMATIONS

The solution of such equation yields:

$$\begin{bmatrix} \mathbf{u}_7 \\ \mathbf{u}_8 \\ \mathbf{u}_9 \end{bmatrix} = \begin{bmatrix} & & \\ & K_g & \\ & & \end{bmatrix}^{-1} \begin{bmatrix} \\ \\ F \end{bmatrix}$$

3.3 Finite Element Approximations

The basics of the FEM is already explained in details in the previous section using simple Poisson's equation. In the following subsections (3.3.1) and (3.3.2), the finite element approximation for the Navier-Stokes equations and the three-field formulation of Bingham fluid is presented, respectively.

3.3.1 The Navier-Stokes Equations

For the space discretization, let the bounded domain $\Omega \subset \mathbb{R}^d$ be partitioned by a grid \mathcal{T}_h consisting of elements $K \in \mathcal{T}_h$ such that $\bar{\Omega} = (\bigcup_{K \in \mathcal{T}_h} K)$. For an element $K \in \mathcal{T}_h$, we denote by $\mathcal{E}(K)$ the set of all 1-dimensional edges of K . Let $\mathcal{E}_i := \bigcup_{K \in \mathcal{T}_h} \mathcal{E}(K)$ be the set of all interior element edges of the grid \mathcal{T}_h . For the approximation of the problem (2.19) with the finite element method, we introduce the approximation spaces \mathbb{V}^h and \mathbb{Q}^h of \mathbb{V} and \mathbb{Q} , respectively.

$$\begin{aligned} \mathbb{V}^h &= \{ \mathbf{v}_h \in \mathbb{V}, \mathbf{v}_h|_K \in (Q_2(K))^2 \}, \\ \mathbb{Q}^h &= \{ q_h \in \mathbb{Q}, q_h|_K \in P_1^{\text{disc}}(K) \}. \end{aligned} \quad (3.24)$$

The velocity and pressure fields are discretized using higher order stable Q_2/P_1^{disc} FEM [49, 50], presented in Fig. 3.4. Then the approximate problem of (2.19) reads; *Find* $(\mathcal{U}_h, p_h) \in \mathbb{V}^h \times \mathbb{Q}^h$ *s.t.*

$$\begin{cases} a(\mathcal{U}_h, \mathcal{V}_h) + b(\mathcal{V}_h, p_h) = 0 & \forall \mathcal{V}_h \in \mathbb{V}^h, \\ b(\mathcal{U}_h, q_h) = 0 & \forall q_h \in \mathbb{Q}^h. \end{cases} \quad (3.25)$$

The corresponding nonlinear discrete Navier-Stokes system reads:

$$\begin{bmatrix} \mathcal{A}_u & \mathcal{B}^T \\ \mathcal{B} & \mathbf{0} \end{bmatrix} \begin{bmatrix} \mathbf{u} \\ p \end{bmatrix} = \begin{bmatrix} \text{rhs}_u \\ \text{rhs}_p \end{bmatrix}, \quad (3.26)$$

where

$$\mathcal{A}_u := \mathcal{L}_u + \mathcal{N}_u, \quad (3.27)$$

here, \mathcal{L}_u is the discrete diffusion and \mathcal{N}_u is the discrete nonlinear transport operator w.r.t. \mathbf{u} . Moreover, \mathcal{B} is the vectorial discrete divergence operator.

3.3.2 The Bingham Three-Field Formulation

This section is devoted for the implementation of the finite element approximation of the three-field Bingham model. The strong form of the system of equations in (2.13) is converted into the weak formulation by multiplying it with the test functions and integrated over the whole domain (already developed in section 2.3). Let the bounded domain $\Omega \subset \mathbb{R}^d$ be partitioned by a *grid* \mathcal{T}_h consisting of elements $K \in \mathcal{T}_h$ such that $\bar{\Omega} = (\bigcup_{K \in \mathcal{T}_h} K)$. For an element $K \in \mathcal{T}_h$, we denote by $\mathcal{E}(K)$ the set of all 1-dimensional edges of K . Let $\mathcal{E}_i := \bigcup_{K \in \mathcal{T}_h} \mathcal{E}(K)$ be the set of all interior element edges of the grid \mathcal{T}_h . We introduce the approximation spaces as:

$$\begin{aligned} \mathbb{V}^h &= \{ \mathbf{v}_h \in \mathbb{V}, \mathbf{v}_{h|K} \in (Q_2(K))^2 \} \\ \mathbb{M}^h &= \{ \boldsymbol{\tau}_h \in \mathbb{M}, \boldsymbol{\sigma}_{h|K} \in (Q_2(K))^{2 \times 2} \} \\ \mathbb{Q}^h &= \{ q_h \in \mathbb{Q}, q_{h|K} \in P_1^{\text{disc}}(K) \} \end{aligned} \quad (3.28)$$

The velocity, stress and pressure are discretized using $Q_2, Q_2, P_1^{\text{disc}}$ finite elements, respectively, as shown in Figure 3.4. $Q_2(K)$ is the bi-quadratic space on the quadrilateral K with nine degrees of freedom located at vertices, mid points and in the center of the edges of quads, is defined as:

$$Q_2(K) = \{ q \circ F_K^{-1} : q \in \text{span} \langle 1, x, y, xy, x^2, y^2, x^2y, xy^2, x^2y^2 \rangle \} \quad (3.29)$$

The $P_1(K)$ is defined as:

$$P_1(K) = \{ q \circ F_K^{-1} : \text{span} \langle 1, x, y \rangle \} \quad (3.30)$$

with three degrees of freedom at the centre of the quadrilateral containing function's value and its partial derivatives. For the pressure element, if the transformation (F_K^{-1}) is being performed from real to reference coordinates, then the resulting linear function along with the Q_2 bilinear mapping, does not contain the full bilinear basis. This affects the order of approximation of the finite element method. Therefore, to cure such problem, consider (ξ, η) as the local coordinate system by joining the midpoints of the opposite faces of the element K [51, 52, 53], The $P_1(K)$ is now defined as; .

$$P_1(K) = \text{span}\{1, \xi, \eta\} \quad (3.31)$$

Consequently, the approximation method turns out to be second order (in interpolation error) not only for the velocity but also for the pressure field.

$$\|p - p_h\|_0 = O(h^2) \quad \text{and} \quad \|\mathbf{u} - \mathbf{u}_h\|_0 = O(h^2) \quad (3.32)$$

The approximate discrete problem is now defined as: Find $(\mathcal{U}_h, p_h) \in \mathbb{X}^h \times \mathbb{Q}^h$ such that:

$$\begin{cases} a(\mathcal{U}_h, \mathcal{V}_h) + b(\mathcal{V}_h, p_h) = \langle \mathbf{f}, \mathcal{V}_h \rangle & \forall \mathcal{V}_h \in \mathbb{X}^h \\ b(\mathcal{U}_h, q_h) = \langle \mathbf{g}, q_h \rangle & \forall q_h \in \mathbb{Q}^h \end{cases} \quad (3.33)$$

3.4. STABILITY OF THE FINITE ELEMENTS

We introduce the discrete solutions for $\mathbf{u}_h, \boldsymbol{\sigma}_h$ and p_h , respectively as follows:

$$\mathbf{u}_h = \sum_{i=1}^{NN_{\mathbf{u}}} \mathbf{u}_i v_i \quad \boldsymbol{\sigma}_h = \sum_{i=1}^{NN_{\boldsymbol{\sigma}}} \boldsymbol{\sigma}_i \phi_i \quad p_h = \sum_{i=1}^{NN_p} p_i \psi_i \quad (3.34)$$

Here NN denotes the number of unknown nodes in each element and v_i, ϕ_i and ψ_i are the basis functions. By keeping the test and basis functions same, the discrete formulation will be similar to the system (2.25) and will provide an approximate solution.

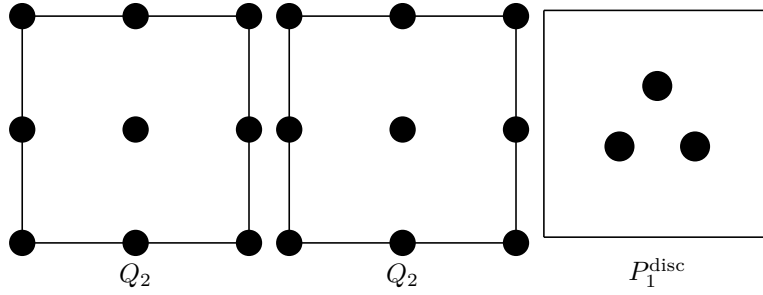


Figure 3.4: Finite elements $Q_2, Q_2, P_1^{\text{disc}}$ for the velocity, stress and pressure, respectively, on each quadrilateral.

3.4 Stability of the Finite Elements

The chosen FEM spaces for the field variables should satisfy the LBB stability conditions [54]. In the present work, the choice of the elements for the velocity and pressure are compatible according to the LBB (inf-sup) condition.

$$\sup_{\mathbf{u} \in \mathbb{V}^h} \frac{\int_{\Omega} \nabla \cdot \mathbf{u} q dx}{\|\mathbf{u}\|_{1,\Omega}} \geq \alpha \|q\|_{0,\Omega} \quad \forall q \in \mathbb{Q}^h \quad (3.35)$$

In the three-field Stokes problem, the compatibility condition for the velocity-stress [55] variables should also satisfy such that:

$$\sup_{\boldsymbol{\sigma} \in \mathbb{W}^h} \frac{\int_{\Omega} \nabla \cdot \boldsymbol{\sigma} \mathbf{u} dx}{\|\boldsymbol{\sigma}\|_{0,\Omega}} \geq \gamma \|\mathbf{u}\|_{1,\Omega} \quad \forall \mathbf{u} \in \mathbb{V}^h \quad (3.36)$$

where α and γ are the mesh independent parameters, $\|\cdot\|_{1,\Omega}$ and $\|\cdot\|_{0,\Omega}$ are the standard $H^1(\Omega), L^2(\Omega)$ norms and $\mathbb{W}^h \subset (L^2(\Omega))^4$, respectively. According to Fortin and Pierre [56], when the solvent viscosity terms vanishes in the problem (e.g. viscoelastic fluid) then the approximation spaces of the discrete problem should satisfy the following properties:

CHAPTER 3. FINITE ELEMENT METHOD

- **Condition 1:** The velocity-pressure spaces must be compatible with respect to estimate (3.35).
- **Condition 2:** If the stress tensor $\boldsymbol{\sigma}$ is approximated by a discontinuous FEM space, the deformation tensor must be a member of the same space

$$\mathbf{D}(\mathbf{u}) = \frac{1}{2}(\nabla \mathbf{u} + (\nabla \mathbf{u})^T) \in \mathbb{M}^h, \forall \mathbf{u} \in \mathbb{V}^h. \quad (3.37)$$

- **Condition 3:** If the same tensor is approximated by a continuous FEM space, the number of local degrees of freedom must be larger than the velocity space.

In our work, the choice of the FEM pair for the velocity-pressure satisfies the condition 1, whereas, there are some proposed solutions [57, 58] in the form of different element types for the fulfilment of the second and the third conditions. Moreover, Baranger et al. [59] proposes that there is no need of inf-sup condition on the non-Newtonian extra stress tensor (i.e. condition 2 and 3) unless the solvent viscosity (η) vanishes. They define a three-field Stokes discrete problem as:

Find $(\boldsymbol{\sigma}_h, \mathbf{u}_h, p_h) \in \mathbb{M}^h \times \mathbb{V}^h \times \mathbb{Q}^h$ such that:

$$\left\{ \begin{array}{ll} (\boldsymbol{\sigma}_h, \boldsymbol{\tau}_h) - 2\alpha(\mathbf{D}(\mathbf{u}_h), \boldsymbol{\tau}_h) = 0 & \forall \boldsymbol{\tau}_h \in \mathbb{M}^h \\ (\boldsymbol{\sigma}_h, \mathbf{D}(\mathbf{v}_h)) + 2\eta(1 - \alpha)(\mathbf{D}(\mathbf{u}_h), \mathbf{D}(\mathbf{v}_h)) - (p_h, \nabla \cdot \mathbf{v}_h) = \langle \mathbf{f}, \mathbf{v}_h \rangle & \forall \mathbf{v}_h \in \mathbb{V}^h \\ (\nabla \cdot \mathbf{u}_h, q_h) = 0 & \forall q_h \in \mathbb{Q}^h \end{array} \right. \quad (3.38)$$

For $0 < \alpha < 1$, the problem 3.38 allows to suppress the second and third conditions, which broadens the spectrum for choosing the finite element approximation for the extra stress tensor $\boldsymbol{\sigma}$. In the present three field Bingham problem, the case of $\alpha = 1$ does not appear (solvent viscosity (η) is always present). Therefore, the inf-sup condition for the stability of velocity-stress $(\mathbf{u}, \boldsymbol{\sigma})$ is not required. Henceforth, the corresponding operator form reads:

$$\begin{bmatrix} \mathcal{A}_1 & \mathcal{B}_2^T & \mathcal{B}_1^T \\ \mathcal{B}_2 & -\mathcal{A}_2 & \mathbf{0} \\ \mathcal{B}_1 & \mathbf{0} & \mathbf{0} \end{bmatrix} \begin{bmatrix} \mathbf{u} \\ \boldsymbol{\sigma} \\ p \end{bmatrix} = \begin{bmatrix} rhs_{\mathbf{u}} \\ rhs_{\boldsymbol{\sigma}} \\ rhs_p \end{bmatrix}. \quad (3.39)$$

Nevertheless, for the convection dominated or the complex Bingham flows (the value of the yield stress τ_s is too large), the convergence of the solving method may be effected. Moreover, when the solvent viscosity vanishes in the non-Newtonian fluids and the choice of the stable finite element is not available, the solver faces difficulties in the convergence. In order to circumvent such situations, solver may need any kind of pre-conditioner/stabilization (e.g. edge-oriented or artificial diffusion stabilization etc.). The numerical studies for such situations are shown in the forthcoming chapters.

3.5 Edge Oriented FEM Stabilization

In the EOFEM, a jump term of the solution gradient over the element edges is added either in the velocity or stress tensor equations. It controls the solution jumps between the edges of the two neighbouring elements. The jump term [60, 61] for the velocity can be defined as:

$$J_u = \sum_{\text{edge } E} \gamma_u h \int_E [\nabla \mathbf{u}] : [\nabla \mathbf{v}] ds \quad (3.40)$$

$$J_u = \sum_{\text{edge } E} \gamma_u h^2 \int_E [\nabla \mathbf{u}] : [\nabla \mathbf{v}] ds \quad (3.41)$$

where γ_u is a constant parameter (chosen according to the numerical oscillations in the problem) and h is the mesh refinement size. The resulting sparsity-pattern of the matrix does not remain the standard one, after the addition of this term. The corresponding operator form reads as follows:

$$\begin{bmatrix} \mathcal{A}_1 + J_u & \mathcal{B}_2^T & \mathcal{B}_1^T \\ \mathcal{B}_2 & -\mathcal{A}_2 & \mathbf{0} \\ \mathcal{B}_1 & \mathbf{0} & \mathbf{0} \end{bmatrix} \begin{bmatrix} \mathbf{u} \\ \boldsymbol{\sigma} \\ p \end{bmatrix} = \begin{bmatrix} \text{rhs}_u \\ \text{rhs}_\sigma \\ \text{rhs}_p \end{bmatrix} \quad (3.42)$$

Similarly, the jump term [62, 63] for the stress tensor can be defined as:

$$J_\sigma = \sum_{\text{edge } E} \gamma_\sigma h \int_E [\nabla \boldsymbol{\sigma}] : [\nabla \phi] ds \quad (3.43)$$

where γ_σ is a constant parameter, the corresponding operator form reads as follows:

$$\begin{bmatrix} \mathcal{A}_1 & \mathcal{B}_2^T & \mathcal{B}_1^T \\ \mathcal{B}_2 & -\mathcal{A}_2 + J_\sigma & \mathbf{0} \\ \mathcal{B}_1 & \mathbf{0} & \mathbf{0} \end{bmatrix} \begin{bmatrix} \mathbf{u} \\ \boldsymbol{\sigma} \\ p \end{bmatrix} = \begin{bmatrix} \text{rhs}_u \\ \text{rhs}_\sigma \\ \text{rhs}_p \end{bmatrix} \quad (3.44)$$

3.6 Artificial Diffusion Stabilization

While solving the highly non-linear system of equations, the numerical oscillations might appear in the solution effecting its convergence behaviour. In order to suppress these oscillations, the artificial diffusion can be used as a stabilization. In the present work, the system of equations (2.13) is also non-linear. Therefore, some amount of artificial diffusion is added to the constitutive equation of the stress tensor $\boldsymbol{\sigma}$ in the form of a linear operator $L_\sigma = \gamma h^2 \Delta \boldsymbol{\sigma}$. This stabilization is controlled by a parameter γh^2 , which decreases with mesh refinement.

CHAPTER 3. FINITE ELEMENT METHOD

The non-linearity of the system of equations (2.13) increases, when the regularization parameter ϵ gets very small. To overcome this problem, we add a small amount of stabilization in order to increase the stability of the numerical solver but the accuracy of the solution is a little bit compromised. The corresponding operator form reads as follows:

$$\begin{bmatrix} \mathcal{A}_1 & \mathcal{B}_2^T & \mathcal{B}_1^T \\ \mathcal{B}_2 & -\mathcal{A}_2 + L_\sigma & \mathbf{0} \\ \mathcal{B}_1 & \mathbf{0} & \mathbf{0} \end{bmatrix} \begin{bmatrix} \mathbf{u} \\ \boldsymbol{\sigma} \\ p \end{bmatrix} = \begin{bmatrix} \text{rhs}_u \\ \text{rhs}_\sigma \\ \text{rhs}_p \end{bmatrix} \quad (3.45)$$

The effect of the stabilization can be observed in the detailed numerical studies carried out in the next chapters.

Chapter 4

Nonlinear and Linear Solvers

4.1 Nonlinear Solver

This chapter provides a brief description of the numerical solvers, that have been used for solving the nonlinear system of equations (3.39). The nonlinearity of this system arises due to the presence of the nonlinear viscosity term in the constitutive equation of the new auxiliary stress tensor. Solving such a system is a big challenge for any nonlinear numerical solver. Usually, the Newton or fixed point iteration methods [64] are used to solve the nonlinear problems in fluid dynamics. Since the Newton method usually has a faster convergence rate than the fixed point method, therefore, it is preferred in most of the cases.

4.1.1 Newton Method

This section explains the linearization process of the Newton method. For a function $\mathcal{R}(\mathcal{U}) \in C^1$ and its non-zero first derivative $\mathcal{R}'(\mathcal{U})$, where $\mathcal{U} = (\mathbf{u}, \boldsymbol{\sigma}, p)$ is the solution vector and \mathcal{R} is the residual of the current nonlinear system (3.39). The Newton iteration reads as:

$$\mathcal{U}^{n+1} = \mathcal{U}^n - \mathcal{R}'(\mathcal{U}^n)^{-1} \mathcal{R}(\mathcal{U}^n) \quad \text{for all } n \geq 0 \quad (4.1)$$

The basic purpose of this method is to find the root of the equation (4.1), where the derivative of the function should be non-zero. Moreover, the initial guess \mathcal{U}^0 must be provided at $n = 0$ to solve the following step:

$$J(\mathcal{U}^n) \delta \mathcal{U}^n = \mathcal{R}(\mathcal{U}^n)$$

CHAPTER 4. NONLINEAR AND LINEAR SOLVERS

where $J(\mathcal{U}^n) = \frac{\partial \mathcal{R}(\mathcal{U}^n)}{\partial \mathcal{U}^n}$ is the Jacobian matrix. The advantageous quadratic convergence of the Newton method is proved according to the following theorem.

Theorem 2 *Let \mathbf{x} be a solution of $F(\mathbf{x}) = 0$ and the Jacobian $J(\mathbf{x}^n) = \frac{\partial F(\mathbf{x}^n)}{\partial \mathbf{x}^n}$ is invertible and locally Lipschitz continuous. Then, if \mathbf{x}^0 is sufficiently close to \mathbf{x} , the Newton algorithm has the following property [65]*

$$\|\mathbf{x}^{n+1} - \mathbf{x}\| \leq c \|\mathbf{x}^n - \mathbf{x}\|^2.$$

Newton method is very sensitive regarding the initial guess of the solution and depends strongly on the properties of the Jacobian matrices during the iterations. It is very important to have initial guess close to the solution for achieving the quadratic convergence. In the present work, the Newton method solves the nonlinear steady system of equations (2.13) with the following steps:

Algorithm 1 Newton method solver

- Provide the input parameters, e.g. tolerance, parameters of the non linear solver, initial guess and the iteration number n
 - Repeat until the tolerance is achieved
 - Calculate the residual $\mathcal{R}(\mathcal{U}^n) = A \mathcal{U}^n - b$
 - Build the Jacobian $J(\mathcal{U}^n) = \frac{\partial \mathcal{R}(\mathcal{U}^n)}{\partial \mathcal{U}^n}$
 - Solve $J(\mathcal{U}^n) \delta \mathcal{U}^n = \mathcal{R}(\mathcal{U}^n)$
 - Find the optimal value of the damping factor $\omega^n \in (-1, 0]$
 - Approximate $\mathcal{U}^{n+1} = \mathcal{U}^n - \omega^n \delta \mathcal{U}^n$
-

There are also some other factors in the Newton method which should be taken into account for the numerical stability, e.g. a damping factor ω (when the solution is non-smooth). In our work, this factor is calculated by a root finding technique called the line search method [66, 67]. This method calculates the damping parameter ω automatically by adaptively changing the length of the correction vector. The $\omega^n \in (-1, 0]$ is calculated such that:

$$J(\mathcal{U}^{n+1}) \cdot \mathcal{U}^{n+1} \leq J(\mathcal{U}^n) \cdot \mathcal{U}^n$$

The residual is calculated by the following equation:

$$\mathcal{R}(\omega) = \mathcal{U}^n - \omega^n \delta \mathcal{U}^n$$

If \mathcal{U}^n is far from the final solution, then the damping strategy helps to minimize the residual $\mathcal{R}(\omega)$ by back tracking into the Newton direction i.e. $\delta \mathcal{U}^n$ [62]. To

4.2. LINEAR SOLVER

find the new value of ω , the method first tests the value $\omega = -1$ (called full step). Afterwards, the new damping factor can be calculated using the following quadratic equation:

$$\omega^{\text{new}} = \frac{-\|\mathcal{R}'(0)\|}{2(\|\mathcal{R}(1)\| - \|\mathcal{R}(0)\| - \|\mathcal{R}'(0)\|)} \quad (4.2)$$

where $\omega^0, \mathcal{R}(0)$ and $\mathcal{R}'(0)$ are the known factors (calculated from step 3 and 4 in the algorithm 1). Once the ω^{new} is calculated, the old value $\mathcal{R}(\omega = -1)$ is replaced with the new one and the process continues till $\mathcal{R}(\omega)$ is minimized. For the current nonlinear Bingham problem, one Newton iteration reads:

$$\begin{bmatrix} \mathbf{u}^{n+1} \\ \boldsymbol{\sigma}^{n+1} \\ p^{n+1} \end{bmatrix} = \begin{bmatrix} \mathbf{u}^n \\ \boldsymbol{\sigma}^n \\ p^n \end{bmatrix} - \omega_n \begin{bmatrix} \frac{\partial \mathcal{R}_{\mathbf{u}}(\mathcal{U}^n)}{\partial \mathbf{u}} & \frac{\partial \mathcal{R}_{\mathbf{u}}(\mathcal{U}^n)}{\partial \boldsymbol{\sigma}} & \frac{\partial \mathcal{R}_{\mathbf{u}}(\mathcal{U}^n)}{\partial p} \\ \frac{\partial \mathcal{R}_{\boldsymbol{\sigma}}(\mathcal{U}^n)}{\partial \mathbf{u}} & \frac{\partial \mathcal{R}_{\boldsymbol{\sigma}}(\mathcal{U}^n)}{\partial \boldsymbol{\sigma}} & \frac{\partial \mathcal{R}_{\boldsymbol{\sigma}}(\mathcal{U}^n)}{\partial p} \\ \frac{\partial \mathcal{R}_p(\mathcal{U}^n)}{\partial \mathbf{u}} & \frac{\partial \mathcal{R}_p(\mathcal{U}^n)}{\partial \boldsymbol{\sigma}} & \frac{\partial \mathcal{R}_p(\mathcal{U}^n)}{\partial p} \end{bmatrix}^{-1} \begin{bmatrix} \mathcal{R}_{\mathbf{u}}(\mathcal{U}^n) \\ \mathcal{R}_{\boldsymbol{\sigma}}(\mathcal{U}^n) \\ \mathcal{R}_p(\mathcal{U}^n) \end{bmatrix} \quad (4.3)$$

In the Newton method, first derivative of the residuals are needed in every nonlinear iteration called Jacobian matrix. The Jacobian is either calculated analytically or approximated by the divided difference method. The advantage of the approximation of the Jacobian is that this method acts in a black box manner so that it allows any nonlinear equations to be handled automatically without having to derive the corresponding calculations [62, 68]. In this work, the Jacobian matrix is not computed exactly, instead its approximation is computed using divided differences and the corresponding j -th column is given as follows

$$\left[\frac{\partial \mathcal{R}(\mathcal{U}^n)}{\partial \mathcal{U}^n} \right]_j \approx \frac{\mathcal{R}(\mathcal{U}^n + \chi \delta_j) - \mathcal{R}(\mathcal{U}^n - \chi \delta_j)}{2\chi} \quad (4.4)$$

where δ_j is the vector with unit j -th component and zero otherwise. The advantage of this approximation is that we don't need any knowledge of the Jacobian a priori. However, in this method, the step-size χ is a "free" parameter and the right choice might be a delicate task. The parameter χ can be fixed or can be modified according to some norm of the solution $\|\mathcal{U}^n\|$ or the norm of the update in the previous step, i.e. $\|\delta \mathcal{U}^{n-1}\|$. Theoretically [69], for double machine precision the value of the $\chi^{\frac{1}{3}} = 10^{-6}$ is suggested but practically, the step size is chosen to be $\chi^{\frac{1}{2}} = 10^{-8}$.

4.2 Linear Solver

After the linearization of the problem with Newton method, the next significant task is to solve the linear sub-problem. Usually, the linear solvers are divided

CHAPTER 4. NONLINEAR AND LINEAR SOLVERS

into two categories, direct and iterative solvers. The choice of using one of these types, depends on the size of the problem matrix. The computations of the linear solver are expensive w.r.t. time. Therefore, considering that the computational machine has sufficiently high memory, the direct solver may be a good choice. There are several direct solvers in the literature e.g. Gauss elimination or LU decomposition [70, 71]. In these solvers, if the matrix A and right hand side is provided, the method solves the problem in one step and gives the solution of unknown vector \mathcal{U} containing all the unknown fields $\{\mathbf{u}, \boldsymbol{\sigma}, p\}$. The unsymmetric multifrontal package (UMFPACK) [72] is one of the ready to use available routines. Moreover, if the computing machines do not have enough memory, then the iterative methods can be a good choice, ILU decomposition, conjugate gradient method, bi-conjugate gradients and variants (BICG, BICGSTAB [73], GMRES [74]) or multigrid [75] are examples of the iterative methods.

4.2.1 Multigrid Method

Multigrid [75, 76, 77] is one of the fastest numerical solver for the linear systems, consisting of different components named as smoother, restriction, prolongation and a direct coarse mesh solver (UMFPACK). These components contribute their part in solving the linear sub-problem. Multigrid works with grid refinement levels from higher to lower. Restriction is performed to convert the solution from finer mesh to coarser and prolongation from coarse to finer mesh levels. Moreover, pre and post smoothing steps are applied before and after restriction/prolongation. The applied smoother is of Vanka-type [78, 53] with the local pressure-schur complement approach:

$$\begin{bmatrix} \mathbf{u}^{n+1} \\ \boldsymbol{\sigma}^{n+1} \\ p^{n+1} \end{bmatrix} = \begin{bmatrix} \mathbf{u}^n \\ \boldsymbol{\sigma}^n \\ p^n \end{bmatrix} + \omega_n \sum_{K \subset \mathcal{T}_h} [J]_{|K}^{-1} \begin{bmatrix} \mathcal{R}_u(\mathcal{U}^n) \\ \mathcal{R}_\sigma(\mathcal{U}^n) \\ \mathcal{R}_p(\mathcal{U}^n) \end{bmatrix}_{|K} \quad (4.5)$$

where $|K$ represents that the corresponding terms are calculated on each element and then the summation is carried out to assemble all elements. The algorithm of one multigrid cycle is given below named as algorithm 2. The frequency of visiting the coarser mesh level depends on the cycle types e.g. V-cycle, F-cycle or W-cycle. The coarsest level is visited once in V-cycle and more than one time in F-cycle. The grid of the coarsest level needs memory storage because it is solved by the direct solver. Therefore, it should be coarse enough in order to avoid any memory issue.

4.3. FLOW AROUND CYLINDER BENCHMARK

Algorithm 2 One cycle multigrid

- Provide the input parameter, i.e. linear tolerance
 - Set the coarse and maximum grid of level L
 - Pre-smoothing: smooth e^L
 - Restriction: restrict A , \mathcal{R}
 - **if** $(L - 1)$ is min level **then**
 Solve $Ae = \mathcal{R}$
 Prolong the error e
 else
 Pre-smoothing: smooth $e^{(L-1)}$
 end if
-

In the next sections, solvability of the Newton-multigrid solver has been tested for some simple benchmark problems for the Newtonian fluid flows i.e. laminar flow around cylinder and lid driven cavity.

4.3 Flow Around Cylinder Benchmark

This DFG 2-dimensional benchmark [79] analyse the attributes of the flow around an obstacle in a rectangular channel, where a cylinder of radius $r = 0.05$ is placed with the centre at $(0.2, 0.2)$ in a rectangular channel of length 2.2, the upper and lower walls are 0.41 length apart. The geometrical configuration and coarse mesh are shown in Fig. 4.1 and 4.2. The fluid density (ρ) and kinematic viscosity (η) are set to 1 and 0.001, respectively. The fluid is characterised by the incompressible stationary three-field Navier-Stokes equations as follows:

$$\left\{ \begin{array}{ll} \sigma - 2\eta\mathbf{D}(\mathbf{u}) = 0 & \text{in } \Omega \\ \mathbf{u} \cdot \nabla\mathbf{u} - \nabla \cdot \left(2\eta(1 - \alpha)\mathbf{D}(\mathbf{u}) + \alpha\sigma \right) + \nabla p = 0 & \text{in } \Omega \\ \nabla \cdot \mathbf{u} = 0 & \text{in } \Omega \\ \mathbf{u} = \mathbf{g}_D & \text{on } \Gamma_D \end{array} \right. \quad (4.6)$$

CHAPTER 4. NONLINEAR AND LINEAR SOLVERS

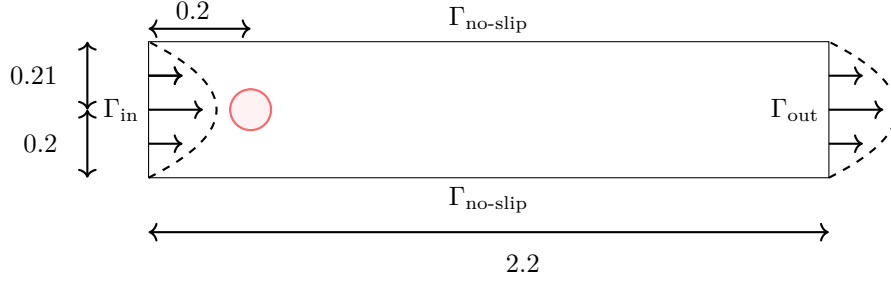


Figure 4.1: Flow around cylinder configuration.

Here, α is a constant parameter with the range $0 \leq \alpha \leq 1$. Dirichlet boundary is defined at the inlet Γ_{in} with a parabolic profile

$$u_x(y) = \left(\frac{4.0Uy(0.41 - y)}{(0.41)^2}, 0 \right),$$

having maximum velocity $U_{\text{max}} = 0.3$. The corresponding mean velocity is $\mathcal{U}_{\text{mean}} = 0.2$, where $\mathcal{U}_{\text{mean}}$ is defined as:

$$\mathcal{U}_{\text{mean}} = \frac{2}{3}U_{\text{max}}.$$

No slip boundary condition is defined at the upper and lower walls and do-nothing boundary condition is defined at the outlet Γ_{out} . The characteristic length of the cylinder ($L = 2r_c = 0.1$) along with the viscosity (η) and mean velocity yields the Reynolds number $Re = 20$, depicting a laminar flow. Here r_c is the radius of the cylinder:

$$Re = \frac{\mathcal{U}_{\text{mean}}L}{\eta}. \quad (4.7)$$

Force acting on cylinder surface has two components i.e. lift and drag, respectively. Lift is perpendicular to the direction of flow, whereas drag is parallel to the direction of the flow. The mathematical expressions for lift and drag are defined as:

$$\mathcal{F}_L = - \int_S \left(\eta \frac{\partial \mathbf{u}_\tau}{\partial n} n_1 - pn_2 \right) ds, \quad \mathcal{F}_D = \int_S \left(\eta \frac{\partial \mathbf{u}_\tau}{\partial n} n_2 - pn_1 \right) ds. \quad (4.8)$$

The dimensionless drag and lift coefficients are also calculated with following definitions:

$$C_D = \frac{2}{U_{\text{mean}}^2 L} \mathcal{F}_D, \quad C_L = \frac{2}{U_{\text{mean}}^2 L} \mathcal{F}_L.$$

For testing the robustness and efficiency of the resulting discretization in comparison with the Stokes solver both in two-field as well as in three-field formulation, we substitute $\alpha = 0$, for reducing this system of equations into two-field

4.3. FLOW AROUND CYLINDER BENCHMARK

formulation. The numerical results illustrating the performance of system (4.6) for flow around cylinder benchmark are presented in Table [4.1]. Numerical results in the form of lift/drag are compared and validated with the results of Damanik et al. [62]. Convergence of the solution is presented for higher order finite elements (Q_2/P_1^{disc}). Where "NL" denotes nonlinear iterations, "LL" denotes the average number of multigrid iterations. Each refinement level shows a strong agreement between both studies. The accuracy of the solution in terms of velocity magnitude, pressure and stream functions are presented in Fig. 4.3. However, the basic purpose of this numerical study is to show the suppression of the inf-sup condition on velocity-stress $(\mathbf{u}, \boldsymbol{\sigma})$ for the range of α between 0 and 1. Therefore, a detailed study [80] is carried out in Table [4.2] to show the stability of the three-field system, unless $\alpha = 1$. One can see the accuracy of the solution as well as the robustness of the monolithic Newton-multigrid solver in the above mentioned tables. Moreover, these results obtained from higher order finite elements show mesh convergence with respect to the mesh refinements. For the extreme case, when the solvent viscosity is absent i.e. $\alpha = 1$, the solver is not able to converge at all because the finite element pair for velocity-stress $(\mathbf{u}, \boldsymbol{\sigma})$ is not stable. In order to circumvent this stability issue, edge-oriented stabilization is added and clearly the solver is able to achieve accurate results as well as the behaviour of convergence is quite good with the decent number of iterations. The eofem stabilization can also be added to eliminate the numerical oscillations of the solver. Moreover, it is beneficial to add eofem, when the yield stress value is very large in the three-field Bingham formulation.

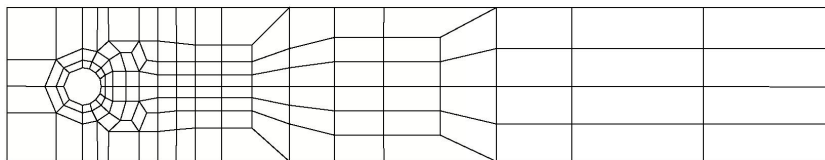


Figure 4.2: Flow around cylinder coarse mesh.

Table 4.1: **Flow around cylinder Drag/Lift:** Comparison with Damanik et al.[62], where NL denotes the number of Newton iterations, LL denotes the average number of multigrid iterations.

L	Drag/Lift	NL/LL	Drag/Lift [62]	NL/LL [62]
1	5.5550/0.009498	9/1	5.5550/0.009498	9/2
2	5.5722/0.010601	9/1	5.5722/0.010601	9/2
3	5.5776/0.010616	9/1	5.5776/0.010616	9/1
4	5.5791/0.010618	8/1	5.5790/0.010618	8/1

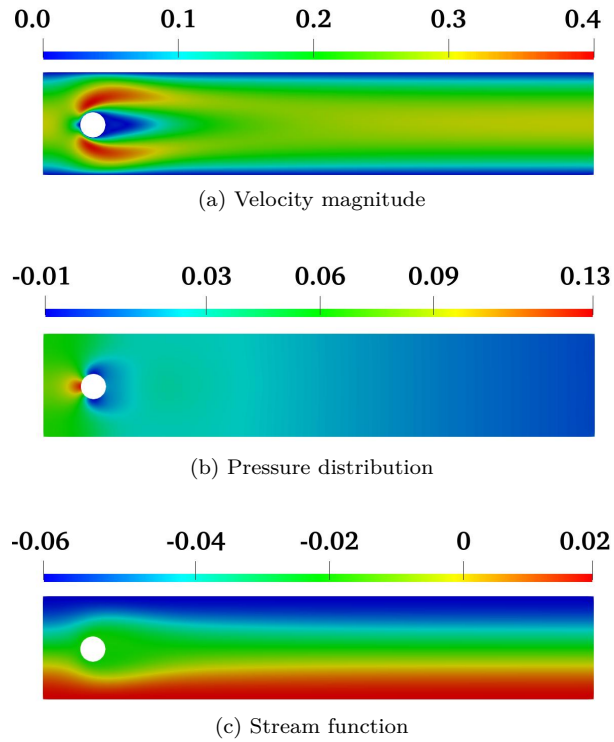


Figure 4.3: Flow around cylinder: Visualization of the velocity, pressure and stream function.

4.3. FLOW AROUND CYLINDER BENCHMARK

Table 4.2: **Flow around cylinder:** Values of lift and drag coefficient [80] for flow around cylinder benchmark at different refinement levels for $0 \leq \alpha \leq 1$ in the system (4.6) along with the solver performance in terms of "NL/LL".

α	L	With EOFEM			
		Lift/Drag	NL/LL	Lift/Drag	NL/LL
0	1	0.008786117/5.5285	7/4	0.010107982/5.5427	7/3
0	2	0.010424275/5.5663	7/4	0.010702943/5.5674	7/3
0	3	0.010597517/5.5764	7/3	0.010619474/5.5757	7/3
0	4	0.010615911/5.5788	7/4	0.010616941/5.5782	7/3
0	5	0.010618494/5.5794	7/4	0.010618268/5.5790	6/4
0.25	1	0.009307183/5.5454	7/3	0.010013472/5.5301	7/3
0.25	2	0.010559395/5.5701	7/2	0.010677420/5.5639	7/2
0.25	3	0.010611104/5.5772	7/2	0.010615166/5.5744	7/3
0.25	4	0.010617270/5.5790	7/2	0.010615982/5.5777	7/3
0.25	5	0.010618658/5.5794	6/3	0.010617947/5.5788	6/4
0.5	1	0.009075847/5.5363	7/3	0.009911587/5.5171	7/3
0.5	2	0.010506223/5.5681	7/3	0.010650185/5.5601	7/2
0.5	3	0.010605621/5.5767	7/3	0.010610603/5.5730	7/3
0.5	4	0.010616682/5.5789	7/3	0.010614926/5.5771	7/3
0.5	5	0.010618582/5.5794	7/3	0.010617576/5.5785	7/4
0.75	1	0.008786117/5.5285	7/4	0.009800026/5.5039	7/3
0.75	2	0.010424275/5.5663	7/4	0.010620649/5.5562	7/3
0.75	3	0.010597517/5.5764	7/3	0.010605686/5.5715	7/3
0.75	4	0.010615911/5.5788	7/4	0.010613740/5.5764	7/3
0.75	5	0.010618494/5.5794	7/4	0.010617138/5.5782	7/4
1	1	-	-	0.009675569/5.4903	7/3
1	2	-	-	0.010587841/5.5520	7/3
1	3	-	-	0.010600252/5.5698	7/3
1	4	-	-	0.010612372/5.5756	7/3
1	5	-	-	0.010616606/5.5778	7/4

4.4 Lid Driven Cavity Benchmark

The numerical simulation of Newtonian fluid flow in the lid-driven square cavity is a well-known as well as a very simple benchmark because of its wide application in the industry e.g. where a shear is applied on the upper wall of the square container. The geometrical configuration consists of a unit square domain $\bar{\Omega} = [0, 1]^2$, where the Dirichlet boundary conditions are imposed for $u|_{y=1} = (1, 0)^T$ and $u = 0$ everywhere else. Two different Reynolds numbers are tested i.e. $Re = 1000$ and $Re = 5000$, which corresponds to the constant viscosity $\eta = 1e - 3$ and $\eta = 2e - 4$, respectively. For simulating the Newtonian fluids, the yield stress value is set to zero i.e. $\tau_s = 0$ in the system of equations (2.13). The numerical results shown in the Table [4.3] presents a validation of this benchmark with the Damanik et al. [62], where the Kinetic energy E is calculated and compared at different refinement levels as:

$$E = \frac{1}{2} \|\mathbf{u}\|_0^2.$$

The results calculated using $Q_2P_1^{\text{disc}}$ elements, converged and are mesh independent Table [4.3]. Fig. 4.4 represents the stream contours (top) and the velocity magnitude (bottom) at the cut line passing through the centre of the square domain for the mesh refinement level 8. It can be clearly observed that the results are in good agreement with the results of Damanik et al. [62].

Table 4.3: **Lid driven cavity:** Comparison of the kinetic energy values with Damanik et al. [62] for Newtonian fluid flow at $Re = 1000$ and $Re = 5000$ for different mesh refinement levels.

L	$Re = 1000$		$Re = 5000$	
	K.E.	K.E. [62]	K.E.	K.E. [62]
4	$5.245101e - 02$	$5.2454e - 02$	$8.486944e - 02$	$1.0860e - 01$
5	$4.541506e - 02$	$4.5418e - 02$	$6.082526e - 02$	$6.1149e - 02$
6	$4.458871e - 02$	$4.4590e - 02$	$4.955858e - 02$	$4.9571e - 02$
7	$4.452357e - 02$	$4.4524e - 02$	$4.768668e - 02$	$4.7691e - 02$
8	$4.451904e - 02$	$4.4519e - 02$	$4.744816e - 02$	$4.7465e - 02$

4.4. LID DRIVEN CAVITY BENCHMARK

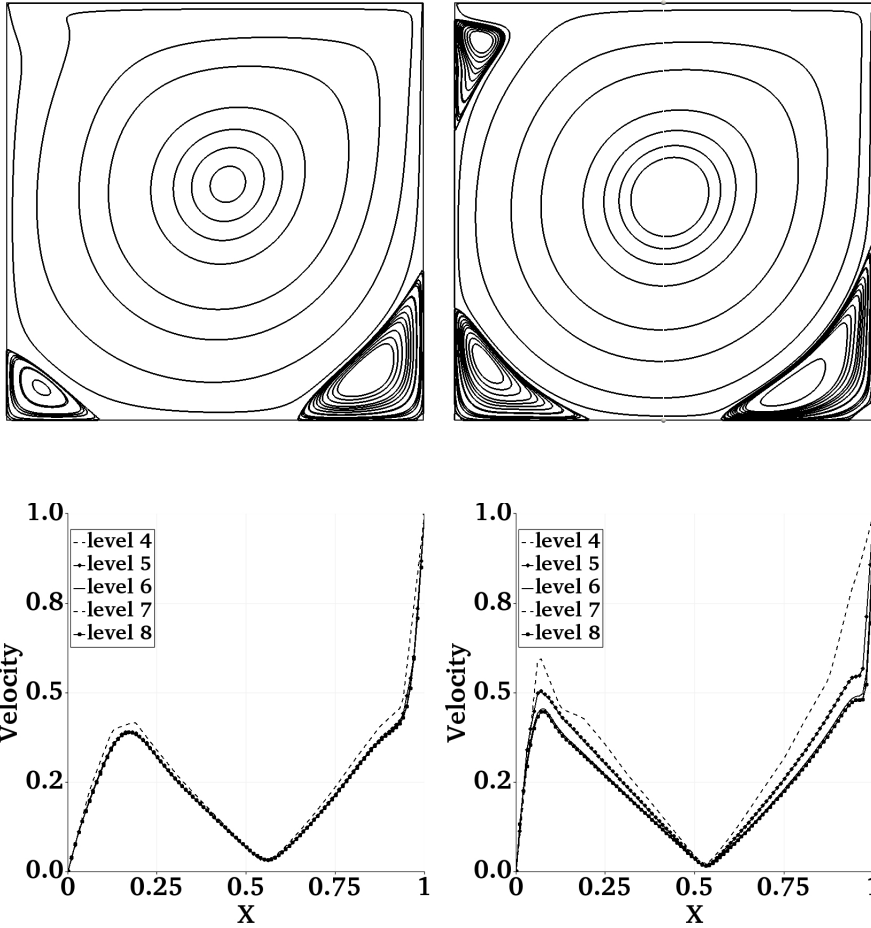


Figure 4.4: **Lid driven cavity:** stream line contours (top) and velocity magnitude (bottom) at the cutline $x = 0.5$ for Newtonian fluid flow at $Re = 1000$ (left) and $Re = 5000$ (right).

CHAPTER 4. NONLINEAR AND LINEAR SOLVERS

Chapter 5

Numerical Study of Bingham

In this chapter, the numerical studies for different prototypical configurations of Bingham viscoplastic fluid are carried out to test the solvability of the problem. Three-field formulation with a constitutive equation of an auxiliary stress tensor $\boldsymbol{\sigma}$ with Bercovier-Engelmann viscosity regularization model is solved with the discrete Newton solver, the resulting linear problem is then solved with the multigrid solver. Moreover, higher order finite elements Q_2 are used to discretize the velocity, stress and P_1^{disc} for pressure field. This discrete nonlinear system is solved in a coupled manner/monolithically. The results of different benchmarks show the accuracy and efficiency of the solver in the prediction of unyielded or dead zones in the Bingham fluid regimes, which is very important for achieving the 'true' viscoplastic solution.

5.1 Bingham Fluid Flow in a Channel

The two dimensional channel is considered as a domain consisting of two parallel plates with h length apart and long, shown in Fig. 5.1. Two different types of boundary conditions have been imposed on this configuration in subsection 5.1.1 and 5.1.2, respectively.

As already discussed in chapter[2], that the three-field formulation has a potential to solve the Bingham fluid accurately as the regularization parameter can be reduced to zero (" $\epsilon \rightarrow 0$ "), reads as follows:

$$\boldsymbol{\sigma} = \frac{\mathbf{D}(\mathbf{u})}{\|\mathbf{D}(\mathbf{u})\|_\epsilon} \quad (5.1)$$

$$\begin{cases} \|\mathbf{D}(\mathbf{u})\|_\epsilon \boldsymbol{\sigma} - \mathbf{D}(\mathbf{u}) = 0 & \text{in } \Omega \\ -\nabla \cdot (2\eta \mathbf{D}(\mathbf{u}) + \sqrt{2}\tau_s \boldsymbol{\sigma}) + \nabla p = 0 & \text{in } \Omega \\ \nabla \cdot \mathbf{u} = 0 & \text{in } \Omega \\ \mathbf{u} = \mathbf{g}_D & \text{on } \Gamma_D \end{cases} \quad (5.2)$$

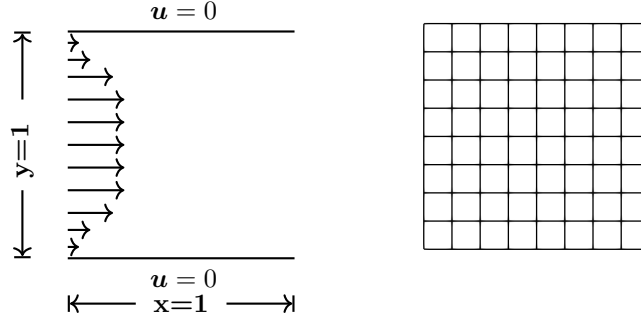


Figure 5.1: Flow in a unit square channel (left) with the coarse mesh (right).

5.1.1 Boundary Conditions: Case 1

The problem is solved under the assumption of Dirichlet boundary conditions on the domain $\bar{\Omega} = [0, h]^2$ boundaries and the analytical velocity profile is given for the x-component as:

$$u_1 = \begin{cases} \frac{1}{8} [(h - 2\tau_s)^2 - (h - 2\tau_s - 2y)^2] & 0 \leq y < \frac{h}{2} - \tau_s \\ \frac{1}{8}(h - 2\tau_s)^2 & \frac{h}{2} - \tau_s \leq y \leq \frac{h}{2} + \tau_s \\ \frac{1}{8} [(h - 2\tau_s)^2 - (2y - 2\tau_s - h)^2] & \frac{h}{2} + \tau_s < y \leq h \end{cases} \quad (5.3)$$

with $u_2 = 0$ and $p = -x + c$ [81]. The viscosity of the fluid is set to be $\eta = 1$, the body force is $\mathbf{f} = 0$ and $h = 1$ is considered. The central part of the channel flow is the rigid/plug zone of constant velocity, i.e.

$$\frac{h}{2} - \tau_s \leq y \leq \frac{h}{2} + \tau_s. \quad (5.4)$$

A comparison study is carried out for the two-field (\mathbf{u}, p) and the three-field $(\mathbf{u}, \boldsymbol{\sigma}, p)$ formulation in the Table [5.1], consisting of Newton iterations "NL" and L^2 norm of the velocity error $\|\mathbf{u} - \mathbf{u}_{\text{ex}}\|$. In this table, the mesh refinement level 3 ($h=1/8$) is the coarse mesh level and no initial solution is given to this refinement level. It can be clearly seen, that the two-field formulation could only solve up to $\epsilon = 10^{-2}$, which concludes that this formulation can only solve

5.1. BINGHAM FLUID FLOW IN A CHANNEL

Bingham for non-vanishing regularization parameter. On the other hand, the three-field formulation can not only solve very small ϵ but also $\epsilon = 0$ accurately, quantitatively shown by $\|\mathbf{u} - \mathbf{u}_{\text{ex}}\|$ in the Table [5.1]. Hence, the goal to solve the regularization-free Bingham numerically is achieved with quite accurate results, which assures the true viscoplastic solution.

Fig 5.2 presents the velocity magnitude for different ϵ at the refinement level 5 ($h=1/32$), where different flow regimes (shear and plug zones) are developed depending on the yield stress value. When the applied stress is greater than the threshold value τ_s (0.25 in the current test), the flow develops a parabolic profile due to the shear region, whereas the middle region of the channel contains the plug zone, where the $\|\mathbf{D}(\mathbf{u})\| = 0$ and the fluid moves with the constant velocity ($\mathbf{u} = c$). Moreover, the value of the regularization parameter has a great influence on the velocity profile inside the channel domain, when the ϵ is large (10^{-1}), the interface of the plug zone is not accurately captured. On the other hand, when the value of the regularization parameter is smaller or vanishes (i.e. $\epsilon = 0$), the interface and the unyielded zones can be predicted more accurately, which can be described quantitatively in the form of $\|\mathbf{u} - \mathbf{u}_{\text{ex}}\|$ in the Table [5.1]. The unyielded/dead zones can be expressed with the $\|\mathbf{D}(\mathbf{u})\|$ and its contours, shown in Fig. 5.3 and 5.4, respectively. The blue region in Fig. 5.3 corresponds to nearly zero value of the deformation tensor $\|\mathbf{D}(\mathbf{u})\| \approx 0$, it also has a great impact of regularization parameter's value. In this figure, the blue region is almost absent in the case of $\epsilon = 10^{-1}$, which implies the compromised accuracy of the solution in the rigid zone. The pressure distribution inside the rigid zone of the fluid is not linear, Fig. 5.5 illustrates that the pressure is linear in the Newtonian zone of the fluid (which is according to the expected solution) but some singularities/perturbations occur near the boundaries and in the plug zone. Moreover, the magnitude of the new auxiliary stress tensor ($\|\boldsymbol{\sigma}\|$) in Fig. 5.6 demonstrates the effect of the regularization parameter, where all the cases including $\epsilon = 0$ shows that the $\|\boldsymbol{\sigma}\| < 1$ in the rigid zone, as expected in this channel flow.

CHAPTER 5. NUMERICAL STUDY OF BINGHAM

Table 5.1: **Bingham flow in a channel:** A comparison of the two-field (regularized viscosity approach) (\mathbf{u}, p) and three-field $(\mathbf{u}, \boldsymbol{\sigma}, p)$ formulations in terms of Newton iterations "NL" and $\|\mathbf{u} - \mathbf{u}_{\text{ex}}\|$ for different mesh refinement levels L and regularization parameter ϵ , with the yield stress value $\tau_s = 0.25$.

ϵ	L	Two-Field		Three-Field	
		NL	$\ \mathbf{u} - \mathbf{u}_{\text{ex}}\ $	NL	$\ \mathbf{u} - \mathbf{u}_{\text{ex}}\ $
10^{-1}	3	3	3.346×10^{-3}	6	2.598×10^{-3}
	4	3	2.790×10^{-3}	3	2.597×10^{-3}
	5	2	2.563×10^{-3}	2	2.597×10^{-3}
10^{-2}	3	9	1.760×10^{-3}	45	5.873×10^{-4}
	4	6	1.041×10^{-4}	4	5.818×10^{-4}
	5	3	6.771×10^{-4}	3	5.818×10^{-4}
10^{-3}	3	-	-	14	6.257×10^{-5}
	4	-	-	6	6.415×10^{-5}
	5	-	-	4	6.416×10^{-5}
10^{-4}	3	-	-	49	6.407×10^{-6}
	4	-	-	5	6.262×10^{-6}
	5	-	-	4	6.298×10^{-6}
10^{-5}	3	-	-	39	6.788×10^{-7}
	4	-	-	13	6.378×10^{-7}
	5	-	-	5	6.297×10^{-7}
0	3	-	-	18	2×10^{-11}
	4	-	-	4	7×10^{-12}
	5	-	-	3	4×10^{-12}

5.1. BINGHAM FLUID FLOW IN A CHANNEL

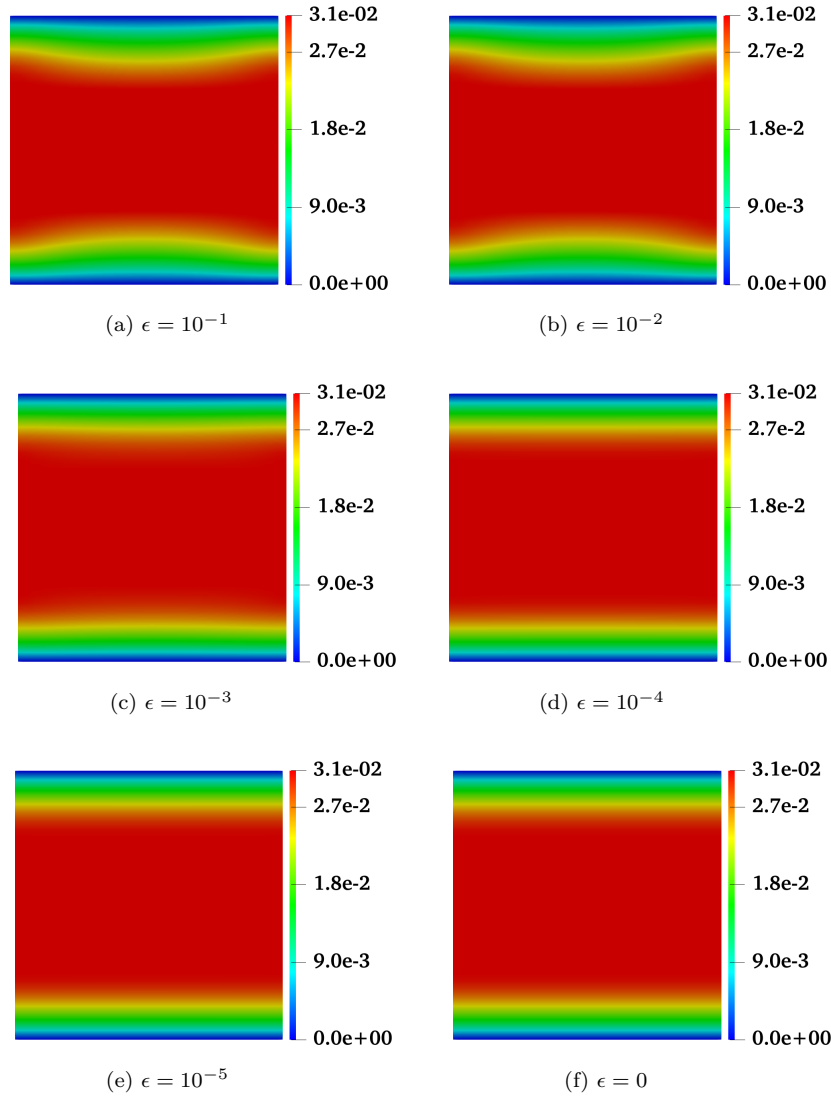


Figure 5.2: **Bingham flow in a channel:** The velocity magnitude $\|\mathbf{u}\|$ at mesh refinement level 5 ($h = 1/32$) for $\epsilon = 10^{-1}, 10^{-2}, 10^{-3}, 10^{-4}, 10^{-5}$ and 0 by using system of equations 5.2 with $\tau_s = 0.25$.

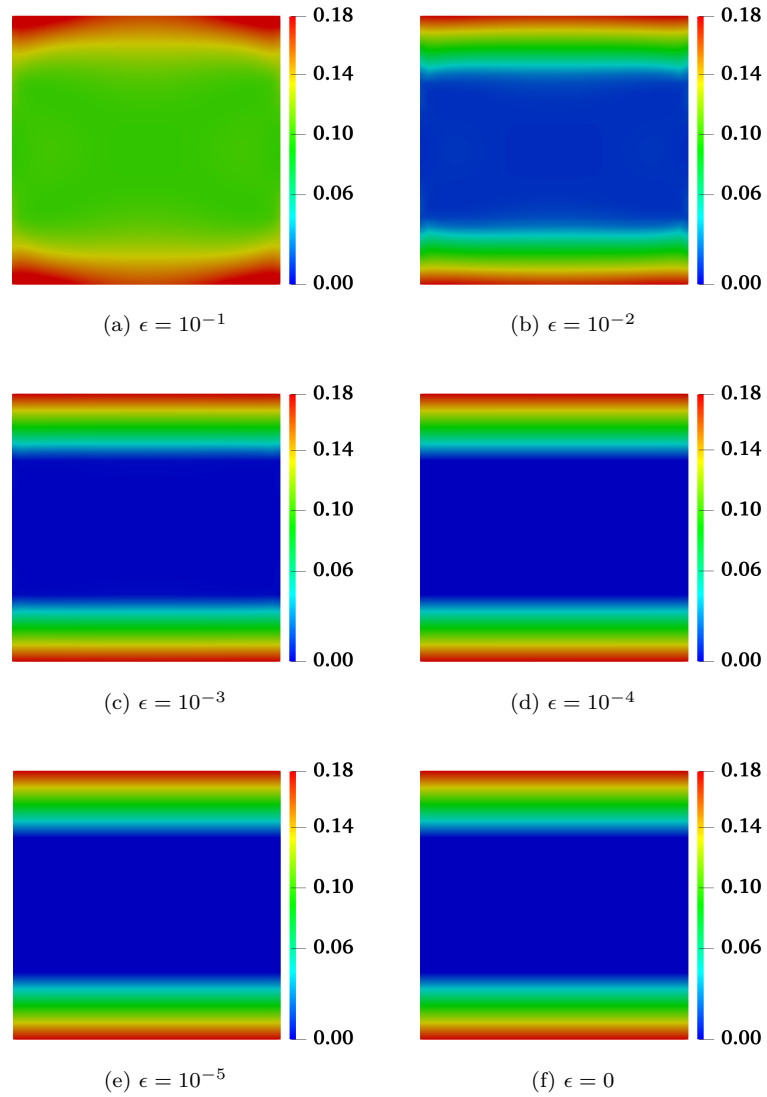


Figure 5.3: **Bingham flow in a channel:** The norm of deformation tensor $\|\mathbf{D}(\mathbf{u})\|$ at mesh refinement level 5 ($h = 1/32$) for $\epsilon = 10^{-1}, 10^{-2}, 10^{-3}, 10^{-4}, 10^{-5}$ and 0 by using system of equations 5.2 with $\tau_s = 0.25$.

5.1. BINGHAM FLUID FLOW IN A CHANNEL

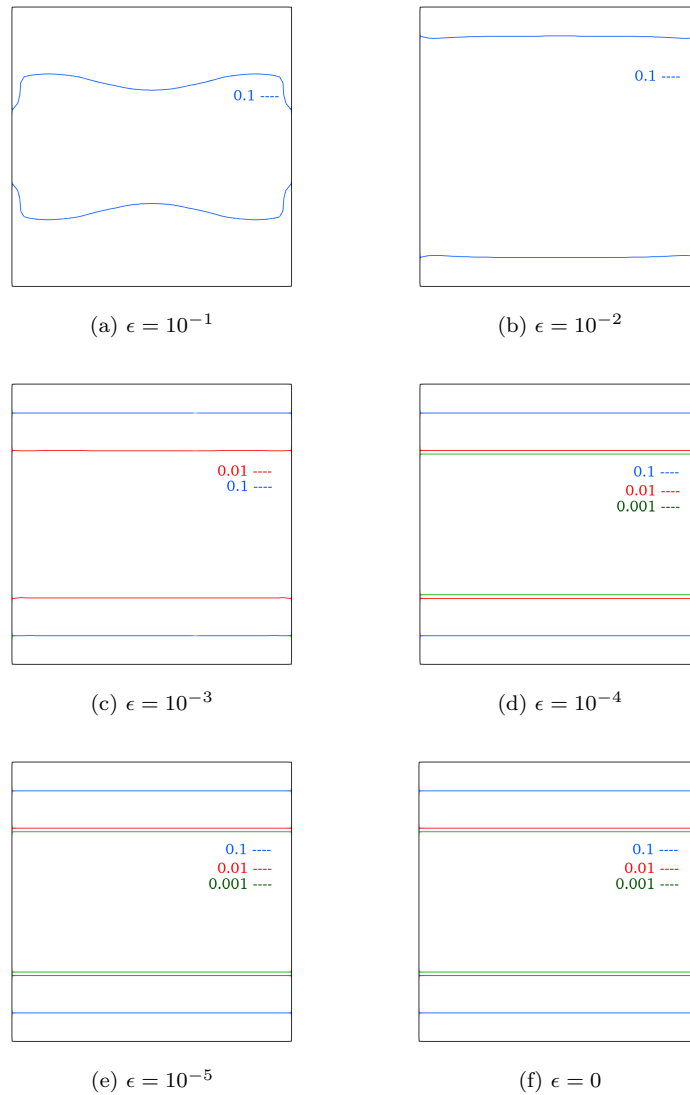
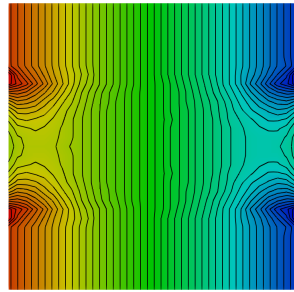
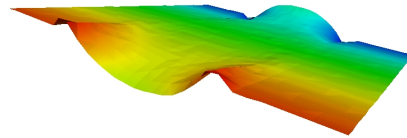


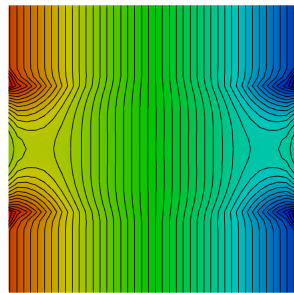
Figure 5.4: **Bingham flow in a channel:** The contours of the unyielded zones with $\|\mathbf{D}(\mathbf{u})\| < 0.1$ at mesh refinement level 5 ($h = 1/32$) for $\epsilon = 10^{-1}, 10^{-2}, 10^{-3}, 10^{-4}, 10^{-5}$ and 0 by using system of equations 5.2 with $\tau_s = 0.25$.



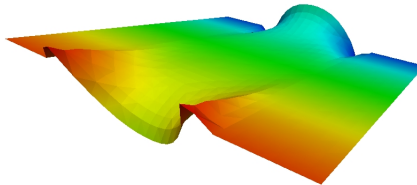
(a) $\epsilon = 10^{-1}$



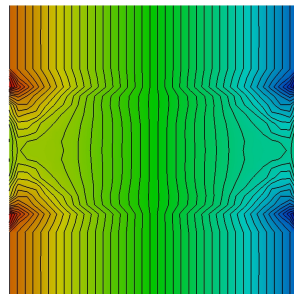
(b) $\epsilon = 10^{-1}$



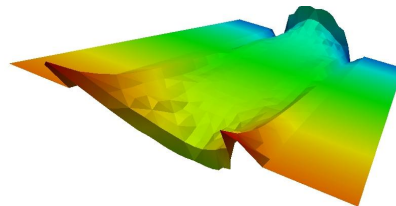
(c) $\epsilon = 10^{-3}$



(d) $\epsilon = 10^{-3}$



(e) $\epsilon = 0$



(f) $\epsilon = 0$

Figure 5.5: **Bingham flow in a channel:** The pressure distributions at mesh refinement level 5 ($h = 1/32$) for $\epsilon = 10^{-1}, 10^{-3}$ and 0 by using system of equations 5.2 with $\tau_s = 0.25$.

5.1. BINGHAM FLUID FLOW IN A CHANNEL

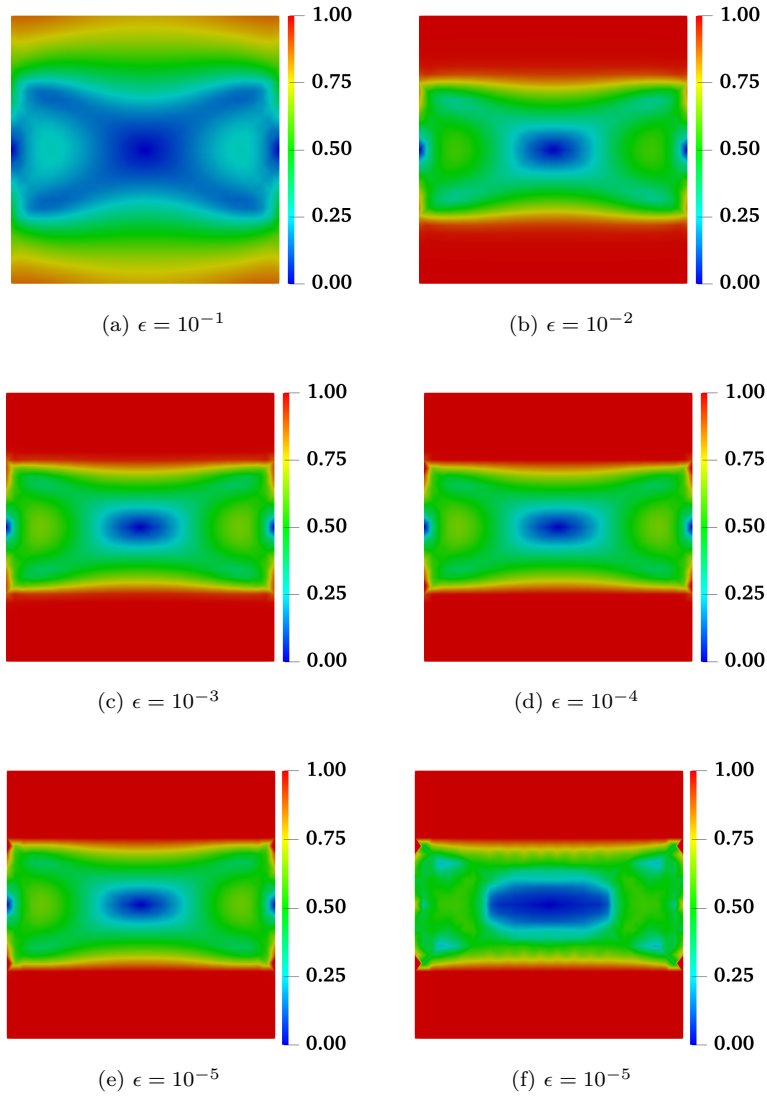


Figure 5.6: **Bingham flow in a channel:** The visualization of $\|\sigma\|$ at mesh refinement level 5 ($h = 1/32$) for $\epsilon = 10^{-1}, 10^{-2}, 10^{-3}, 10^{-4}, 10^{-5}$ and 0 by using system of equations 5.2 with $\tau_s = 0.25$.

5.1.2 Boundary Conditions: Case 2

Instead of assuming all Dirichlet boundary conditions for the velocity, the following boundary conditions are prescribed on the respective boundary parts [82, 37]:

$$\begin{aligned}
 u_2 &= 0 && \text{at inflow and outflow} \\
 \mathbf{u} &= 0 && \text{at upper and lower walls} \\
 \boldsymbol{\tau} \mathbf{n} \cdot \mathbf{n} &= LC && \text{at inflow} \\
 \boldsymbol{\tau} \mathbf{n} \cdot \mathbf{n} &= 0 && \text{at outflow}
 \end{aligned} \tag{5.5}$$

where L is the length of the channel (which is unit in our case) and C is the prescribed normal stress, which reduces to pressure in this case, $C = \frac{\partial p}{\partial x}$ and \mathbf{n} is the unit normal vector. The analytical solution for the Poiseuille flow in case of Bingham fluid is calculated in [1, 81]. The exact solution for the unit length and width channel reads:

$$u_1 = \begin{cases} \frac{C}{2\eta}y(1-y) - \frac{\tau_s}{\eta}y & 0 \leq y < \frac{1}{2} - \frac{\tau_s}{C} \\ \frac{C}{2\eta}\left(\frac{1}{2} - \frac{\tau_s}{\eta}\right)^2 & \frac{1}{2} - \frac{\tau_s}{C} \leq y \leq \frac{1}{2} + \frac{\tau_s}{C} \\ \frac{C}{2\eta}y(1-y) - \frac{\tau_s}{\eta}(1-y) & \frac{1}{2} + \frac{\tau_s}{C} < y \leq 1 \end{cases} \tag{5.6}$$

$$p(x, y) = -C(x - L) \tag{5.7}$$

where $L = 1$ and $C = 1$ in this test case, Fig 5.7 presents the velocity magnitude for the regularized as well as regularization-free case i.e. $\epsilon = 0$ at the refinement level 5 ($h=1/32$), where different flow regimes (shear and plug zones) are developed depending on the yield stress value as expected from the exact solution. It is already mentioned that the value of the regularization parameter has a great influence on the velocity profile inside the channel domain, therefore for $\epsilon = 10^{-3}$, the interface of the plug zone is not accurately captured. On the other hand, when the value of the regularization parameter vanishes (i.e. $\epsilon = 0$), the solution of the velocity in the plug zone perfectly matches with the exact solution shown in Fig. 5.7, the L^2 and H^1 error of the velocity magnitude in Table. [5.2] also present the accuracy of the three-field formulation for regularization-free Bingham solver. The pressure distribution inside the channel is completely linear throughout the domain based on the Poiseuille theory in the infinite channel. Moreover, the magnitude of the new auxiliary stress tensor shows that the $\|\boldsymbol{\sigma}\| < 1$ in the rigid zone, as expected in this channel flow, the analytical expression for the unique solution of velocity, pressure and stress tensor $(\mathbf{u}, p, \boldsymbol{\sigma})$ is calculated already in section (2.4). The blue region in Fig. 5.8 corresponds to nearly zero value of the deformation tensor $\|\mathbf{D}(\mathbf{u})\| \approx 0$ and the symmetric part of the auxiliary stress tensor (σ_{12}) shows its linear change in the plug zone w.r.t. y -axis.

5.1. BINGHAM FLUID FLOW IN A CHANNEL

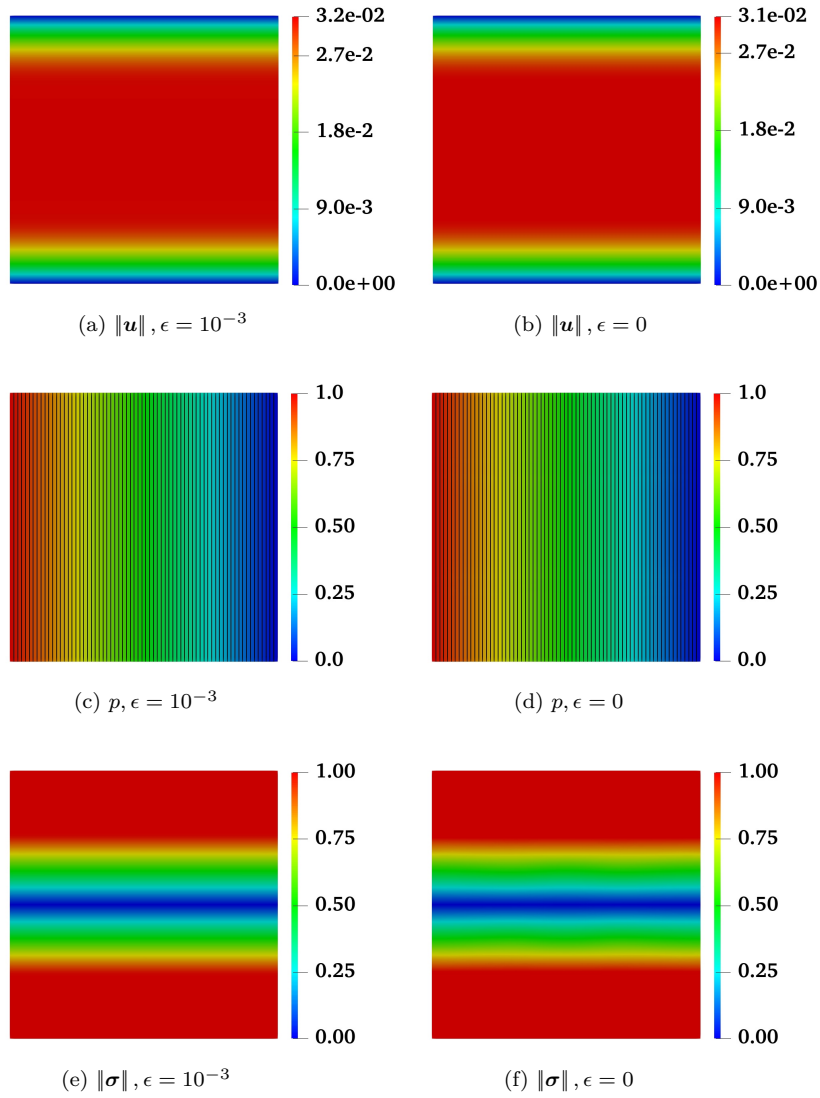


Figure 5.7: **Bingham flow in a channel:** The visualization of $\|\mathbf{u}\|$, p and $\|\boldsymbol{\sigma}\|$ at mesh refinement level 5 ($h = 1/32$) for $\epsilon = 10^{-3}$ (left) and 0 (right) by using system of equations 5.2 with $\tau_s = 0.25$.

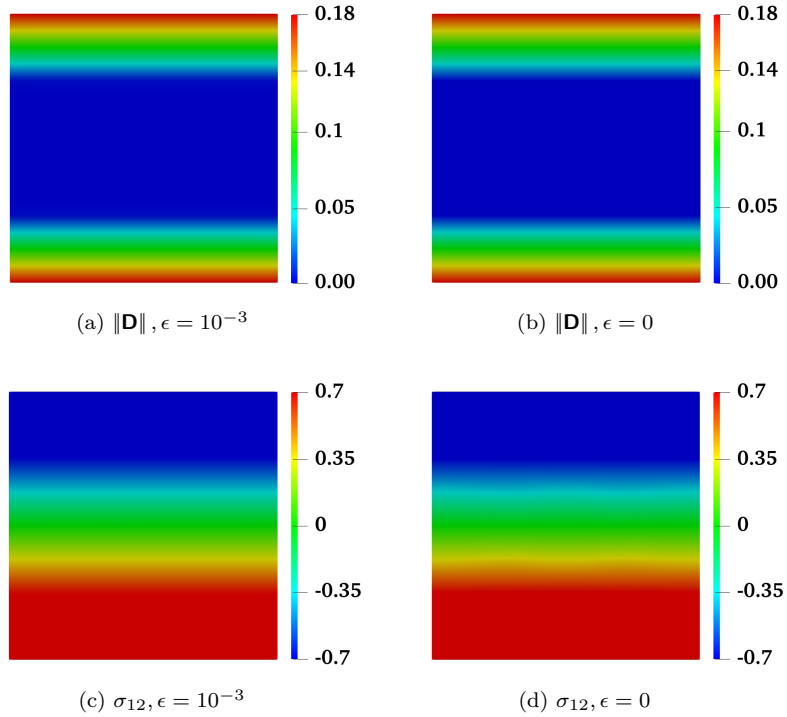


Figure 5.8: **Bingham flow in a channel:** The visualization of $\|\mathbf{D}\|$ and σ_{12} at mesh refinement level 5 ($h = 1/32$) for $\epsilon = 10^{-3}$ (left) and 0 (right) by using system of equations 5.2 with $\tau_s = 0.25$.

Table 5.2: **Bingham flow in a channel:** L^2 and H^1 errors for velocity for $\tau_s = 0.25$ at different mesh refinement levels, the errors are calculated for the regularization-free Bingham.

DOF	L	NL	$\ \mathbf{u} - \mathbf{u}_{\text{ex}}\ _2$	$\ \mathbf{u} - \mathbf{u}_{\text{ex}}\ _1$
4741	3	6	$3.435092763644e - 08$	$2.49700187926642e - 06$
18309	4	6	$1.639790671967e - 08$	$1.32702565344534e - 06$
71941	5	5	$1.637294427502e - 08$	$8.92504780298530e - 07$

So far, the results are obtained using the direct linear solver i.e. Umfpack. In the next sections, the computations are performed with an iterative linear solver i.e. multigrid.

5.2. MULTIGRID PARAMETERS STUDY

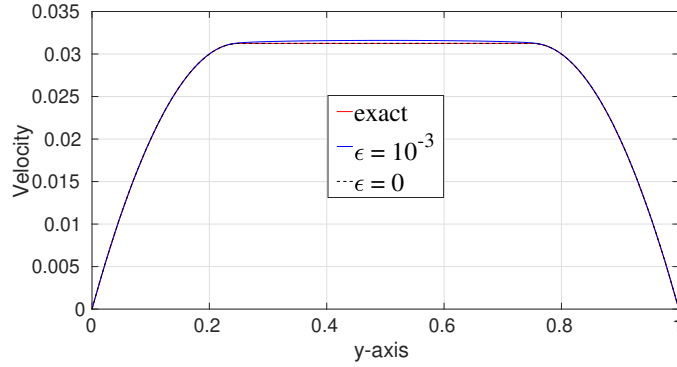


Figure 5.9: **Bingham flow in a channel:** Velocity magnitude at $x = 0$ for $\epsilon = 10^{-3}$ and $\epsilon = 0$, plotted with exact velocity profile for $\tau_s = 0.25$.

5.2 Multigrid Parameters Study

Similar to the Newton method, multigrid linear solver also has several sensitive parameters e.g. smoothing steps, prolongation etc. These parameters can be set according to the requirement of the numerical test, depending on the complexity and challenges of the problem. The same flow configuration of the Bingham fluid flow in a channel is tested with the Newton-multigrid solver shown in Table 5.3, where the "NL" denotes the number of Newton iterations and "LL" are the multigrid average iterations. As expected, the velocity error decreases with decreasing ϵ . However, the solver shows slightly slow convergence in the case of small regularization parameter i.e. $\epsilon = 10^{-3}$. In order to obtain the fast convergence, a detailed study is carried out for this case to obtain the optimal choice of the multigrid parameters.

CHAPTER 5. NUMERICAL STUDY OF BINGHAM

Table 5.3: **Bingham fluid flow in a channel:** Number of Newton-multigrid iterations "NL/LL" for the three-field formulation $(\mathbf{u}, \boldsymbol{\sigma}, p)$ at different mesh refinement levels L for yield stress $\tau_s = 0.25$.

ϵ	L	NL/LL	$\ \mathbf{u} - \mathbf{u}_{\text{ex}}\ $
10^{-1}	3	6/1	2.598×10^{-3}
	4	3/1	2.597×10^{-3}
	5	2/1	2.597×10^{-3}
	6	2/1	2.597×10^{-3}
10^{-2}	3	5/1	5.873×10^{-4}
	4	4/1	5.818×10^{-4}
	5	3/1	5.815×10^{-4}
	6	3/1	5.815×10^{-4}
10^{-3}	3	151/5	6.257×10^{-5}
	4	43/5	6.415×10^{-5}
	5	8/6	6.416×10^{-5}
	6	8/5	6.394×10^{-5}

On the first place, the smoother damping parameter is varied from 1.0 to 0.2 as shown in the Table [5.4]. In this study, the optimal smoother damping parameter turns out to be 0.8 because it gives the faster convergence rate as compared to all other values. On the second place, the effect of the multigrid cycle is studied as shown in the Table [5.5], which concludes that the cycle does not has any significant influence on the current benchmark settings. On the third place, the effect of smoothing steps in combination with the prolongation is carried out in the Table [5.6], which concludes that the optimal value of the smoothing steps and the prolongation are 8 and 0.6, respectively.

5.2. MULTIGRID PARAMETERS STUDY

Table 5.4: **Smoother damping parameter study:** Number of Newton-multigrid iterations "NL/LL" for the Bingham flow in a channel at mesh refinement level 3 ($h = 1/8$) for yield stress $\tau_s = 0.25$, where "lp" denotes the stopping criteria of the linear solver, the regularization parameter is $\epsilon = 10^{-3}$.

ϵ	NL/LL	Smoother Damping	lp
10^{-3}	50/9	1.0	10^{-3}
	8/7	0.8	10^{-3}
	35/9	0.6	10^{-3}
	diverges	0.4	10^{-3}
	diverges	0.2	10^{-3}
10^{-3}	22/10	1.0	10^{-4}
	69/9	0.8	10^{-4}
	diverges	0.6	10^{-4}
	diverges	0.4	10^{-4}
	—	0.2	10^{-4}

Table 5.5: **Multigrid cycle study:** Number of Newton-multigrid iterations "NL/LL" for Bingham flow in a channel at different mesh refinement levels L for the yield stress $\tau_s = 0.25$, where "lp" denotes the stopping criteria of linear solver, the regularization parameter is $\epsilon = 10^{-3}$.

ϵ	L	NL/LL	MG-Cycle	lp
10^{-3}	3	8/7	F	10^{-3}
	4	4/7		10^{-3}
	5	6/9		10^{-3}
	6	4/9		10^{-3}
10^{-3}	3	8/7	V	10^{-3}
	4	4/7		10^{-3}
	5	6/9		10^{-3}
	6	4/9		10^{-3}

CHAPTER 5. NUMERICAL STUDY OF BINGHAM

Table 5.6: **Smoothing steps and prolongation study:** Number of Newton-multigrid iterations "NL/LL" for Bingham flow in a channel at different mesh refinement levels L for the yield stress $\tau_s = 0.25$, where "lp" denotes the stopping criteria of linear solver, the regularization parameter is $\epsilon = 10^{-3}$.

ϵ	L	NL/LL	Smoothing	Prolongation	lp
10^{-3}	3	151/5	4	1.0	10^{-1}
	4	43/5	4	1.0	10^{-1}
	5	8/6	8	1.0	10^{-1}
	6	8/5	8	1.0	10^{-1}
10^{-3}	3	19/8	4	1.0	10^{-2}
	4	40/7	4	1.0	10^{-2}
	5	7/7	4	1.0	10^{-2}
	6	8/5	8	1.0	10^{-2}
10^{-3}	3	7/6	8	0.2	10^{-2}
	4	12/6	8	0.2	10^{-2}
	5	12/9	8	0.2	10^{-2}
	6	28/8	8	0.2	10^{-2}
10^{-3}	3	9/6	8	0.4	10^{-2}
	4	13/5	8	0.4	10^{-2}
	5	7/8	8	0.4	10^{-2}
	6	12/6	8	0.4	10^{-2}
10^{-3}	3	12/8	8	0.4	10^{-3}
	4	11/8	8	0.4	10^{-3}
	5	8/9	8	0.4	10^{-3}
	6	7/9	8	0.4	10^{-3}
10^{-3}	3	27/9	8	0.2	10^{-3}
	4	8/8	8	0.2	10^{-3}
	5	11/9	8	0.2	10^{-3}
	6	-	8	0.2	10^{-3}
10^{-3}	3	8/7	8	0.6	10^{-3}
	4	4/7	8	0.6	10^{-3}
	5	6/9	8	0.6	10^{-3}
	6	4/9	8	0.6	10^{-3}

5.3. BINGHAM FLOW IN A CHANNEL WITH EOFEM STABILIZATION

From Table [5.3] it can be concluded that the multigrid can solve the Bingham fluid upto the moderate value of the regularization parameter but the regularization-free Bingham is difficult to obtain with the current settings. One possible remedy can be the addition of some kind of stabilization, therefore, at the first place the edge oriented FEM stabilization is added and discussed in the next section.

5.3 Bingham Flow in a Channel with EOFEM Stabilization

In order to achieve the solution of regularization-free Bingham with the Newton-multigrid solver, the numerical studies for the stationary Bingham fluid flow in a channel are performed by applying the edge oriented stabilization.

In the first step, the stabilization $\gamma_{\mathbf{u}}h$ is added in the velocity term and its effects on the accuracy of the solution are investigated. For the sake of comparison with the already calculated results (Table [5.1]) without any stabilization, we add the eofem into the Newton-umfpack solver and the corresponding comparison study is shown in the Table [5.7], where the $\gamma_{\mathbf{u}}$ is set as 10^{-1} . The results clearly concludes that the eofem does not harm the solution accuracy.

In the second step, eofem is added while using the multigrid as the linear solver, shown in Table [5.8]. In this table, two values of $\gamma_{\mathbf{u}}$ (i.e. 2.5×10^{-2} and 1.0×10^{-1}) are tested for the regularization parameter $\epsilon = 10^{-3}$ and the results show that the solution remains undisturbed for both values of $\gamma_{\mathbf{u}}$. Afterwards, the study is extended for all values of regularization parameter ϵ , given in Table [5.9]. The Newton-multigrid solver is able to solve for $\epsilon = 10^{-4}$, which is a clear improvement in the solver after adding the eofem stabilization. Moreover, the solver can converge with a decent number of iterations, which was not the case earlier. One more comparison study is carried out between the direct and iterative linear solver after adding the eofem, i.e. umfpack and multigrid respectively, shown in Table [5.10]. The results describe that the accuracy of the solution is sustained in all the cases but the task of regularization-free Bingham with Newton-multigrid is still not achieved.

In the third step, the contribution of the stabilization was reduced by adding h^2 (instead of h) shown in Table [5.11], which slightly reduces the nonlinear iterations by keeping the accuracy of the solution unharmed. On the other side, the linear solver becomes a little bit slower because of the less contribution of the stabilization term h^2 with the mesh refinement. Hence, the eofem in the velocity term does not seems to be so much helpful for achieving the regularization-free Bingham.

Therefore, the next idea is to add stabilization in the stress tensor i.e. $\gamma_{\sigma}h$, where γ_{σ} is set as 10^{-2} in the Table [5.12]. A new improvement from the multigrid solver is achieved by solving the smallest $\epsilon = 10^{-5}$ with this stabilization.

CHAPTER 5. NUMERICAL STUDY OF BINGHAM

Nevertheless, the solution with vanishing regularization ($\epsilon = 0$) is yet to be achieved with the Newton-multigrid solver, so the idea of adding some other kind of stabilization (e.g. artificial diffusion) might be helpful in this regard, which is discussed in the next section.

Table 5.7: **Bingham flow in a channel:** Comparison of Newton iterations with and without eofem stabilization in velocity (\mathbf{u}), where $\gamma_u = 10^{-1}$, for different mesh refinement levels L and regularization parameter ϵ , yield stress $\tau_s = 0.25$.

ϵ	L	EOFEM			
		NL	$\ \mathbf{u} - \mathbf{u}_{\text{ex}}\ $	NL	$\ \mathbf{u} - \mathbf{u}_{\text{ex}}\ $
10^{-1}	2	6	2.641×10^{-3}	6	2.627×10^{-3}
	3	3	2.598×10^{-3}	3	2.598×10^{-3}
	4	2	2.596×10^{-3}	3	2.597×10^{-3}
	5	2	2.597×10^{-3}	2	2.597×10^{-3}
	6	1	2.597×10^{-3}	2	2.567×10^{-3}
10^{-2}	2	9	6.079×10^{-4}	9	6.130×10^{-4}
	3	5	5.873×10^{-4}	5	5.893×10^{-4}
	4	4	5.818×10^{-4}	4	5.819×10^{-4}
	5	4	5.815×10^{-4}	3	5.815×10^{-4}
	6	3	5.815×10^{-4}	3	5.815×10^{-4}
10^{-3}	2	19	6.237×10^{-5}	15	6.228×10^{-5}
	3	7	6.257×10^{-5}	5	6.296×10^{-5}
	4	5	6.415×10^{-5}	5	6.426×10^{-5}
	5	4	6.416×10^{-5}	5	6.418×10^{-5}
	6	3	6.395×10^{-5}	4	6.395×10^{-5}
10^{-4}	2	15	7.835×10^{-6}	14	7.564×10^{-6}
	3	14	6.407×10^{-6}	9	6.300×10^{-6}
	4	4	6.262×10^{-6}	5	6.265×10^{-6}
	5	4	6.298×10^{-6}	4	6.308×10^{-6}
	6	3	6.286×10^{-6}	4	6.304×10^{-6}

5.3. BINGHAM FLOW IN A CHANNEL WITH EOFEM STABILIZATION

Table 5.8: **Bingham flow in a channel:** Comparison of Newton-multigrid iterations with and without eofem stabilization in velocity (\mathbf{u}) of different γ_u , for different mesh refinement levels L and $\epsilon = 10^{-3}$, yield stress $\tau_s = 0.25$.

γ_u	L	EOFEM			
		NL/LL	$\ \mathbf{u} - \mathbf{u}_{\text{ex}}\ $	NL/LL	$\ \mathbf{u} - \mathbf{u}_{\text{ex}}\ $
2.5×10^{-2}	2	19/1	6.237×10^{-5}	15/1	6.228×10^{-5}
	3	7/7	6.257×10^{-5}	6/5	6.258×10^{-5}
	4	4/3	6.415×10^{-5}	5/4	6.415×10^{-5}
	5	4/4	6.416×10^{-5}	4/4	6.416×10^{-5}
	6	6/6	6.395×10^{-5}	4/4	6.395×10^{-5}
1.0×10^{-1}	2	19/1	6.237×10^{-5}	15/1	6.228×10^{-5}
	3	7/7	6.257×10^{-5}	5/4	6.296×10^{-5}
	4	4/3	6.415×10^{-5}	5/4	6.426×10^{-5}
	5	4/4	6.416×10^{-5}	4/3	6.418×10^{-5}
	6	6/6	6.395×10^{-5}	4/4	6.395×10^{-5}

Table 5.9: **Bingham flow in a channel:** Comparison of Newton iterations with and without eofem stabilization in velocity (\mathbf{u}), where $\gamma_u = 2.5 \times 10^{-2}$, for different mesh refinement levels L and regularization parameter ϵ , yield stress $\tau_s = 0.25$.

ϵ	L	EOFEM			
		NL/LL	$\ \mathbf{u} - \mathbf{u}_{\text{ex}}\ $	NL/LL	$\ \mathbf{u} - \mathbf{u}_{\text{ex}}\ $
10^{-1}	2	6/1	2.641×10^{-3}	6/1	2.627×10^{-3}
	3	4/1	2.598×10^{-3}	4/1	2.598×10^{-3}
	4	3/1	2.596×10^{-3}	3/1	2.597×10^{-3}
	5	3/1	2.597×10^{-3}	3/1	2.597×10^{-3}
	6	2/1	2.597×10^{-3}	2/1	2.567×10^{-3}
10^{-2}	2	9/1	6.079×10^{-4}	9/1	6.130×10^{-4}
	3	5/1	5.873×10^{-4}	5/1	5.893×10^{-4}
	4	4/1	5.818×10^{-4}	4/2	5.819×10^{-4}
	5	4/1	5.815×10^{-4}	3/1	5.814×10^{-4}
	6	3/1	5.815×10^{-4}	3/2	5.815×10^{-4}
10^{-3}	2	15/1	6.237×10^{-5}	15/1	6.228×10^{-5}
	3	7/7	6.257×10^{-5}	6/2	6.296×10^{-5}
	4	4/3	6.415×10^{-5}	5/1	6.426×10^{-5}
	5	4/4	6.416×10^{-5}	5/2	6.418×10^{-5}
	6	3/4	6.395×10^{-5}	4/2	6.395×10^{-5}
10^{-4}	2	-	-	14/1	6.228×10^{-6}
	3	-	-	12/4	6.504×10^{-6}
	4	-	-	10/7	6.339×10^{-6}
	5	-	-	11/8	6.338×10^{-6}

CHAPTER 5. NUMERICAL STUDY OF BINGHAM

Table 5.10: **Bingham flow in a channel:** Comparison of Newton and Newton-MG iterations with eofem stabilization in velocity (\mathbf{u}), where $\gamma_u = 10^{-1}$, for different mesh refinement levels L and regularization parameter ϵ , yield stress $\tau_s = 0.25$.

ϵ	L	Newton		Newton-MG	
		NL/LL	$\ \mathbf{u} - \mathbf{u}_{\text{ex}}\ $	NL/LL	$\ \mathbf{u} - \mathbf{u}_{\text{ex}}\ $
10^{-1}	2	5	2.627×10^{-3}	5/1	2.627×10^{-3}
	3	2	2.598×10^{-3}	4/1	2.598×10^{-3}
	4	2	2.597×10^{-3}	4/1	2.597×10^{-3}
	5	1	2.597×10^{-3}	3/1	2.597×10^{-3}
	6	1	2.597×10^{-3}	2/1	2.597×10^{-3}
10^{-2}	2	7	6.130×10^{-4}	7/1	6.130×10^{-4}
	3	2	5.893×10^{-4}	4/1	5.873×10^{-4}
	4	2	5.819×10^{-4}	4/1	5.819×10^{-4}
	5	2	5.814×10^{-4}	4/1	5.814×10^{-4}
	6	1	5.814×10^{-4}	3/1	5.815×10^{-4}
10^{-3}	2	11	6.228×10^{-5}	11/1	6.228×10^{-5}
	3	4	6.296×10^{-5}	4/8	6.296×10^{-5}
	4	3	6.426×10^{-5}	3/9	6.265×10^{-5}
	5	3	6.418×10^{-5}	3/9	6.308×10^{-5}
10^{-4}	2	14	7.564×10^{-6}	14/1	7.832×10^{-6}
	3	5	6.300×10^{-6}	8/6	6.300×10^{-6}
	4	4	6.265×10^{-6}	8/7	6.265×10^{-6}
	5	5	6.307×10^{-6}	12/8	6.308×10^{-6}
10^{-5}	2	20	9.323×10^{-7}	25/1	9.323×10^{-7}
	3	6	6.672×10^{-7}	-	-
	4	5	6.369×10^{-7}	-	-
	5	4	6.293×10^{-7}	-	-

5.3. BINGHAM FLOW IN A CHANNEL WITH EOFEM STABILIZATION

Table 5.11: **Bingham flow in a channel:** Comparison of Newton and Newton-MG iterations with eofem stabilization $\gamma_u h^2$, where $\gamma_u = 10^{-1}$, for different mesh refinement levels L and regularization parameter ϵ , yield stress $\tau_s = 0.25$.

ϵ	L	Newton		Newton-MG	
		NL/LL	$\ \mathbf{u} - \mathbf{u}_{ex}\ $	NL/LL	$\ \mathbf{u} - \mathbf{u}_{ex}\ $
10^{-1}	2	5	2.621×10^{-3}	5/1	2.621×10^{-3}
	3	2	2.597×10^{-3}	4/1	2.598×10^{-3}
	4	2	2.596×10^{-3}	3/1	2.597×10^{-3}
	5	1	2.597×10^{-3}	2/1	2.597×10^{-3}
	6	1	2.597×10^{-3}	2/1	2.597×10^{-3}
10^{-2}	2	7	6.100×10^{-4}	7/1	6.100×10^{-4}
	3	2	5.779×10^{-4}	5/1	5.876×10^{-4}
	4	2	5.794×10^{-4}	4/1	5.818×10^{-4}
	5	2	5.808×10^{-4}	3/1	5.815×10^{-4}
	6	1	5.814×10^{-4}	3/1	5.815×10^{-4}
10^{-3}	2	11	6.234×10^{-5}	11/1	6.234×10^{-5}
	3	3	6.258×10^{-5}	6/2	6.262×10^{-5}
	4	4	6.415×10^{-5}	5/2	6.415×10^{-5}
	5	3	6.415×10^{-5}	5/3	6.416×10^{-5}
10^{-4}	2	13	7.713×10^{-6}	13/1	7.713×10^{-6}
	3	2	5.481×10^{-6}	8/7	6.382×10^{-6}
	4	2	6.139×10^{-6}	7/9	6.265×10^{-6}
	5	1	6.297×10^{-6}	8/18	6.298×10^{-6}
10^{-5}	2	34	9.408×10^{-7}	-	-
	3	7	6.758×10^{-7}	-	-
	4	6	6.380×10^{-7}	-	-
	5	4	6.304×10^{-7}	-	-

CHAPTER 5. NUMERICAL STUDY OF BINGHAM

Table 5.12: **Bingham flow in a channel:** Comparison of Newton-multigrid iterations with and without eofem stabilization in the stress (σ), where $\gamma_\sigma = 10^{-2}$ for different mesh refinement levels L and regularization parameter ϵ , yield stress $\tau_s = 0.25$.

ϵ	L	EOFEM			
		NL/LL	$\ \mathbf{u} - \mathbf{u}_{\text{ex}}\ $	NL/LL	$\ \mathbf{u} - \mathbf{u}_{\text{ex}}\ $
10^{-1}	2	6/1	2.641×10^{-3}	3/1	2.616×10^{-3}
	3	4/1	2.598×10^{-3}	4/1	2.598×10^{-3}
	4	3/1	2.596×10^{-3}	3/1	2.597×10^{-3}
	5	3/1	2.597×10^{-3}	3/1	2.597×10^{-3}
10^{-2}	2	9/1	6.079×10^{-4}	3/1	6.018×10^{-4}
	3	5/1	5.873×10^{-4}	4/1	5.874×10^{-4}
	4	4/1	5.818×10^{-4}	5/1	5.819×10^{-4}
	5	4/1	5.815×10^{-4}	4/2	5.815×10^{-4}
10^{-3}	2	15/1	6.237×10^{-5}	15/1	6.257×10^{-5}
	3	7/7	6.257×10^{-5}	6/3	6.287×10^{-5}
	4	4/3	6.415×10^{-5}	6/2	6.437×10^{-5}
	5	4/4	6.416×10^{-5}	5/4	6.417×10^{-5}
10^{-4}	2	-	-	21/1	8.919×10^{-6}
	3	-	-	7/7	6.650×10^{-6}
	4	-	-	7/4	6.985×10^{-6}
	5	-	-	6/6	6.900×10^{-6}
10^{-5}	2	-	-	9/1	9.772×10^{-7}
	3	-	-	5/1	2.743×10^{-6}
	4	-	-	11/34	3.003×10^{-6}

5.4 Bingham Flow in a Channel with Artificial Diffusion Stabilization

The aim of adding the artificial diffusion stabilization is to achieve the solution of regularization-free Bingham with the nice behaviour of multigrid solver for the direct steady state Bingham problem. Therefore, the three-field $(\mathbf{u}, \boldsymbol{\sigma}, p)$ system of equations after the addition of artificial diffusion stabilization reads as follows:

$$\begin{cases} \|\mathbf{D}(\mathbf{u})\|_{\epsilon} \boldsymbol{\sigma} - \mathbf{D}(\mathbf{u}) + \gamma h^2 \Delta \boldsymbol{\sigma} = 0 & \text{in } \Omega \\ -\nabla \cdot (2\eta \mathbf{D}(\mathbf{u}) + \tau_s \boldsymbol{\sigma}) + \nabla p = 0 & \text{in } \Omega \\ \nabla \cdot \mathbf{u} = 0 & \text{in } \Omega \\ \mathbf{u} = \mathbf{g}_D & \text{on } \Gamma_D \end{cases} \quad (5.8)$$

where the parameter γ is multiplied with h^2 , which implies that it's effect will reduce with the the mesh refinement (h).

In the first step, a comparison study is carried out between Newton-umfpack and Newton-multigrid solvers shown in Table [5.13], where γ is set to 10^{-2} . The results illustrates that in the presence of artificial diffusion, both solvers exhibit good convergence rate. However, the accuracy of the solution is a little bit compromised. Nevertheless, the Newton-multigrid solver has successfully achieved the goal of solving regularization-free Bingham fluid flow. The accuracy of the solution can be increased by choosing the suitable value of γ , therefore, the value of the γ is decreased to $\gamma = 10^{-3}$ and $\gamma = 10^{-4}$ in the Table [5.14] and [5.15], respectively. The effect of reducing γ can be seen from velocity error $\|\mathbf{u} - \mathbf{u}_{\text{ex}}\|$, which reduces at higher mesh refinement levels. Based on the convergence rate and velocity error from the parameter γ study, it can be concluded that the $\gamma = 10^{-3}$ is optimal value for these numerical tests.

In the second step, we fix γ to the optimal value and reduce the contribution of the stabilization from the mesh size by multiplying it with h^3 in order to improve the accuracy of the solution. The corresponding results are shown in Table [5.16]. As expected, the velocity error gets smaller with the mesh refinements due to the less contribution from the stabilization term, on the other hand, the solver slightly slows down and the convergence is achieved with more number of iterations.

In this third step, another idea can be applied to improve the accuracy of the approximated solution, by choosing different values of γ for the Jacobian matrix (γ_j) and the residuals (γ_d). The basic purpose is to keep the value of γ_d small in order to have less effects on the defect and the value of γ_j big in order to help the solver in convergence. Table [5.17] shows that the idea did not fully supported in the current test case because the convergence rate gets very slow even for bigger ϵ . Therefore, sticking to the old strategy and keeping the same γ for the Jacobian and residual, we can conclude that the artificial diffusion stabilization helps the multigrid to solve regularization-free Bingham fluid with acceptable accurate results.

CHAPTER 5. NUMERICAL STUDY OF BINGHAM

Table 5.13: **Bingham flow in a channel:** Comparison of Newton and Newton-multigrid iterations with artificial diffusion stabilization γh^2 , where $\gamma = 10^{-2}$, for different mesh refinement levels L and regularization parameter ϵ , yield stress $\tau_s = 0.25$.

ϵ	L	Newton		Newton-MG	
		NL	$\ \mathbf{u} - \mathbf{u}_{\text{ex}}\ $	NL/L	$\ \mathbf{u} - \mathbf{u}_{\text{ex}}\ $
10^{-1}	2	5	2.633×10^{-3}	5/1	2.633×10^{-3}
	3	3	2.621×10^{-3}	3/2	2.621×10^{-3}
	4	3	2.607×10^{-3}	3/4	2.607×10^{-3}
	5	2	2.601×10^{-3}	2/5	2.601×10^{-3}
	6	2	2.598×10^{-3}	2/5	2.598×10^{-3}
10^{-2}	2	7	1.384×10^{-3}	7/1	1.384×10^{-3}
	3	4	8.964×10^{-4}	4/6	8.964×10^{-4}
	4	3	6.887×10^{-4}	3/3	6.887×10^{-4}
	5	2	6.159×10^{-4}	3/4	6.159×10^{-4}
	6	2	5.919×10^{-4}	3/5	5.919×10^{-4}
10^{-3}	2	7	1.245×10^{-3}	7/1	1.245×10^{-3}
	3	4	5.811×10^{-4}	5/9	5.811×10^{-4}
	4	4	2.326×10^{-4}	4/8	2.326×10^{-4}
	5	4	1.107×10^{-4}	3/6	1.107×10^{-4}
	6	4	7.725×10^{-5}	3/8	7.725×10^{-5}
10^{-4}	2	7	1.243×10^{-3}	7/1	1.243×10^{-3}
	3	4	5.724×10^{-4}	4/6	5.724×10^{-4}
	4	4	2.056×10^{-4}	4/5	2.056×10^{-4}
	5	4	6.740×10^{-5}	4/6	6.740×10^{-5}
	6	4	2.670×10^{-5}	5/6	2.670×10^{-5}
10^{-5}	2	7	1.243×10^{-3}	7/1	1.243×10^{-3}
	3	4	5.724×10^{-4}	6/2	5.724×10^{-4}
	4	4	2.056×10^{-4}	4/3	2.056×10^{-4}
	5	4	6.636×10^{-5}	4/5	6.636×10^{-5}
	6	4	2.458×10^{-5}	5/6	2.458×10^{-5}
0	2	3	1.243×10^{-3}	3/1	1.243×10^{-3}
	3	3	5.724×10^{-4}	4/1	5.724×10^{-4}
	4	3	2.056×10^{-4}	5/2	2.056×10^{-4}
	5	3	6.635×10^{-5}	5/2	6.635×10^{-5}
	6	6	2.459×10^{-5}	6/9	2.459×10^{-5}

5.4. BINGHAM FLOW IN A CHANNEL WITH ARTIFICIAL DIFFUSION STABILIZATION

Table 5.14: **Bingham flow in a channel:** Comparison of Newton and Newton-MG iterations with and without artificial diffusion stabilization γh^2 , where $\gamma = 10^{-3}$, for different mesh refinement levels L and regularization parameter ϵ , yield stress $\tau_s = 0.25$.

L	Newton			Newton-MG		
	Stab.		$\ u - u_{ex}\ $	Stab.		$\ u - u_{ex}\ $
	NL	NL		NL /LL	NL/LL	
$\epsilon = 10^{-1}$						
2	6	6	2.648×10^{-3}	6/1	6/1	2.641×10^{-3}
3	3	3	2.603×10^{-3}	3/2	3/2	2.598×10^{-3}
4	2	2	2.598×10^{-3}	2/4	3/2	2.597×10^{-3}
5	2	2	2.597×10^{-3}	2/3	2/4	2.597×10^{-3}
6	2	1	2.597×10^{-3}	2/4	2/4	2.597×10^{-3}
$\epsilon = 10^{-2}$						
2	8	9	7.764×10^{-4}	9/1	8/1	6.079×10^{-4}
3	3	5	6.364×10^{-4}	5/2	3/2	5.873×10^{-4}
4	3	4	5.974×10^{-4}	4/3	3/3	5.818×10^{-4}
5	3	4	5.860×10^{-4}	4/4	3/3	5.815×10^{-4}
6	2	3	5.827×10^{-4}	3/5	2/4	5.827×10^{-4}
$\epsilon = 10^{-3}$						
2	9	12	3.457×10^{-4}	12/1	9/1	6.237×10^{-5}
3	4	8	1.452×10^{-4}	9/20	4/2	6.257×10^{-5}
4	4	8	8.630×10^{-5}	7/9	4/2	6.415×10^{-5}
5	4	5	7.022×10^{-5}	7/16	4/3	6.417×10^{-5}
6	5	4	6.569×10^{-5}	6/11	4/4	6.395×10^{-5}
$\epsilon = 10^{-4}$						
2	9	15	3.306×10^{-4}	-	10/1	7.835×10^{-6}
3	6	14	1.117×10^{-4}	-	6/4	6.407×10^{-6}
4	7	4	4.155×10^{-5}	-	5/5	6.262×10^{-6}
5	5	4	1.787×10^{-5}	-	7/6	6.298×10^{-6}
6	6	-	9.418×10^{-6}	-	6/8	6.284×10^{-6}
$\epsilon = 10^{-5}$						
2	17	-	3.304×10^{-4}	-	17/1	-
3	7	39	1.112×10^{-4}	-	6/4	6.788×10^{-7}
4	6	13	4.041×10^{-5}	-	5/3	6.378×10^{-7}
5	5	5	1.563×10^{-5}	-	7/6	6.297×10^{-7}
6	6	-	5.840×10^{-6}	-	7/8	-
$\epsilon = 0$						
2	3	-	-	-	3/1	3.304×10^{-4}
3	4	-	-	-	6/2	1.112×10^{-4}
4	4	-	-	-	6/4	4.040×10^{-5}
5	5	-	-	-	6/11	1.557×10^{-5}
6	11	-	-	-	12/22	5.694×10^{-6}

CHAPTER 5. NUMERICAL STUDY OF BINGHAM

Table 5.15: **Bingham flow in a channel:** Comparison of Newton and Newton-MG iterations with artificial diffusion stabilization γh^2 , where $\gamma = 10^{-4}$, for different mesh refinement levels L and regularization parameter ϵ , yield stress $\tau_s = 0.25$.

ϵ	L	Newton		Newton-MG	
		NL	$\ \mathbf{u} - \mathbf{u}_{\text{ex}}\ $	NL/L	$\ \mathbf{u} - \mathbf{u}_{\text{ex}}\ $
10^{-1}	2	6	2.642×10^{-3}	6/1	2.642×10^{-3}
	3	3	2.599×10^{-3}	3/2	2.599×10^{-3}
	4	3	2.597×10^{-3}	3/3	2.597×10^{-3}
	5	2	2.597×10^{-3}	2/3	2.597×10^{-3}
	6	2	2.597×10^{-3}	2/3	2.597×10^{-3}
10^{-2}	2	9	6.232×10^{-4}	9/1	6.232×10^{-4}
	3	5	5.937×10^{-4}	5/4	5.937×10^{-4}
	4	4	5.836×10^{-4}	4/3	5.836×10^{-4}
	5	4	5.820×10^{-4}	4/4	5.820×10^{-4}
	6	3	5.816×10^{-4}	3/4	5.816×10^{-4}
10^{-3}	2	21	9.234×10^{-5}	21/1	9.234×10^{-5}
	3	6	7.413×10^{-5}	7/6	7.413×10^{-5}
	4	5	6.728×10^{-5}	8/9	6.728×10^{-5}
	5	5	6.486×10^{-5}	6/8	6.486×10^{-5}
	6	6	6.414×10^{-5}	6/12	6.414×10^{-5}
10^{-4}	2	29	4.428×10^{-5}	24/1	4.428×10^{-5}
	3	6	2.418×10^{-5}	12/11	2.418×10^{-5}
	4	6	1.299×10^{-5}	11/4	1.299×10^{-5}
	5	8	8.243×10^{-6}	10/4	8.243×10^{-6}
	6	5	7.023×10^{-6}	9/4	7.023×10^{-6}
10^{-5}	2	12	4.304×10^{-5}	12/1	4.304×10^{-5}
	3	3	2.226×10^{-5}	4/11	2.224×10^{-5}
	4	5	1.075×10^{-5}	6/12	1.062×10^{-5}
	5	9	4.953×10^{-6}	13/28	4.567×10^{-6}
	6	10	2.577×10^{-6}	16/47	2.313×10^{-6}
0	2	4	4.292×10^{-5}	4/1	4.292×10^{-5}
	3	5	2.225×10^{-5}	6/7	2.225×10^{-5}
	4	6	1.012×10^{-5}	7/6	1.012×10^{-5}
	5	10	4.448×10^{-6}	13/15	4.448×10^{-6}

5.4. BINGHAM FLOW IN A CHANNEL WITH ARTIFICIAL DIFFUSION STABILIZATION

Table 5.16: **Bingham flow in a channel:** Comparison of Newton and Newton-MG iterations with artificial diffusion stabilization $\gamma_\sigma h^3$, where $\gamma = 10^{-2}$, for different mesh refinement levels L and regularization parameter ϵ , yield stress $\tau_s = 0.25$.

ϵ	L	Newton		Newton-MG	
		NL	$\ \mathbf{u} - \mathbf{u}_{\text{ex}}\ $	NL/L	$\ \mathbf{u} - \mathbf{u}_{\text{ex}}\ $
10^{-1}	2	3	2.651×10^{-3}	3/1	2.651×10^{-3}
	3	2	2.604×10^{-3}	3/1	2.604×10^{-3}
	4	2	2.598×10^{-3}	3/1	2.598×10^{-3}
	5	1	2.597×10^{-3}	2/1	2.597×10^{-3}
	6	1	2.597×10^{-3}	3/2	2.597×10^{-3}
10^{-2}	2	6	9.336×10^{-4}	6/1	9.336×10^{-4}
	3	2	6.465×10^{-4}	5/1	6.465×10^{-4}
	4	2	5.920×10^{-4}	4/1	5.920×10^{-4}
	5	2	5.830×10^{-4}	4/1	5.830×10^{-4}
	6	1	5.816×10^{-4}	3/2	5.816×10^{-4}
10^{-3}	2	6	6.121×10^{-4}	6/1	6.121×10^{-4}
	3	3	1.622×10^{-4}	6/1	1.622×10^{-4}
	4	3	7.902×10^{-5}	8/1	7.902×10^{-5}
	5	3	6.626×10^{-5}	10/1	6.626×10^{-5}
	6	2	6.432×10^{-5}	5/2	6.432×10^{-5}
10^{-4}	2	6	6.046×10^{-4}	6/1	6.046×10^{-4}
	3	3	1.306×10^{-4}	6/2	1.306×10^{-4}
	4	4	3.203×10^{-5}	6/5	3.206×10^{-5}
	5	3	1.110×10^{-5}	9/6	1.113×10^{-6}
	6	4	6.867×10^{-6}	7/6	6.823×10^{-6}
10^{-5}	2	6	6.045×10^{-4}	6/1	6.045×10^{-4}
	3	3	1.302×10^{-4}	6/2	1.302×10^{-4}
	4	4	3.076×10^{-5}	6/2	3.076×10^{-5}
	5	5	8.498×10^{-6}	8/12	8.498×10^{-6}
	6	15	2.443×10^{-6}	11/12	2.443×10^{-6}
10^{-6}	2	6	6.045×10^{-4}	6/1	6.122×10^{-4}
	3	2	1.293×10^{-4}	6/2	1.302×10^{-4}
	4	2	3.072×10^{-5}	6/2	3.076×10^{-5}
	5	2	9.826×10^{-6}	8/13	8.435×10^{-6}
	6	3	3.308×10^{-6}	21/13	3.308×10^{-6}
0	2	6	6.045×10^{-4}	6/1	6.045×10^{-4}
	3	3	1.302×10^{-4}	6/2	1.302×10^{-4}
	4	4	3.072×10^{-5}	6/5	3.072×10^{-5}
	5	5	8.436×10^{-6}	10/15	8.436×10^{-6}
	6	17	2.274×10^{-6}	33/25	2.263×10^{-6}

CHAPTER 5. NUMERICAL STUDY OF BINGHAM

Table 5.17: **Bingham flow in a channel:** Comparison of Newton and Newton-MG iterations with artificial diffusion stabilization γh^2 , where $\gamma_j = 10^{-3}$ and $\gamma_d = 10^{-4}$, for different mesh refinement levels L and regularization parameter ϵ , yield stress $\tau_s = 0.25$.

ϵ	L	Newton		Newton-MG	
		NL	$\ \mathbf{u} - \mathbf{u}_{\text{ex}}\ $	NL/L	$\ \mathbf{u} - \mathbf{u}_{\text{ex}}\ $
10^{-1}	2	12	2.642×10^{-3}	12/1	2.642×10^{-3}
	3	8	2.599×10^{-3}	7/1	2.599×10^{-3}
	4	5	2.597×10^{-3}	5/2	2.597×10^{-3}
	5	4	2.597×10^{-3}	4/3	2.597×10^{-3}
	6	2	2.597×10^{-3}	2/3	2.597×10^{-3}
10^{-2}	2	33	6.232×10^{-4}	33/1	6.232×10^{-4}
	3	26	5.937×10^{-4}	26/4	5.937×10^{-4}
	4	21	5.836×10^{-4}	20/3	5.836×10^{-4}
	5	13	5.820×10^{-4}	13/5	5.820×10^{-4}
	6	8	5.816×10^{-4}	8/3	5.816×10^{-4}
10^{-3}	2	69	9.234×10^{-5}	69/1	9.234×10^{-5}
	3	54	7.413×10^{-5}	53/14	7.413×10^{-5}
	4	39	6.728×10^{-5}	40/5	6.728×10^{-5}
	5	29	6.486×10^{-5}	28/5	6.486×10^{-5}
	6	19	6.414×10^{-5}	20/5	6.414×10^{-5}

Chapter 6

Adaptive Discrete Newton

This chapter is devoted to the insights of our newly developed adaptive discrete Newton approach for any nonlinear problem. A comprehensive description of the efficiency and the robustness of this method is explained with the help of graphical representation of the solver's behaviour. Several comparison studies for different benchmarks configurations are carried out between classical and the new adaptive discrete Newton.

6.1 Adaptive Discrete Newton

Devoting our attention back to the details of Newton method explained in the section (4.1), which uses the approximated Jacobian matrix, calculated using divided difference. This method consists of some sensitive parameters in the algorithm 1 e.g. initial solution and the damping factor ω . The approximation of the derivatives is carried out with the following equation, where the j -th column is given as follows:

$$\left[\frac{\partial \mathcal{R}(\mathcal{U}^n)}{\partial \mathcal{U}^n} \right]_j \approx \frac{\mathcal{R}(\mathcal{U}^n + \chi \delta_j) - \mathcal{R}(\mathcal{U}^n - \chi \delta_j)}{2\chi} \quad (6.1)$$

here δ_j is the vector with unit j -th component and zero otherwise, χ is the step-size and chosen as a free parameter. The parameter χ plays a very important role in the convergence rate of the discrete Newton solver. The advantage of such Newton method is that it acts in a black box manner. Therefore, it handles any nonlinearity coming from the equations automatically, without deriving the corresponding calculations. However, the choice of the χ is really important as it is a free parameter and the right choice is a very delicate task because it has a strong impact on the accuracy and robustness of any difference method [69]. Based on the perturbation analysis for the residuum, it can be a fixed constant and often chosen according to the machine precision [64]. On the other hand,

CHAPTER 6. ADAPTIVE DISCRETE NEWTON

the sensitivity study of the nonlinear behaviour of the Power law models w.r.t. the step-size parameter χ , the mesh width h and the strength of the nonlinearity suggests an adaptive choice [49]. Indeed, choosing χ too big leads to the loss of the advantageous quasi-quadratic convergence behaviour of Newton method. On the contrary, if we choose very small value of χ , the divergence occurs due to the numerical instabilities. In order to observe these effects, a study is carried out for the Bingham fluid flow in a channel configuration presented in Table [6.1].

Table 6.1: **Bingham flow in a channel:** Number of Newton iterations for different step-size χ and the nonlinear tolerance for regularization-free Bingham, where the yield stress τ_s is set to 0.25.

$\downarrow \chi/\text{Tol} \rightarrow$	10^{-5}	10^{-6}	10^{-7}	10^{-8}
10^{-2}	13	16	19	22
10^{-3}	13	14	14	16
10^{-4}	14	14	15	diverge
10^{-5}	15	15	oscillate	oscillate
10^{-6}	15	oscillate	oscillate	diverge
10^{-7}	16	diverge	oscillate	diverge
10^{-8}	17	37	diverge	diverge

The results strongly agrees with the suggestion of not choosing too big or too small value of parameter χ . These results lead to the idea of choosing the suitable step-size χ adaptively during the approximations. Therefore, a test is performed for the regularization-free Bingham by changing the step size manually after achieving a certain reduction in the residual $\mathcal{R}(\mathcal{U}^n)$, shown in Fig. 6.1, where two different constant step sizes χ_{c_1} and χ_{c_2} are considered. Initially, the big step-size χ_{c_1} is given and after obtaining a certain reduction in the residual, the step-size is reduced to the smaller value i.e. χ_{c_2} . The implemented idea of changing the step-size between the iterations produced remarkable results as one can see that the convergence was faster after the value of the step-size χ was changed to χ_{c_2} .

However, to implement this strategy in a smart way, such that the choice of χ depends on the residual reduction automatically and removes the numerical instabilities, we allow a process which chooses bigger step-size in the start and changes afterwards between the nonlinear iterations. The ratio of the residuum's norm can be used for the choice of the step-size as a step function and to relate this ratio continuously to the successive nonlinear reduction, we use a characteristic function introduced in [83] or the slightly modified one introduced in [84]

$$f(r_n) = 0.2 + \frac{4.0}{0.7 + \exp(1.5r_n)} \quad (6.2)$$

6.2. NUMERICAL RESULTS

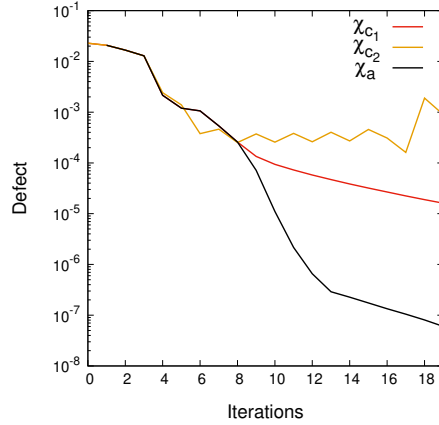


Figure 6.1: **Nonlinear convergence w.r.t. χ for the adaptive discrete Newton method:** The norm of the residual versus number of iterations w.r.t. constant χ strategy (χ_{c_1}, χ_{c_2}) and the adaptive strategy (χ_a) at refinement level $L=2$ ($h_x = 1/4, h_y = 1/12$).

where

$$r_n = \frac{\|\mathcal{R}(U^n)\|}{\|\mathcal{R}(U^{n-1})\|} \quad (6.3)$$

Doing so, the new strategy uses this function to adapt the step-size as follows:

$$\chi_{n+1} = f^{-1}(r_n)\chi_n \quad (6.4)$$

Hence, to test the efficiency and robustness of the new adaptive discrete Newton method, the numerical studies are carried out for four different prototypical configurations (channel flow, lid driven cavity, flow around cylinder and flow in a square reservoir) in the next sections.

6.2 Numerical Results

6.2.1 Bingham Fluid Flow in a Channel

The two dimensional channel is considered as a domain consisting of two parallel plates with h length apart and long, shown in Fig. 5.1. The problem is solved under the assumption of Dirichlet boundary conditions on the domain ($\bar{\Omega} =$

CHAPTER 6. ADAPTIVE DISCRETE NEWTON

$[0, h]^2$) boundaries, where the analytical velocity profile for the x-component is:

$$u_1 = \begin{cases} \frac{1}{8} [(h - 2\tau_s)^2 - (h - 2\tau_s - 2y)^2] & 0 \leq y < \frac{h}{2} - \tau_s \\ \frac{1}{8} (h - 2\tau_s)^2 & \frac{h}{2} - \tau_s \leq y \leq \frac{h}{2} + \tau_s \\ \frac{1}{8} [(h - 2\tau_s)^2 - (2y - 2\tau_s - h)^2] & \frac{h}{2} + \tau_s < y \leq h \end{cases} \quad (6.5)$$

with $u_2 = 0$ and $p = -x + c$ [37, 81]. The viscosity of the fluid is set to be $\eta = 1$, the body force is $\mathbf{f} = 0$ and $h = 1$ is considered. After the implementation of the new adaptive discrete Newton strategy, a test (setting the value of $\tau_s = 0.23$) is performed to investigate the behaviour of the adaptive against constant step-size strategy. Fig. 6.2 (a,c) clearly describes the efficient performance of the newly adaptive step-size because the tolerance criteria is achieved in less than 10 iterations as compared to the classical Newton, which converges in approximately 70 and 50 iterations for refinement levels $L=2$ and $L=3$, respectively. This implies a remarkable faster convergence rate of the adaptive discrete Newton. Moreover, the relative change of χ_a is presented in Fig. 6.2 (b,d).

Afterwards, the yield stress threshold value τ_s is slightly increased to $\tau_s = 0.25$ and the same test is performed. Again, the χ_a shows the faster convergence rate than the χ_c as it achieves the convergence in less than 10 iterations, shown in the Fig. 6.3.

The basic idea behind this strategy is to relax the step-size by setting a big χ at the start and when the residual norm reduces then the step-size χ gets smaller accordingly. On the contrary, if we choose smaller χ at the start, what will happen? In order to investigate this point, a test is performed by setting the two different values of initial adaptive step-size i.e. $\chi_{a_1} = 10^{-1}$ and $\chi_{a_2} = 10^{-4}$, respectively (the yield stress value is set to $\tau_s = 0.25$). It can be clearly seen in Fig. 6.4, when the initial step-size is chosen smaller ($\chi_{a_2} = 10^{-4}$), the solver first oscillates and then faces slow convergence. On the other hand, when the initial step size is chosen bigger ($\chi_{a_2} = 10^{-1}$), the solver converges very fast, which concludes that initial step-size should be big. Furthermore, the lower bound must be according to the machine precision i.e. 10^{-8} .

Moreover, a similar test is carried out for the yield stress $\tau_s = 0.23$ for two initial step-size i.e. $\chi_{a_1} = 10^{-1}$ and $\chi_{a_2} = 10^{-6}$, respectively. As expected, the χ_{a_2} again showed oscillatory behaviour and also the number of nonlinear iterations increases to meet the convergence criteria, shown in Fig. 6.5 (b), which strengthens our already drawn conclusion. These tests are performed for regularization-free Bingham using the three-field formulation.

6.2. NUMERICAL RESULTS

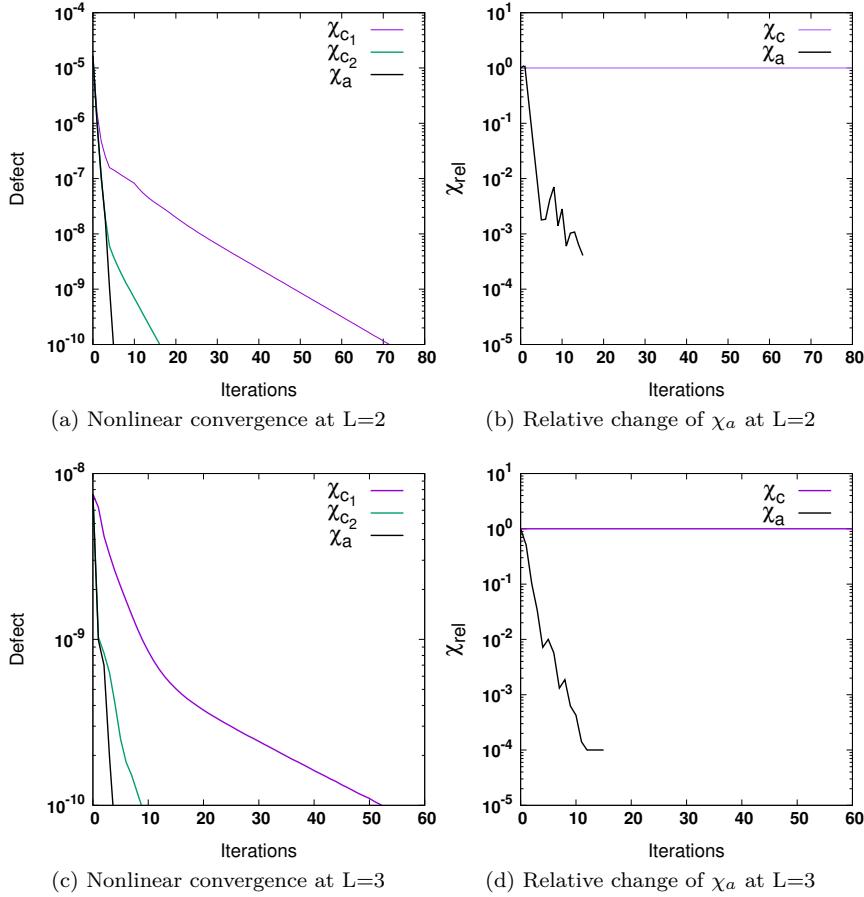


Figure 6.2: **Nonlinear convergence and relative change of χ for the adaptive discrete Newton method:** The norm of the residual versus number of iterations w.r.t. constant χ strategy ($\chi_{c_1} = 10^{-1}, \chi_{c_2} = 10^{-4}$) and the adaptive strategy ($\chi_a = \chi_a^n / \chi_a^0$) at refinement level L=2 (top) ($h_x = 1/4, h_y = 1/12$) and L=3 (bottom) ($h_x = 1/8, h_y = 1/24$) with $\tau_s = 0.23$.

CHAPTER 6. ADAPTIVE DISCRETE NEWTON

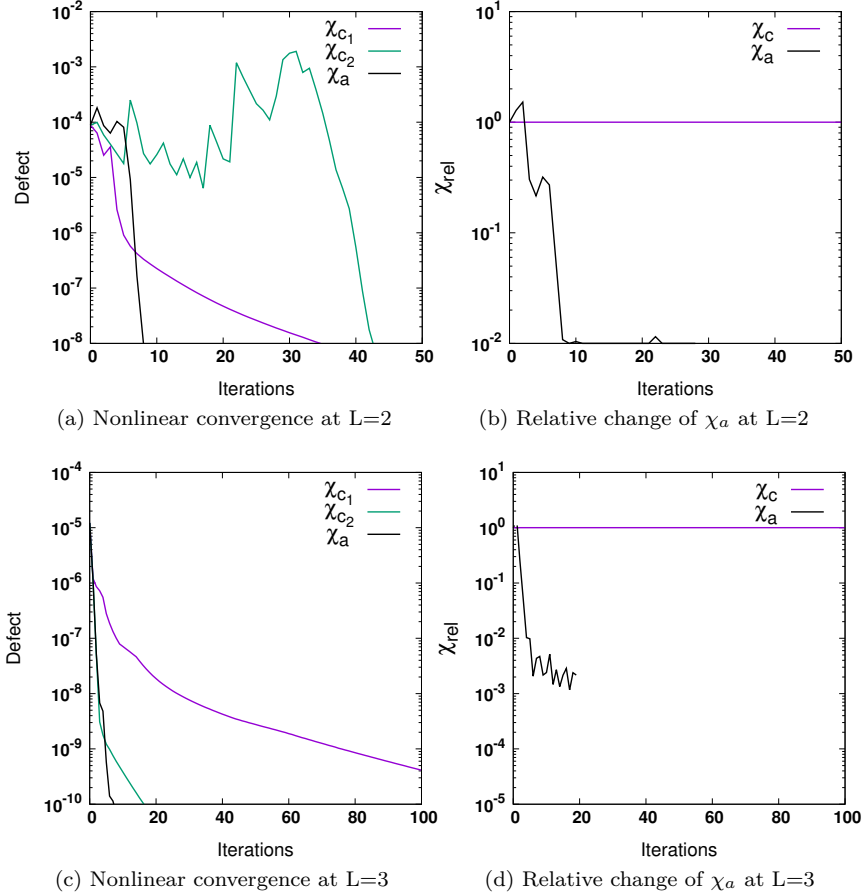


Figure 6.3: **Nonlinear convergence and relative change of χ for adaptive Newton method:** The norm of the residual versus number of iterations w.r.t. constant χ strategy ($\chi_{c_1} = 10^{-1}, \chi_{c_2} = 10^{-4}$) and the adaptive strategy ($\chi_a = \chi_a^n / \chi_a^0$) at refinement level L=2 (top) ($h_x = 1/4, h_y = 1/12$) and L=3 (bottom) ($h_x = 1/8, h_y = 1/24$) with $\tau_s=0.25$.

6.2. NUMERICAL RESULTS

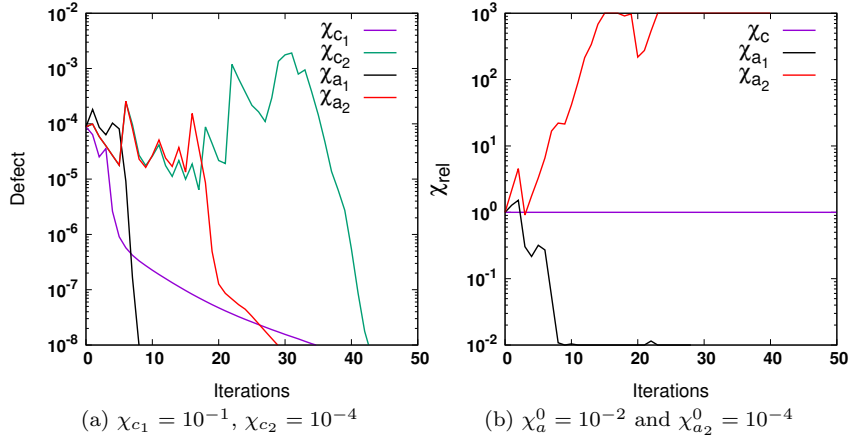


Figure 6.4: **Non-linear convergence w.r.t χ for the adaptive discrete Newton method:** The norm of the residual versus number of iterations w.r.t two strategies (constant and adaptive) at refinement level L=2 (a,b) ($h_x = 1/4$, $h_y = 1/12$) with $\tau_s = 0.25$.

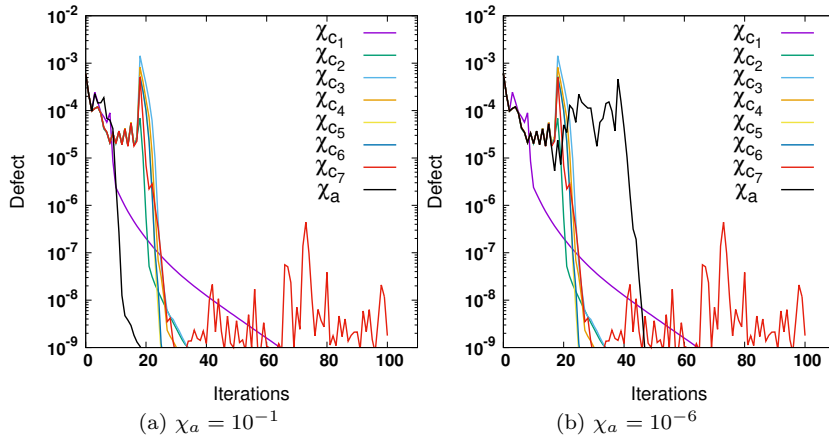


Figure 6.5: **Non-linear convergence w.r.t χ for the adaptive discrete Newton method:** The norm of the residual versus number of iterations w.r.t two strategies (constant and adaptive) at refinement level L=2 (a,b) ($h_x = 1/4$, $h_y = 1/12$) with $\tau_s = 0.23$.

CHAPTER 6. ADAPTIVE DISCRETE NEWTON

Extending the numerical tests, a comparison study is carried out between the new adaptive discrete Newton and the classical Newton for the two-field formulation. Applying both methods, the number of nonlinear iterations is presented in Table [6.2]. For the coarse refinement level ($L=2$ in the present case), starting with the zero solution as an initial guess, we perform Newton iterations until the tolerance is achieved. However, the next refinement level takes the solution from the previous refinement level as an initial solution. For the first test, we choose the yield stress value to be $\tau_s = 0.23$ because this value is aligned as interface with the coarse mesh. It is observed that the two-field formulation along with the classical Newton method faces difficulties in convergence, when the regularization parameter $\epsilon \rightarrow 0$. On the other hand, the adaptive discrete Newton solver is able to converge even for very small values of ϵ , exhibiting the advantages of our newly developed solver. Moreover, it shows a good speed of convergence for all the cases of regularized Bingham fluid.

Similarly, for testing the efficiency of the three-field formulation for the regularization-free Bingham problem, a numerical study is carried out for both of the Newton strategies. The efficiency of the three-field formulation and the robustness of the adaptive strategy for the discrete Newton is showcased successfully in Table 6.3.

Table 6.2: **Bingham flow in a channel:** Comparison of the Newton and the adaptive discrete Newton iterations for the two-field formulation at different mesh refinement levels L and regularization parameter ϵ , yield stress $\tau_s = 0.23$.

↓ L/ϵ →	Newton		Adaptive Newton				
	10^{-1}	10^{-2}	10^{-1}	10^{-2}	10^{-3}	10^{-4}	10^{-5}
3	2	3	4	4	5	5	9
4	2	3	4	4	6	5	9
5	2	3	3	5	5	4	7
6	2	3	3	5	5	4	7

6.2. NUMERICAL RESULTS

Table 6.3: **Bingham flow in a channel:** Comparison of the Newton and the adaptive discrete Newton iterations for the three-field formulation at different mesh refinement levels L and regularization parameter ϵ , yield stress $\tau_s = 0.23$.

$\downarrow L/\epsilon \rightarrow$	10^{-1}	10^{-2}	10^{-3}	10^{-4}	10^{-5}	0
Newton						
2	5	17	61	100	53	23
3	2	3	4	6	9	1
4	2	3	4	8	9	1
5	1	2	3	9	5	2
Adaptive Newton						
2	5	14	21	26	36	16
3	2	2	2	5	1	2
4	2	2	2	4	2	2
5	1	1	1	1	3	1

Furthermore, to highlight the efficiency and robustness of our newly developed solver, a comparison study for four different yield stress value τ_s i.e. 0.23, 0.3, 0.35, 0.4 is carried out, presented in Fig. 6.6 and 6.7 for mesh refinement levels $L=2$ and $L=3$, respectively. All of these tests are carried out for the regularization-free ($\epsilon = 0$) Bingham case, for seven different constant step-sizes, from biggest to smallest i.e. $\chi_{c_1} = 10^{-1}, \chi_{c_2} = 10^{-2}, \chi_{c_3} = 10^{-3}, \chi_{c_4} = 10^{-4}, \chi_{c_5} = 10^{-5}, \chi_{c_6} = 10^{-6}$ and $\chi_{c_7} = 10^{-7}$. One can notice that in each case of χ_c , the solver either converges very slowly or it starts to oscillate. On the other hand, χ_a is very fast to meet the convergence criteria because initially χ_a is relaxed and once the solution enters the radius of convergence, then the χ_a dynamically changes to achieve the accuracy of the solution. The adaptive discrete Newton solver exhibits the remarkable performance for every τ_s , even for the hardest case (when $\tau_s = 0.4$), where the plug zone covers a very big area in the centre of the channel and the situation becomes very difficult for the fluid to flow.

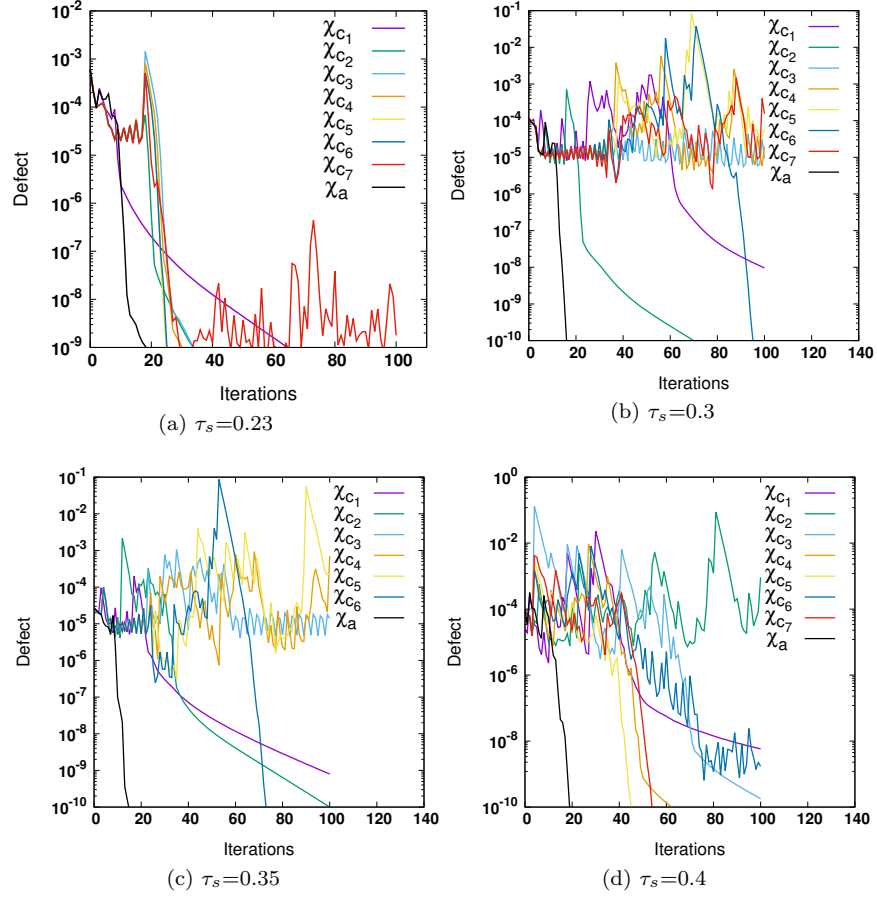


Figure 6.6: **Nonlinear convergence w.r.t. χ for the adaptive discrete Newton method:** The norm of the residual versus number of iterations w.r.t. two strategies (constant (set as $\chi_{c1} = 10^{-1}, \chi_{c2} = 10^{-2}, \dots, \chi_{c7} = 10^{-7}$) and adaptive (χ_a)) at refinement level $L=2$ ($h_x = 1/4, h_y = 1/12$) for $\tau_s = 0.23, 0.3, 0.35, 0.4$.

6.2. NUMERICAL RESULTS

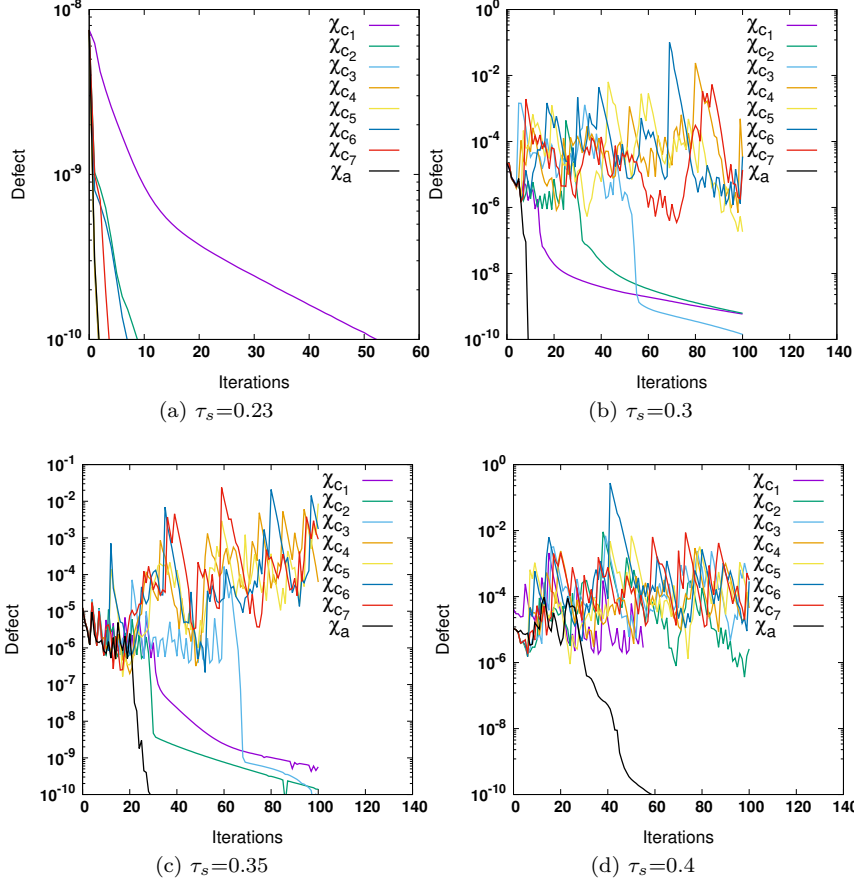


Figure 6.7: **Nonlinear convergence w.r.t. χ for the adaptive discrete Newton method:** The norm of the residual versus number of iterations w.r.t. two strategies (constant (set as $\chi_{c_1} = 10^{-1}, \chi_{c_2} = 10^{-2}, \dots, \chi_{c_7} = 10^{-7}$) and adaptive (χ_a)) at refinement level $L=3$ ($h_x = 1/8, h_y = 1/24$) for $\tau_s = 0.23, 0.3, 0.35, 0.4$.

6.2.2 Lid Driven Cavity

The numerical simulation of Bingham fluid flow for the lid-driven square cavity benchmark is performed for the system of equations (2.13). The geometry consists of a unit square domain $\bar{\Omega} = [0, 1]^2$. Dirichlet boundary conditions are imposed for $u|_{y=1} = (1, 0)^T$ and $u = 0$ everywhere else. The viscosity of the fluid is set to be $\eta = 1$. The geometrical configuration is shown in Fig. 6.8.

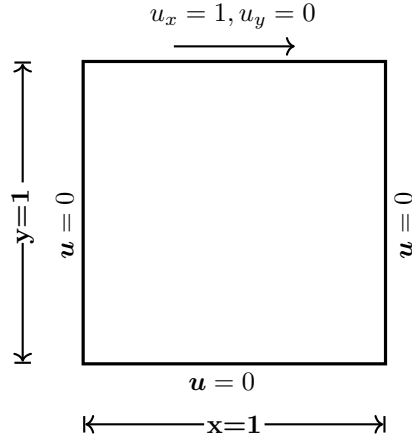


Figure 6.8: Configuration for the lid driven cavity

In the first step, a validation study with the results of Aposporidis et al. [1] for the two-field formulation is carried out, applying both Newton and the adaptive discrete Newton solver, where the yield stress value is set to $\tau_s = 2.0$, shown in Table [6.4]. Looking at the nonlinear iterations in this table, one can clearly observe that the Newton solver is faster than the Picard’s iterative solver (used in the reference study) and the adaptive discrete Newton is the fastest among all, for both values of regularization parameter (ϵ).

Table 6.4: **Lid driven cavity:** Validation of the Newton and the adaptive discrete Newton iterations with Aposporidis et al. [1], for the two-field formulation at different mesh refinement levels L , with the yield stress $\tau_s = 2.0$.

ϵ	L	Aposporidis et al. [1]	Newton	Adaptive Newton
10^{-1}	4	22	10	4
	5	99	8	4
	6	213	5	4
10^{-2}	4	49	8	4
	5	173	8	4
	6	-	5	4

In the second step, a validation study with the reference results [1] for the three-field formulation is carried out, applying both Newton and the adaptive discrete Newton solver, specifically for the extreme case i.e. regularization-free Bingham, where the yield stress value is set to $\tau_s = 2.0$, shown in Table [6.5]. Again, the nonlinear iterations of the Newton solver is faster than the Picard’s iterative solver (used in the reference study) and the adaptive discrete Newton is the fastest among all.

6.2. NUMERICAL RESULTS

Table 6.5: **Lid-driven cavity:** Validation of the Newton and the adaptive discrete Newton iterations with Aposporidis et al. [1] for regularization-free ($\epsilon = 0$) Bingham, for three-field formulation at different mesh refinement levels L, with the yield stress $\tau_s = 2.0$.

L	Aposporidis et al. [1]	Newton	Adaptive Newton
4	21	13	5
5	23	21	5
6	15	18	6

The accuracy of the solution can be checked in terms of the prediction of unyielded zones in the domain. Therefore, a validation of the unyielded zones is presented in Fig. 6.9, which shows a good agreement with the reference results [1] and [85]. Basically, these zones present the image of the dead regions, where the velocity is either constant or zero and no deformation occurs in the fluid.

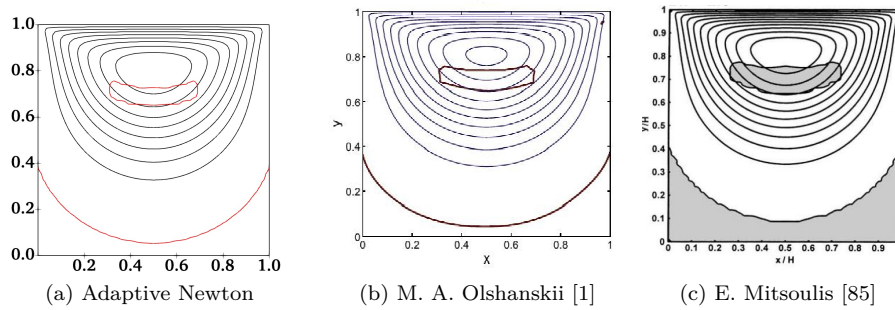


Figure 6.9: **Lid driven cavity:** The superposition of unyielded zones on the streamline contours for the regularization-free ($\epsilon = 0$) Bingham, for the three-field formulation at mesh refinement levels L=6 ($h=1/64$), where the yield stress is set to $\tau_s = 2.0$.

In order to investigate the effects of the regularization parameter ϵ on the development of unyielded zones, a numerical study is performed with the yield stress value $\tau_s = 2.0$, given in the Fig 6.10. It can be concluded from the results that for the accurate prediction of these zones, the regularization parameter should be small enough ($\epsilon \rightarrow 0$).

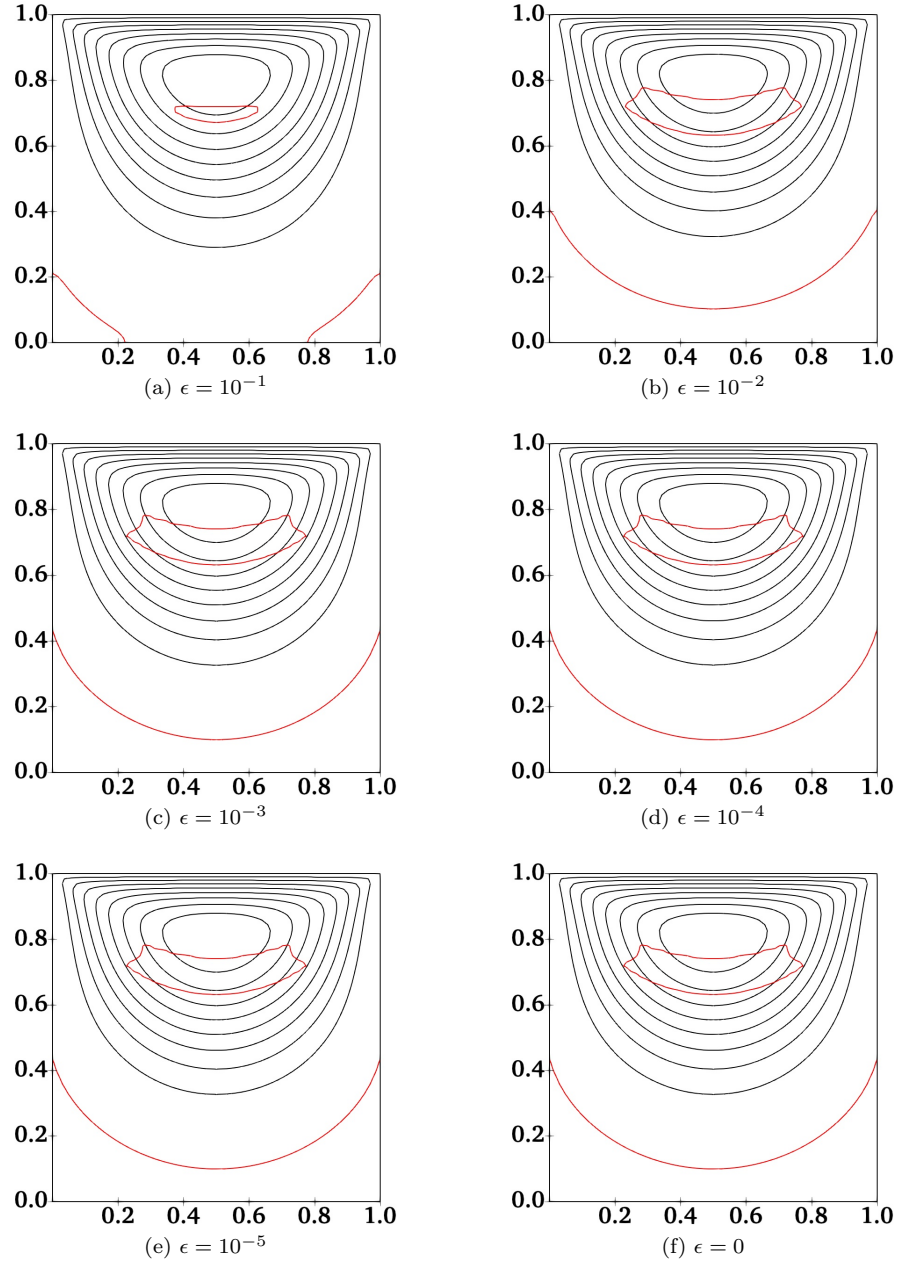


Figure 6.10: **Unyielded zones:** The superposition of the contour of the unyielded zones on the streamline contours in the lid driven cavity computed for regularization-free ($\epsilon = 0$) and regularized ($\epsilon = 10^{-1}$ to 10^{-5}) Bingham with the yield stress value $\tau_s = 2.0$ at refinement level $L=6$ ($h = 1/64$).

6.2. NUMERICAL RESULTS

Moreover, the corresponding nonlinear iterations of Newton and the adaptive discrete Newton solver are presented in Table [6.6]. Again, the performance of the adaptive Newton is very impressive, specially in case of regularization-free Bingham (which is a very complex case for the lid driven cavity benchmark).

Table 6.6: **Lid driven cavity:** Comparison of the Newton and the adaptive discrete Newton iterations for three-field formulation at different mesh refinement levels L and regularization parameter ϵ , with the yield stress $\tau_s = 2.0$.

$\downarrow L/\epsilon \rightarrow$	10^{-1}	10^{-2}	10^{-3}	10^{-4}	10^{-5}	0
Newton						
3	7	12	13	13	13	13
4	3	17	21	21	21	21
5	4	11	19	22	7	18
Adaptive Newton						
3	3	4	4	5	4	5
4	3	4	4	5	6	5
5	3	4	5	7	7	6

In the next step, the effects of the yield stress value on the growth of the unyielded zones are investigated by increasing the τ_s value from 2.0 to 5.0, presented in Fig. 6.11, where the region of the dead zones grows, when the τ_s increases to 5.0. Table [6.7] presents the corresponding comparison study for both Newton and adaptive Newton solver. The results are according to the expectations, the adaptive Newton solver is robust and efficient in all cases. Note that the classical Newton faces difficulties specially on higher mesh levels for small values of ϵ . Fig. 6.12 illustrates the efficiency of the adaptive Newton solver for both values of τ_s for the regularization-free Bingham, as it converges in very less number of iterations. On the other hand, the constant step-size either oscillates or converges very slowly.

In order to test the limit of the complexity handled by the adaptive discrete Newton, in terms of the threshold value τ_s of Bingham fluid. The forthcoming tests are carried out by increasing the value of τ_s , given in Table [6.8]. The adaptive Newton shows faster convergence with significantly less number of nonlinear iterations. Furthermore, Table [6.9] summarizes all the test carried out for the regularization-free Bingham in the lid driven cavity for all values of yield stress, starting from moderate (2.0) to very high (50.0). The effect of increasing the τ_s on the growth of dead zones in the cavity can be seen very clearly in Fig. 6.13, where the unyielded zones grows significantly (which increases the no flow area (shaded in black)). This implies that the adaptive

CHAPTER 6. ADAPTIVE DISCRETE NEWTON

Newton solver is not only efficient but also solves accurately by predicting the accurate unyielded zones.

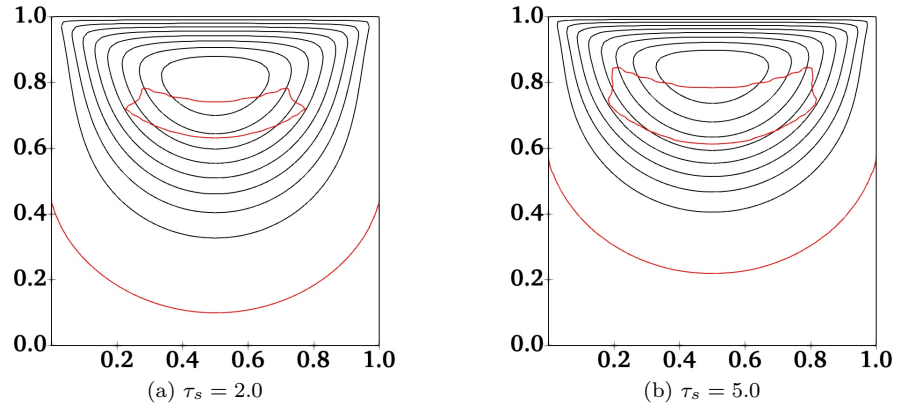


Figure 6.11: **Unyielded zones:** The superposition of the contour of the unyielded zones on the streamline contours in the lid driven cavity computed for regularization-free ($\epsilon = 0$) Bingham with the yield stress value $\tau_s = 2.0$ and $\tau_s = 5.0$ at refinement level $L=6$ ($h = 1/64$).

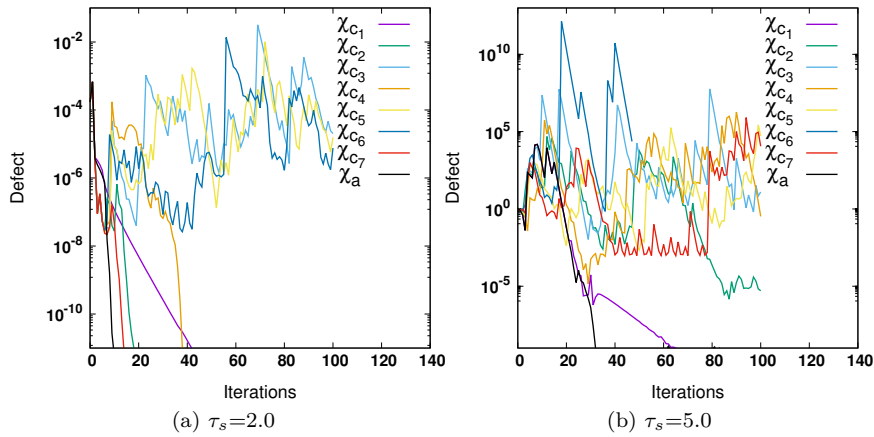


Figure 6.12: **Nonlinear convergence w.r.t χ for the adaptive discrete Newton method:** The norm of the residual versus number of iterations w.r.t. two strategies (constant and adaptive) at refinement level $L=4$ ($h_x = 1/16, h_y = 1/16$) with the constant χ strategy (set as $\chi_{c_1} = 10^{-1}, \chi_{c_2} = 10^{-2}, \dots, \chi_{c_7} = 10^{-7}$) and the adaptive strategy (χ_a) for τ_s 2.0 and 5.0.

6.2. NUMERICAL RESULTS

Table 6.7: **Lid driven cavity:** Comparison of the Newton and the adaptive discrete Newton iterations for the three-field formulation with yield stress $\tau_s = 5.0$ at different refinement levels L and regularization parameters including regularization-free Bingham.

$\downarrow L/\epsilon \rightarrow$	10^{-1}	10^{-2}	10^{-3}	10^{-4}	10^{-5}	0
Newton						
3	10	21	21	21	21	5
4	11	28	31	31	31	-
5	4	27	-	-	-	-
Adaptive Newton						
3	4	4	5	5	5	5
4	3	4	5	6	4	5
5	3	3	3	6	6	6

Table 6.8: **Lid driven cavity:** The adaptive discrete Newton iterations for the three-field formulation with yield stress values $\tau_s = 7.5, 10, 15$ at different refinement levels L and regularization parameters including regularization-free Bingham.

$\downarrow \tau_s / \epsilon \rightarrow$	L	10^{-1}	10^{-2}	10^{-3}	10^{-4}	10^{-5}	0
7.5	3	14	29	37	40	4	2
	4	4	5	6	6	6	6
	5	4	4	6	4	4	2
10	3	13	22	31	100	101	101
	4	4	4	4	6	12	4
	5	3	4	5	7	9	3
15	3	20	29	54	65	78	79
	4	5	5	5	5	5	5
	5	4	4	7	2	2	5

Table 6.9: **Lid driven cavity:** Summary of the adaptive discrete Newton iterations for the three-field formulation, for different yield stress values at different refinement levels L , for regularization-free ($\epsilon = 0$) Bingham.

$\downarrow L/\tau_s \rightarrow$	2	5	7.5	10	15	20	40	50
3	5	5	2	101	79	3	8	18
4	5	6	6	4	5	5	6	7
5	6	6	2	3	5	5	6	9

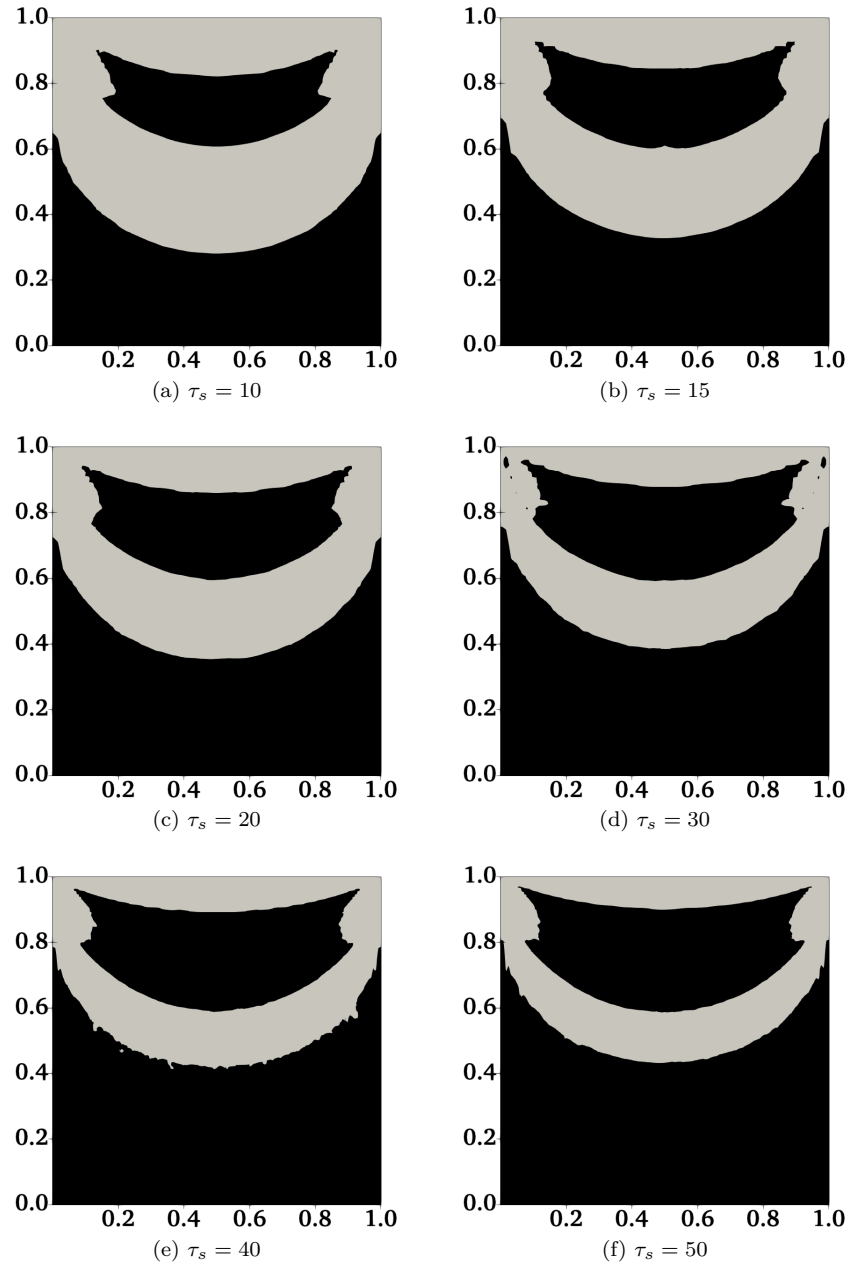


Figure 6.13: **Unyielded zones:** The unyielded zones of the regularization-free ($\epsilon = 0$) Bingham for different yield stress values $\tau_s = 10, 15, 20, 30, 40, 50$ at refinement level $L=5$ ($h = 1/32$).

6.2. NUMERICAL RESULTS

6.2.3 Flow Around Cylinder

This DFG 2-dimensional benchmark [79] analyse the attributes of the flow around an obstacle in a rectangular channel, where a cylinder of radius $r = 0.05$ is placed with the centre at $(0.2, 0.2)$ in a rectangular channel of length 2.2, the upper and lower walls are 0.41 length apart. The geometrical configuration and coarse mesh are shown in Fig. 4.1 and 4.2. The fluid density (ρ) and kinematic viscosity (η) are set to 1 and 0.001, respectively. The fluid is characterised by the stationary three-field Navier-Stokes equations:

$$\begin{cases} \|\mathbf{D}(\mathbf{u})\|_\epsilon \boldsymbol{\sigma} - \mathbf{D}(\mathbf{u}) = 0 & \text{in } \Omega \\ -\nabla \cdot (2\eta\mathbf{D}(\mathbf{u}) + \tau_s\boldsymbol{\sigma}) + \mathbf{u} \cdot \nabla\mathbf{u} + \nabla p = 0 & \text{in } \Omega \\ \nabla \cdot \mathbf{u} = 0 & \text{in } \Omega \end{cases} \quad (6.6)$$

where \mathbf{u} is the velocity and p is the pressure. No-slip boundary conditions are set on upper, lower walls and also on cylinder surface. Parabolic velocity profile is given at the inlet as:

$$u_x(y) = \left(\frac{4.0U_{\max}y(0.41 - y)}{(0.41)^2}, 0 \right)$$

with maximum velocity $U_{\max} = 0.3$. The outflow boundary condition is set as do nothing. The average velocity for $U_{\max} = 0.3$ is $U_{\text{avg}} = 0.2$. According to the characteristic length of the cylinder i.e. $c_l = 0.1$, the Reynolds number is calculated as:

$$Re = \frac{U_{\text{avg}}c_l}{\eta} = 20$$

For the validation of Newtonian flow benchmark, τ_s is substituted as 0 in the system of equations (6.6), which reduces the system into the classical Navier-Stokes equations. The corresponding numerical results (in terms of drag/lift values) strongly agree with the Damanik [62], shown in Table [6.10].

Table 6.10: **Flow around cylinder Drag/Lift:** Comparison with Damanik [62], where NL denotes the number of adaptive discrete Newton iterations, LL denotes the average number of multigrid iterations.

L	Drag/Lift	NL/LL	Drag/Lift [62]	NL/LL [62]
1	5.5550/0.009498	9/1	5.5550/0.009498	9/2
2	5.5722/0.010601	6/1	5.5722/0.010601	9/2
3	5.5776/0.010616	5/1	5.5776/0.010616	9/1
4	5.5791/0.010618	4/1	5.5790/0.010618	8/1

Afterwards, in order to get the viscoplastic effects in the flow, the value of the yield stress is increased from 0 to 0.002, 0.02 and 0.2, respectively. The corresponding numerical results for drag and lift coefficients at different mesh

CHAPTER 6. ADAPTIVE DISCRETE NEWTON

refinement levels are presented in Table 6.11, where "NL" denotes the nonlinear iterations of adaptive discrete Newton. The effects of increasing the yield stress value can be observed in Fig. 6.14, where the velocity profile is drawn through $x = 1.5$. Note that the velocity magnitude changes its behaviour from parabolic profile to flat profile, which reflects the rigid zone where the fluid moves with constant speed. Therefore, when the τ_s increases the flat region grows accordingly.

Table 6.11: **Bingham stationary flow around cylinder:** Adaptive discrete Newton iterations for the regularization-free ($\epsilon = 0$) Bingham fluid at different mesh refinement levels L with different yield stress values (τ_s).

τ_s	L	Drag/Lift	NL
0.002	0	6.1228/0.014789	7
	1	6.2469/0.026615	10
	2	6.2679/0.032125	11
0.02	0	12.7121/0.072606	13
	1	13.4006/0.084327	13
	2	13.5184/0.081366	16
0.2	0	78.7969/0.418760280	7
	1	83.5063/-0.050840764	14
	2	87.4437/-0.151120580	16

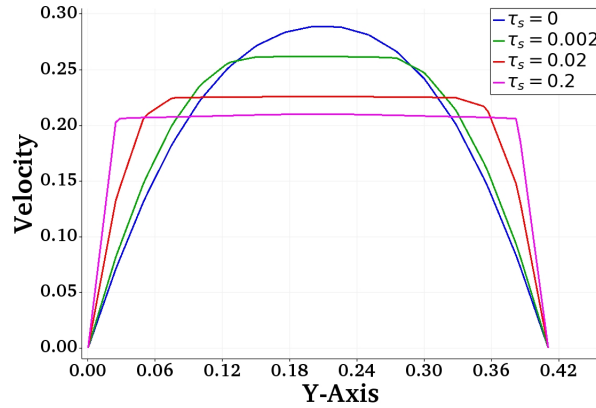


Figure 6.14: **Bingham stationary flow around cylinder:** The velocity profile of regularized-free Bingham ($\epsilon = 0$) through $x = 1.5$ at refinement level $L = 2$, for different yield stress values.

Fig. 6.15 presents the visualization of the velocity magnitude and distribution of the pressure in the channel. It can be noticed that the maximum velocity decreases, when the τ_s increases because the big part of the fluid in the middle

6.2. NUMERICAL RESULTS

of the channel behaves as solid and the maximum pressure increases. Moreover, the visualization of $\|\mathbf{D}(\mathbf{u})\|$ and $\|\boldsymbol{\sigma}\|$ is presented in Fig. 6.16, where the region ($\|\boldsymbol{\sigma}\| < 1$) of auxiliary stress tensor grows with the increasing τ_s . This region indicates the rigid regime of the Bingham fluid flow in the channel.

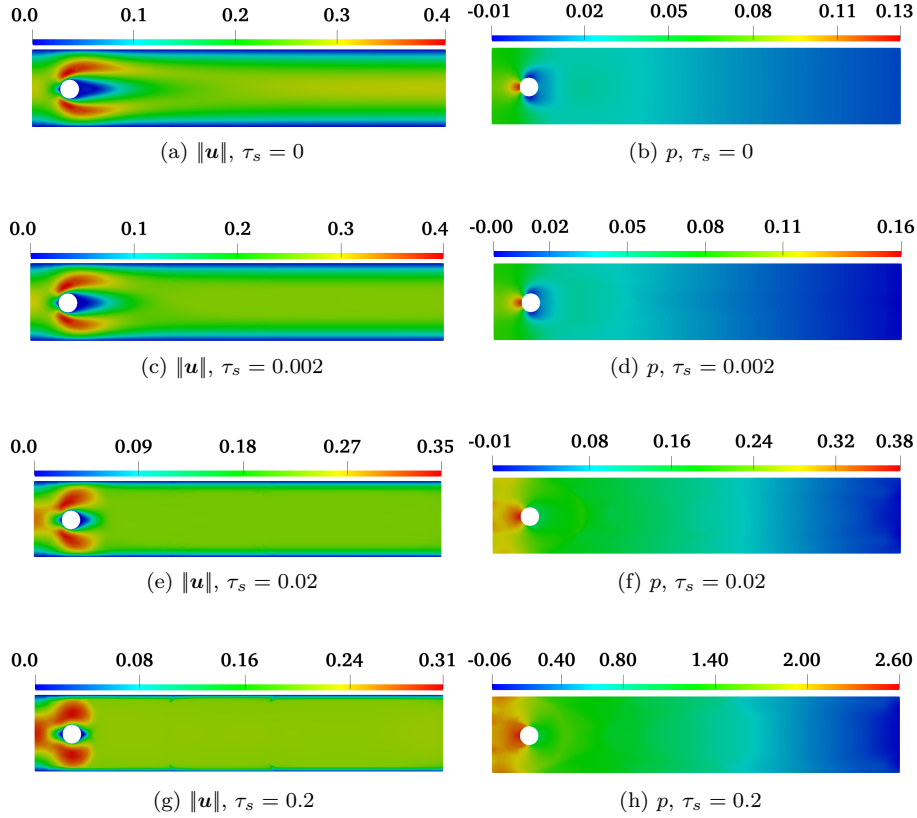


Figure 6.15: **Bingham stationary flow around cylinder:** The visualization of the velocity magnitude and pressure distribution for regularization-free Bingham ($\epsilon = 0$) at refinement level $L = 2$ for different yield stress values.

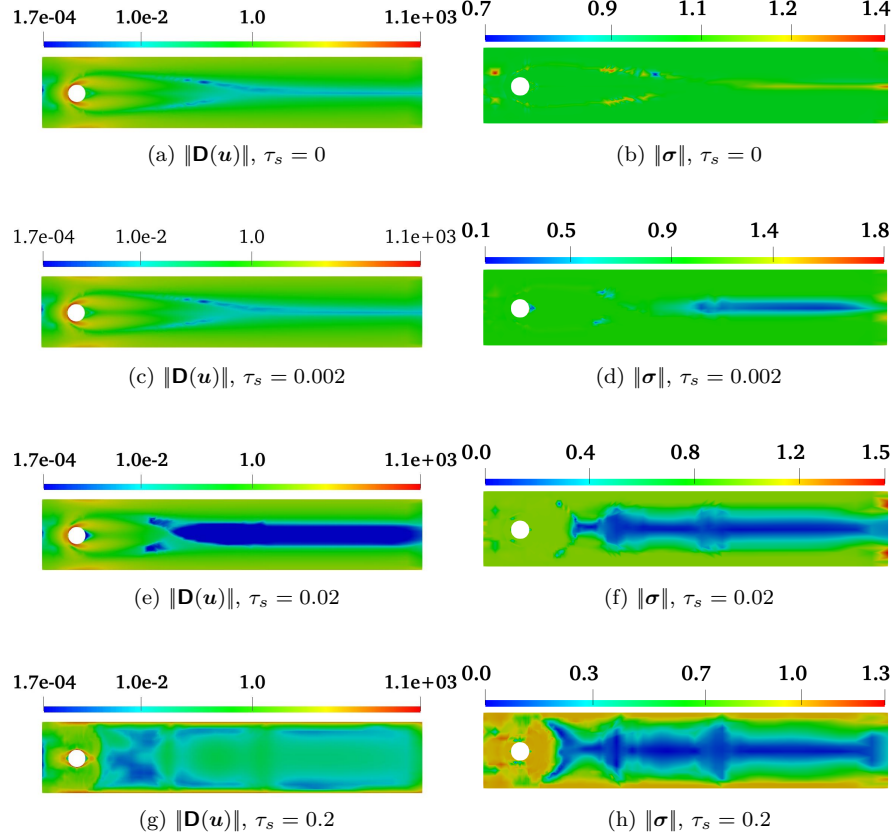


Figure 6.16: **Bingham stationary flow around cylinder:** The visualization of $\|\mathbf{D}(\mathbf{u})\|$ and $\|\boldsymbol{\sigma}\|$ for regularization-free ($\epsilon = 0$) Bingham at refinement level $L = 2$ for different yield stress values.

6.2.4 Rotational Bingham Flow in a Square Reservoir

To test the accuracy of the three-field formulation of Bingham fluid flow along with the adaptive discrete Newton solver, a numerical study of the rotational Bingham flow in a square reservoir benchmark [86, 87] is carried out, specifically for the regularization-free ($\epsilon = 0$) case. This configuration should produce the true viscoplastic solution of the problem.

The benchmark is validated with a recent numerical results of Sergio et al. [87]. The configuration settings includes a wall driven force \mathbf{f} as:

$$\mathbf{f}(x_1, x_2) = 300 (x_2 - 0.5, 0.5 - x_1)$$

over the domain $\Omega = [0, 1]^2$ with the yield stress value $\tau_s = 14.5$. In this

6.2. NUMERICAL RESULTS

numerical experiment, the flow behaviour is analysed with the motion on the boundaries. Fig. 6.17 presents the validation of the results in terms of the velocity field and the plug zones prediction, respectively. A central solid rigid zone is expected as a true solution of the Bingham viscoplastic fluid in this application. Our results are in very good agreement for the velocity field Fig. 6.17 (a) as well as for the calculation of the unyielded zones Fig. 6.17 (b). This assures the accuracy and the efficiency of the three-field Bingham formulation along with our newly developed adaptive discrete Newton solver.

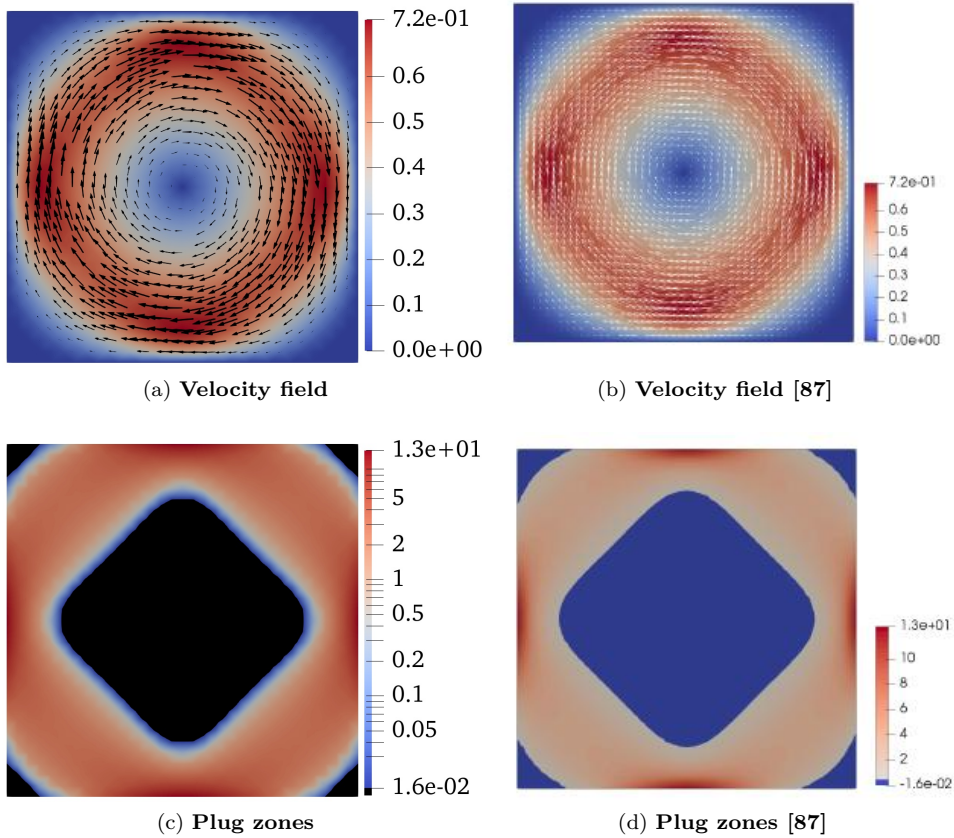


Figure 6.17: **Bingham flow in a square reservoir:** Velocity field and the plug zones of regularization-free ($\epsilon = 0$) Bingham at mesh refinement level $L = 5$ for yield stress value $\tau_s = 14.5$.

Chapter 7

Conclusions

In this work, a new adaptive discrete Newton method and a regularization-free solver for yield stress fluids is developed. Firstly, by introducing a new auxiliary stress in a three-field formulation. This formulation is very beneficial because it can robustly solve small regularization parameter (ϵ) as well as regularization-free ($\epsilon = 0$), which is usually a very difficult task for a numerical solver in the case of primitive variable formulation of any viscoplastic fluid. The existence and the uniqueness of the weak form of the regularized problem has been briefly discussed (chapter 2), whereas the uniqueness of the regularization-free Bingham is still an open problem in the theory. The nonlinearity is treated with the discrete Newton method and the resulting saddle-point problem is solved with a monolithic finite element method to simulate the viscoplastic flows. The advantage of this formulation is to achieve a true regularization-free viscoplastic solution, i.e. $\epsilon = 0$, efficiently and accurately. Several numerical experiments are carried out for the benchmark problem "Bingham fluid flow in a channel", where the three-field formulation predicts the unyielded surfaces correctly without effecting the shape of the yield surfaces.

Secondly, a robust and accurate new adaptive discrete Newton method is developed, which evaluates the Jacobian matrix with the divided difference approach and converges faster as compared to the classical Newton. A step function (depending on the reduction of the nonlinear residual) automatically adapt the step-size (χ) value, which is in the denominator of the approximated Jacobian. This step-size has a great role in the performance of any difference method, which is smartly adapted in our new strategy. The robustness and the efficiency of this newly developed adaptive discrete Newton is tested for several flow configurations (Bingham fluid flow in a channel, lid driven cavity, flow around cylinder and rotational Bingham flow in a square reservoir), where comparisons are carried out for the classical and the adaptive discrete Newton. The numerical results illustrates that the number of nonlinear iterations is significantly reduced as compared to the constant step-size strategy (classical Newton). The remark-

CHAPTER 7. CONCLUSIONS

able performance of the adaptive discrete Newton along with the three-field formulation provides an efficient and robust monolithic solver for the Bingham fluid flow problems. Moreover, the adaptive discrete Newton solver is also very useful for other nonlinear problems as it can handle any nonlinearity of the system of equations in a black box manner and produces a remarkable speed of convergence with accurate solution.

Bibliography

- [1] A. Aposporidis, E. Haber, M. Olshanskii, and A. Veneziani, “A mixed formulation of the Bingham fluid flow problem: Analysis and numerical solution,” *Computer Methods in Applied Mechanics and Engineering* **200**, 2434–2446 (2011).
- [2] A. Fatima, S. Turek, A. Ouazzi, and M. A. Afaq, “An Adaptive Discrete Newton Method for Regularization–Free Bingham Model,” Tech. rep., Fakultät für Mathematik, TU Dortmund (2021). *Ergebnisberichte des Instituts für Angewandte Mathematik*, Nummer 635.
- [3] P. Coussot, “Yield stress fluid flows: A review of experimental data,” *Journal of Non-Newtonian Fluid Mechanics* **211**, 31–49 (2014). URL <https://www.sciencedirect.com/science/article/pii/S0377025714000895>.
- [4] H. A. Barnes and K. Walters, “The yield stress myth?” *Rheologica Acta* **24**, 323–326 (1985).
- [5] G. Astarita, “Letter to the Editor: The engineering reality of the yield stress,” *Journal of Rheology* **34**(2), 275–277 (1990). Cited By 88, URL <https://www.scopus.com/inward/record.uri?eid=2-s2.0-84955051287&doi=10.1122%2f1.550142&partnerID=40&md5=3df925123f82a2a45ce35566eadc2bed>.
- [6] A. Maleki, S. Hormozi, A. Roustaei, and I. A. Frigaard, “Macro-size drop encapsulation,” *Journal of Fluid Mechanics* **769**, 482–521 (2015).
- [7] P. Sarmadi, O. Mierka, S. Turek, S. Hormozi, and I. A. Frigaard, “Three dimensional simulation of flow development of triple-layer lubricated pipeline transport,” *Journal of Non-Newtonian Fluid Mechanics* **274**, 104–201 (2019).
- [8] N. Balmforth, I. A. Frigaard, and G. Ovarlez, “Yielding to Stress: Recent Developments in Viscoplastic Fluid Mechanics,” *Annual Review of Fluid Mechanics* **46**, 121–146 (2014).

BIBLIOGRAPHY

- [9] E. C. Bingham, *Fluidity and plasticity*, International chemical series, 1st ed. (McGraw-Hill Book Company, inc., 1922).
- [10] M. R. Hestenes, “Multiplier and gradient methods,” *Journal of Optimization Theory and Applications* **4**, 303–320 (1969).
- [11] R. Huilgol and M. Panizza, “On the determination of the plug flow region in Bingham fluids through the application of variational inequalities,” *Journal of Non-Newtonian Fluid Mechanics* **58**(2), 207–217 (1995). URL <https://www.sciencedirect.com/science/article/pii/S037702579501342S>.
- [12] R. Huilgol and Z. You, “Application of the augmented Lagrangian method to steady pipe flows of Bingham, Casson and Herschel-Bulkley fluids,” *Journal of Non-Newtonian Fluid Mechanics* **128**(2), 126–143 (2005). URL <https://www.sciencedirect.com/science/article/pii/S0377025705000911>.
- [13] P. Saramito and N. Roquet, “An adaptive finite element method for viscoplastic fluid flows in pipes,” *Computer Methods in Applied Mechanics and Engineering* **190**(40), 5391–5412 (2001). URL <https://www.sciencedirect.com/science/article/pii/S004578250100175X>.
- [14] R. Glowinski, “Approximation of a Bingham-Type Elliptic, Variational Inequality,” *Rev Fr Autom Inf Rech Oper* **10**(12), 13–30 (1976). URL <https://www.scopus.com/inward/record.uri?eid=2->.
- [15] R. Glowinski, *Lectures on numerical methods for non-linear variational problems* (Springer Science & Business Media, 2008).
- [16] M. Fortin and R. Glowinski, *Augmented Lagrangian methods : applications to the numerical solution of boundary-value problems* (Elsevier Science Pub. Co., 1983).
- [17] E. Dean, R. Glowinski, and G. Guidoboni, “On the numerical simulation of Bingham visco-plastic flow: Old and new results,” *Journal of Non-Newtonian Fluid Mechanics* **142**, 36–62 (2007).
- [18] M. Bercovier and M. Engelman, “A finite-element method for incompressible non-Newtonian flows,” *Journal of Computational Physics* **36**(3), 313–326 (1980).
- [19] T. C. Papanastasiou, “Flows of Materials with Yield,” *Journal of Rheology* **31**(5), 385–404 (1987).
- [20] N. Roquet and P. Saramito, “An adaptive finite element method for Bingham fluid flows around a cylinder,” *Computer Methods in Applied Mechanics and Engineering* **192**(31), 3317–3341 (2003).

BIBLIOGRAPHY

- [21] I. A. Frigaard and C. Nouar, “On the Usage of Viscosity Regularisation Methods for Visco-Plastic Fluid Flow Computation,” *Journal of Non-Newtonian Fluid Mechanics* **127**, 1–26 (2005).
- [22] A. Fatima, S. Turek, A. Ouazzi, and M. A. Afaq, “An adaptive discrete Newton method for regularization-free Bingham model,” in *Book of Extended Abstracts of the 6th ECCOMAS Young Investigators Conference 7th-9th July 2021, Valencia, Spain*, pp. 180–189 (Editorial Universitat Politècnica de València, Valencia, Spain, 2021).
- [23] M. A. Afaq, S. Turek, A. Ouazzi, and A. Fatima, “Monolithic Newton-Multigrid Solver for Multiphase Flow Problems with Surface Tension,” in *Book of Extended Abstracts of the 6th ECCOMAS Young Investigators Conference 7th-9th July 2021, Valencia, Spain*, pp. 190–199 (Editorial Universitat Politècnica de València, Valencia, Spain, 2021).
- [24] A. Fatima, H. Damanik, S. Turek, R. Wolff, J. Rudloff, M. Lang, T. Hochrein, and M. Bastian, “Mit Simulation zu neuen Materialien,” *Kunststoffe* **09/2021** (2021).
- [25] D. Sandri, “A posteriori estimators for mixed finite element approximations of a fluid obeying the power law,” *Computer Methods in Applied Mechanics and Engineering* **166**, 329–340 (1998).
- [26] A. F. Loula and J. N. C. Guerreiro, “Finite element analysis of nonlinear creeping flows,” *Computer Methods in Applied Mechanics and Engineering* **79**(1), 87–109 (1990). URL <https://www.sciencedirect.com/science/article/pii/0045782590900965>.
- [27] G. Gatica, M. González, and S. Meddahi, “A low-order mixed finite element method for a class of quasi-Newtonian Stokes flows. Part II: A posteriori error analysis,” *Computer Methods in Applied Mechanics and Engineering* **193**, 893–911 (2004).
- [28] D. Bonn and M. M. Denn, “Yield Stress Fluids Slowly Yield to Analysis,” *Science* **324**(5933), 1401–1402 (2009). <https://www.science.org/doi/pdf/10.1126/science.1174217>, URL <https://www.science.org/doi/abs/10.1126/science.1174217>.
- [29] P. Jop, Y. Forterre, and O. Pouliquen, “A constitutive law for dense granular flows,” *Nature* **441**, 727–30 (2006).
- [30] H. Schmitt, “Numerical Simulation of Bingham Fluid Flow Using Prox-Regularization,” *Journal of Optimization Theory and Applications* **106**, 603–626 (2000).
- [31] E. J. Dean and R. Glowinski, “Operator-splitting methods for the simulation of Bingham viscoplastic flow,” *Chinese Annals of Mathematics* **23** (2012).

BIBLIOGRAPHY

- [32] R. Glowinski and P. Le Tallec, *Augmented Lagrangian and Operator-Splitting Methods in Nonlinear Mechanics* (Society for Industrial and Applied Mathematics, 1989).
- [33] B. Dacorogna, R. Glowinski, Y. Kuznetsov, and T.-W. Pan, “On a Conjugate Gradient/Newton/Penalty Method for the Solution of Obstacle Problems. Application to the Solution of an Eikonal System with Dirichlet Boundary Conditions,” (2004).
- [34] M. Allouche, I. A. Frigaard, and G. Sona, “Static wall layers in the displacement of two visco-plastic fluids in a plane channel,” *Journal of Fluid Mechanics* **424**, 243–277 (2000).
- [35] E. O’Donovan and R. Tanner, “Numerical study of the Bingham squeeze film problem,” *Journal of Non-Newtonian Fluid Mechanics* **15**(1), 75–83 (1984).
- [36] K. Bathe, *Computational Fluid and Solid Mechanics* (Elsevier Science, 2001). URL <https://books.google.de/books?id=Id06Z4YMJLMC>.
- [37] J. Hron, J. Málek, J. Stebel, and K. Touska, “A Novel View on Computations of SteadyFlows of Bingham Fluids Using Implicit Constitutive Relations,” (2017).
- [38] A. Mitchell and D. Griffiths, *The Finite Difference Method in Partial Differential Equations* (1980).
- [39] K. Morton and D. Mayers, *Numerical Solution of Partial Differential Equations: An Introduction* (Cambridge University Press, 2005). URL https://books.google.de/books?id=0uf_iQIBFKgC.
- [40] F. Stummel, “Difference methods for linear initial value problems,” in *Numerische Behandlung nichtlinearer Integrodifferential und Differentialgleichungen*, pp. 123–135 (Springer Berlin Heidelberg, Berlin, Heidelberg, 1974).
- [41] R. Herbin and O. Laberge, “Finite volume schemes for elliptic and elliptic-hyperbolic problems on triangular meshes.” *Comp. Meth. Appl. Mech. Engin.* **147**, 85–103 (1997).
- [42] R. J. LeVeque, *Finite Volume Methods for Hyperbolic Problems*, Cambridge Texts in Applied Mathematics (Cambridge University Press, 2002).
- [43] C. Cuvelier, A. Segal, and A. A. Steenhoven, van, *Finite element methods and Navier-Stokes equations*, Mathematics and its applications (Reidel, 1986).
- [44] S. S. Rao, *The Finite Element Method in Engineering (Fourth Edition)*, Fourth Edition (Butterworth-Heinemann, 2005).

BIBLIOGRAPHY

- [45] G. Strang and G. J. Fix, *An analysis of the Finite Element Method* (Prentice Hall, 1973).
- [46] F. Miller, A. Vandome, and M. John, *Divergence Theorem* (VDM Publishing, 2010). URL <https://books.google.de/books?id=TlpNSwAACAAJ>.
- [47] G. W. Collins, *Fundamental Numerical Methods and Data Analysis* (1990).
- [48] R. Burden and J. Faires, *Numerical Analysis* (Cengage Learning, 2010). URL <https://books.google.de/books?id=zXnSxY9G2JgC>.
- [49] J. Hron, A. Ouazzi, and S. Turek, “A computational comparison of two FEM solvers for nonlinear incompressible flow,” in *Lecture Notes in Computational Science and Engineering*, vol. 35, pp. 87–109 (Springer, 2003). New York.
- [50] D. Arnold, D. Boffi, and R. Falk, “Approximation by quadrilateral finite elements,” *Mathematics of computation* **71**(239), 909–922 (2002).
- [51] D. Boffi, F. Brezzi, and M. Fortin, *Finite Elements for the Stokes Problem*, pp. 45–100 (Springer Berlin Heidelberg, Berlin, Heidelberg, 2008). URL https://doi.org/10.1007/978-3-540-78319-0_2.
- [52] R. Rannacher and S. Turek, “Simple nonconforming quadrilateral Stokes element,” *Numerical methods for partial differential equations* **8**(2), 97–111 (1992).
- [53] S. Turek, M. Griebel, D. Keyes, and R. Nieminen, *Efficient Solvers for Incompressible Flow Problems: An Algorithmic and Computational Approache*, Lecture notes in computational science and engineering (Springer-Verlag, 1999). URL https://books.google.de/books?id=bHninqVxO_AC.
- [54] V. Girault and P. A. Raviart, *Finite Element Methods for Navier-Stokes equations*. (Springer, Berlin-Heidelberg, 1986).
- [55] M. Fortin and F. Brezzi, *Mixed and hybrid finite element methods*, vol. 3 (New York: Springer-Verlag, 1991).
- [56] M. Fortin and R. Pierre, “On the convergence of the mixed method of Crochet and Marchal for viscoelastic flows,” *Computer Methods in Applied Mechanics and Engineering* **73**(3), 341–350 (1989). URL <https://www.sciencedirect.com/science/article/pii/004578258990073X>.
- [57] A. Fortin, R. Guénette, and R. Pierre, “On the discrete EVSS method,” *Computer Methods in Applied Mechanics and Engineering* **189**, 121–139 (2000).

BIBLIOGRAPHY

- [58] J. Marchal and M. Crochet, “A new mixed finite element for calculating viscoelastic flow,” *Journal of Non-Newtonian Fluid Mechanics* **26**(1), 77–114 (1987).
- [59] J. Baranger and D. Sandri, “A formulation of Stokes’s problem and the linear elasticity equations suggested by the Oldroyd model for viscoelastic flow,” *ESAIM: Mathematical Modelling and Numerical Analysis - Modélisation Mathématique et Analyse Numérique* **26**(2), 331–345 (1992). URL http://www.numdam.org/item/M2AN_1992__26_2_331_0/.
- [60] A. Ouazzi, *Finite Element Simulation of Nonlinear Fluids: Application to Granular Material and Powder*, Industrial and applied mathematics (Shaker, 2005).
- [61] S. Turek and A. Ouazzi, “Unified edge-oriented stabilization of nonconforming FEM for incompressible flow problems: Numerical investigations,” *Journal of Numerical Mathematics* **15**(4), 299–322 (2007).
- [62] H. Damanik, *FEM Simulation of Non-isothermal Viscoelastic Fluids* (TU Dortmund, Germany, 2011). PhD Thesis.
- [63] H. Damanik, J. Hron, A. Ouazzi, and S. Turek, “A monolithic FEM approach for the log-conformation reformulation (LCR) of viscoelastic flow problems,” *Journal of Non-Newtonian Fluid Mechanics* **165**(19), 1105–1113 (2010). URL <https://www.sciencedirect.com/science/article/pii/S0377025710001515>.
- [64] C. T. Kelley, *Iterative methods for linear and nonlinear equations* (SIAM, Philadelphia, 1995).
- [65] A. Quarteroni, R. Sacco, and F. Saleri, *Numerical mathematics*, vol. 37 (Springer Science & Business Media, 2010).
- [66] J. E. Dennis and R. B. Schnabel, *Numerical Methods for Unconstrained Optimization and Nonlinear Equations* (Society for Industrial and Applied Mathematics, 1996).
- [67] W. H. Press, S. A. Teukolsky, W. T. Vetterling, and B. P. Flannery, *Numerical Recipes in C++: The Art of Scientific Computing* (Cambridge University Press, 2002).
- [68] H. Damanik, J. Hron, A. Ouazzi, and S. Turek, “Monolithic Newton-multigrid solution techniques for incompressible nonlinear flow models,” *International Journal for Numerical Methods in Fluids* **71**, 208–222 (2012).
- [69] H.-B. An, J. Wen, and T. Feng, “On finite difference approximation of a matrix-vector product in the Jacobian-free Newton–Krylov method,” *Journal of Computational and Applied Mathematics* **236**(6), 1399–1409 (2011). URL <https://www.sciencedirect.com/science/article/pii/S0377042711004730>.

BIBLIOGRAPHY

- [70] L. N. Trefethen and D. Bau, *Numerical Linear Algebra* (SIAM, 1997).
- [71] G. Strang, *Linear Algebra and Its Applications*, 3rd ed. (Brooks/Cole, 1988).
- [72] T. A. Davis, “Algorithm 832: UMFPACK V4.3—an Unsymmetric-Pattern Multifrontal Method,” *ACM Trans. Math. Softw.* **30**(2), 196–199 (2004). URL <https://doi.org/10.1145/992200.992206>.
- [73] H. A. van der Vorst, “Bi-CGSTAB: A Fast and Smoothly Converging Variant of Bi-CG for the Solution of Nonsymmetric Linear Systems,” *SIAM Journal on Scientific and Statistical Computing* **13**(2), 631–644 (1992). URL <https://doi.org/10.1137/0913035>.
- [74] Y. Saad and M. H. Schultz, “GMRES: A Generalized Minimal Residual Algorithm for Solving Nonsymmetric Linear Systems,” *SIAM Journal on Scientific and Statistical Computing* **7**(3), 856–869 (1986).
- [75] P. Wesseling, *An Introduction to Multigrid Methods*, An Introduction to Multigrid Methods (R.T. Edwards, 2004). URL <https://books.google.de/books?id=RoRGAAAYAAJ>.
- [76] W. Hackbusch, *Multi-grid methods and applications*, vol. 4 (Springer Science & Business Media, 2013).
- [77] C. Oosterlee and P. Wesseling, “A multigrid method for an invariant formulation of the incompressible Navier—Stokes equations in general Coordinates,” *Communications in applied numerical methods* **8**(10), 721–734 (1992).
- [78] S. Vanka, “Block-implicit multigrid solution of Navier-Stokes equations in primitive variables,” *Journal of Computational Physics* **65**(1), 138–158 (1986). URL <https://www.sciencedirect.com/science/article/pii/0021999186900082>.
- [79] “DFG benchmark 2D-1 (RE20, laminar),” URL http://www.mathematik.tu-dortmund.de/~featflow/en/benchmarks/cfdbenchmarking/flow/dfg_benchmark1_re20.html.
- [80] M. A. Afaq, A. Fatima, S. Turek, and A. Ouazzi, “Robust Monolithic Multigrid FEM Solver for Three Field Formulation of Incompressible Flow Problems,” Tech. rep., Fakultät für Mathematik, TU Dortmund (2023). Ergebnisberichte des Instituts für Angewandte Mathematik, Nummer 659.
- [81] M. El-Borhamy, *Numerical Simulation for viscoplastic fluids via finite element methods* (TU Dortmund, Germany, 2012). PhD Thesis.
- [82] J. Málek, V. Průša, and K. Rajagopal, “Generalizations of the Navier–Stokes fluid from a new perspective,” *International Journal of Engineering Science* **48**(12), 1907–1924 (2010). URL

BIBLIOGRAPHY

<https://www.sciencedirect.com/science/article/pii/S0020722510001205>.

- [83] S. Mandal, A. Ouazzi, and S. Turek, “Modified Newton solver for yield stress fluids,” in *Proceedings of ENUMATH 2015, the 11th European Conference on Numerical Mathematics and Advanced Applications*, pp. 481–490 (Springer, 2016).
- [84] S. Mandal, *Efficient FEM solver for quasi-Newtonian flow problems with application to granular material* (TU Dortmund, Germany, 2016). PhD Thesis.
- [85] E. Mitsoulis and T. Zisis, “Flow of Bingham plastics in a lid-driven square cavity,” *Journal of Non-newtonian Fluid Mechanics* **101**, 173–180 (2001).
- [86] J. C. D. L. Reyes and S. G. Andrade, *A combined BDF-semismooth Newton approach for time-dependent Bingham flow* (Humboldt-Universität zu Berlin, Mathematisch-Naturwissenschaftliche Fakultät II, Institut für Mathematik, 2011).
- [87] S. González Andrade, S. López, and P. Merino, “Nonsmooth exact penalization second-order methods for incompressible bi-viscous fluids,” *Computational Optimization and Applications* **80** (2021).